

Utah State University

DigitalCommons@USU

All Graduate Theses and Dissertations

Graduate Studies

5-2010

Cooperative Remote Sensing and Actuation Using Networked Unmanned Vehicles

Haiyang Chao
Utah State University

Follow this and additional works at: <https://digitalcommons.usu.edu/etd>



Part of the [Electrical and Electronics Commons](#), and the [Robotics Commons](#)

Recommended Citation

Chao, Haiyang, "Cooperative Remote Sensing and Actuation Using Networked Unmanned Vehicles" (2010). *All Graduate Theses and Dissertations*. 597.
<https://digitalcommons.usu.edu/etd/597>

This Dissertation is brought to you for free and open access by the Graduate Studies at DigitalCommons@USU. It has been accepted for inclusion in All Graduate Theses and Dissertations by an authorized administrator of DigitalCommons@USU. For more information, please contact digitalcommons@usu.edu.



COOPERATIVE REMOTE SENSING AND ACTUATION USING
NETWORKED UNMANNED VEHICLES

by

Haiyang Chao

A dissertation submitted in partial fulfillment
of the requirements for the degree

of

DOCTOR OF PHILOSOPHY

in

Electrical Engineering

Approved:

Dr. YangQuan Chen
Major Professor

Dr. Wei Ren
Committee Member

Dr. Don Cripps
Committee Member

Dr. Todd Moon
Committee Member

Dr. Vladimir Kulyukin
Committee Member

Dr. Byron R. Burnham
Dean of Graduate Studies

UTAH STATE UNIVERSITY
Logan, Utah

2010

Copyright © Haiyang Chao 2010

All Rights Reserved

Abstract

Cooperative Remote Sensing and Actuation Using Networked Unmanned Vehicles

by

Haiyang Chao, Doctor of Philosophy

Utah State University, 2010

Major Professor: Dr. YangQuan Chen

Department: Electrical and Computer Engineering

This dissertation focuses on how to design and employ networked unmanned vehicles for remote sensing and distributed control purposes in the current information-rich world. The target scenarios are environmental or agricultural applications such as river/reservoir surveillance, wind profiling measurement, and monitoring/control of chemical leaks, etc. AggieAir, a small and low-cost unmanned aircraft system, is designed based on the remote sensing requirements from environmental monitoring missions. The state estimation problem and the advanced lateral flight controller design problem are further attacked focusing on the small unmanned aerial vehicle (UAV) platform. Then the UAV-based remote sensing problem is focused with further flight test results. Given the measurements from unmanned vehicles, the actuation algorithms are needed for missions like the diffusion control. A consensus-based central Voronoi tessellation (CVT) algorithm is proposed for better control of the diffusion process. Finally, the dissertation conclusion and some new research suggestions are presented.

(228 pages)

This work is dedicated
to my parents, Mr. Kezhi Chao and Mrs. Yufen Fu,
and to my brother Hailong Chao.

Acknowledgments

First, I would like to thank my Ph.D. advisor, Dr. YangQuan Chen, for offering me a great opportunity to work on the exciting MASnet and UAV projects in the Center for Self-Organizing and Intelligent Systems (CSOIS). Dr. Chen always encourages me to pursue for research excellence. He has brought me to a new level of research through frequent discussions and professional guidance. I could not go this far without his support.

Many thanks go to my committee members, not only for the knowledge I learned from them, but also for the deep thinking they delivered behind the lectures. Especially, I would like to thank Dr. Wei Ren for introducing me the consensus and UAV basics, and for guiding us in the experimental validations on the MASnet platform. I would also like to thank Dr. Don Cripps for his suggestions and encouragements when I got stuck by some problems, Dr. Todd Moon for leading the department to create a good research environment, and Dr. Vladimir Kulyukin for explaining his idea of adapting human languages to the machine level when interacting with robots. Special thanks to Mary Lee Anderson, the ECE graduate advisor, and to Tricia Brandenburg, the department secretary, for their professionalism when I turned to them for help.

Also, I need to appreciate all the colleagues I have been working with. I would like to thank Austin M. Jensen for working together on our UAV platforms days and nights, especially in 2008 and sharing with me all the tricks on RC flying. I would like to thank Calvin Coopmans for his help on the Gumstix and IMUs so that I could test my algorithms based on his hardware work. I would like to thank Dr. Ying Luo particularly for those days we spent together trying our best to implement the fractional order controller in real UAV flights. I would like to thank Long Di for helping me repair the airframes and testing outside at the USU research farm, whether it was freezing or sweltering. I would like to thank Yiding Han for his discussions of the software and his hard work to help us win the competition. I would like to thank Daniel Morgan for first looking into the Paparazzi open-source autopilot project and starting ours in the summer of 2007. I will always remember the

moments when we had our first autonomous flight and our first IMU-guided flight under the Paparazzi architecture. I need to thank all the others who have worked together with me on the UAV project, including Marc Baumann, Yongcan Cao, Hu Sheng, Aaron Avery, Mitch Humphries, Chris Hall, Aaron Quitberg, and Norman Wildmann. I need to thank Professor Raymond L. Cartee for providing the USU farm at Cache Junction as the flight test field. My thanks also go to my other colleagues and friends for their help, including William K. Bourgeois, Nathan Sorensen, Dr. Zhen Song, Dr. Hyo-Sung Ahn, Christophe Tricaud, Rongtao Sun, Yashordhan Tarte, Tripti Bhaskaran, Varsha Bhambhani, Jessi Lianghan N.G., Shayok Mukhopadhyay, Dr. Warren Philips, Dr. Hui Chen, Dr. Yan Li, Dr. Jiming Jin, Dr. Changpin Li, Bin Wang, Wei Sun, Yongshun Jin, Hongguang Sun, Zhuorui Song, and Jinlu Han.

My greatest thanks should go to my family, especially my parents, Mr. Kezhi Chao and Mrs. Yufen Fu, my brother Hailong Chao, and my cousin Tao Zhao. There is no way I could get a Ph.D. degree in the United States without their support. I still remember my parents' words to me when I was a child: "If you really want something, you can achieve it, but you have to work hard for it." Their love supports me through all those hard days, either for a paper deadline, for the project pressure, or for the burden of life.

Last, but not least, I would like to thank my major funding support: the Utah Water Research Laboratory (UWRL) MLF Seed Grant (2006-2010) and the Vice President for Research Fellowship from Utah State University. I would also like to thank Professor H. Scott Hinton, the Dean of College of Engineering, for travel support to Maryland for the AUVSI Student UAS competitions in Summer 2008 and 2009, the Graduate Student Senate for the Enhancement Award, and the Institute for Pure and Applied Mathematics (IPAM) at UCLA for the travel support to participate in the one week-long workshop on "Mathematical Challenges on Sensor Networks."

Haiyang Chao

Contents

	Page
Abstract	iii
Acknowledgments	v
List of Tables	xi
List of Figures	xii
Acronyms	xvii
1 Introduction	1
1.1 Dissertation Roadmap	1
1.1.1 Sensing and Control in the information-rich World	1
1.1.2 Typical Civilian Application Scenarios	4
1.1.3 Challenges in Sensing and Control Using Unmanned Vehicles	6
1.2 Research Motivations	8
1.2.1 Small Unmanned Aircraft System (UAS) Design for Remote Sensing	9
1.2.2 State Estimation for Small UAVs	10
1.2.3 Advanced Flight Control for Small UAVs	11
1.2.4 Cooperative Remote Sensing Using Multiple UAVs	13
1.2.5 Diffusion Control Using Mobile Actuator and Sensor Networks	13
1.3 Dissertation Contributions	14
1.4 Dissertation Organization	15
2 AggieAir UAS Platform	16
2.1 Introduction	16
2.2 Small UAS Overview	18
2.2.1 Autopilot Hardware	21
2.2.2 Autopilot Software	23
2.2.3 Typical Autopilots for Small UAVs	26
2.3 AggieAir UAS Platform	30
2.3.1 Remote Sensing Requirements	31
2.3.2 AggieAir System Structure	31
2.3.3 Flying-Wing Airframe	35
2.3.4 OSAM-Paparazzi Autopilot	37
2.3.5 OSAM Image Payload Subsystem	37
2.3.6 gRAID Image Georeference Subsystem	42
2.4 OSAM-Paparazzi Interface Design for IMU Integration	46
2.4.1 Hardware Interface Connections	47
2.4.2 Software Interface Design	48

2.5	AggieAir UAS Test Protocol and Tuning	52
2.5.1	AggieAir UAS Test Protocol	52
2.5.2	AggieAir Controller Tuning Procedure	53
2.6	Typical Platforms and Flight Test Results	55
2.6.1	Typical Platforms	55
2.6.2	Flight Test Results	56
2.7	Chapter Summary	57
3	State Estimation Filters for Small UAVs	60
3.1	Problem Definition and Notations	61
3.1.1	Rigid Body Rotations Basics	62
3.1.2	UAV Kinematics	65
3.2	Extended Kalman Filter for Attitude Estimation	66
3.2.1	General Extended Kalman Filter	66
3.2.2	Quaternion-Based Extended Kalman Filter	67
3.2.3	Euler Angles-Based Extended Kalman Filter	68
3.3	AggieEKF: GPS-Aided Extended Kalman Filter	69
3.4	Experimental Results	70
3.5	Chapter Summary	71
4	Advanced Lateral Flight Controller Design	75
4.1	Introduction	75
4.2	Preliminaries of UAV Flight Control	76
4.3	Roll-Channel System Identification and Control	78
4.3.1	System Model	79
4.3.2	Excitation Signal for System Identification	79
4.3.3	Parameter Optimization	80
4.4	Fractional Order Controller Design	80
4.4.1	Fractional Order Operators	80
4.4.2	PI^λ Controller Design	81
4.4.3	Fractional Order Controller Implementation	86
4.5	Simulation Results	87
4.5.1	Introduction to Aerosim Simulation Platform	87
4.5.2	System Identification of Roll-Channel	87
4.5.3	Fractional Order PI Controller Design Procedure	89
4.5.4	Integer Order PID Controller Design	90
4.5.5	Comparison	91
4.6	UAV Flight Testing Results	92
4.6.1	The ChangE UAV Platform	93
4.6.2	System Identification	95
4.6.3	Proportional Controller and Integer Order PI Controller Design	97
4.6.4	Fractional Order PI Controller Design	97
4.6.5	Flight Test Results	99
4.7	Chapter Summary	100

5	Single UAV-Based Remote Sensing	102
5.1	Motivations for Remote Sensing	103
5.1.1	Water Management and Irrigation Control Requirements	103
5.1.2	Introduction of Remote Sensing	103
5.2	Remote Sensing Using Small UAVs	104
5.2.1	Coverage Control	105
5.2.2	Georeference Problem	107
5.3	Sample Applications for AggieAir	112
5.3.1	Farmland Coverage	112
5.3.2	Road Surveying	113
5.3.3	Water Area Coverage	114
5.3.4	Riparian Surveillance	115
5.3.5	Remote Data Collection	117
5.3.6	Other Applications	122
5.4	Chapter Summary	122
6	Cooperative Remote Sensing Using Multiple Unmanned Vehicles	124
6.1	Consensus-Based Formation Control	125
6.1.1	Consensus Algorithms	125
6.1.2	Implementation of Consensus Algorithms	126
6.1.3	MASnet Hardware Platform	127
6.1.4	Experimental Results	129
6.2	Surface Wind Profile Measurement Using Multiple UAVs	134
6.2.1	Problem Definition: Wind Profile Measurement	136
6.2.2	Wind Profile Measurement Using UAVs	139
6.2.3	Wind Profile Measurement Using Multiple UAVs	141
6.2.4	Preliminary Simulation and Experimental Results	142
6.3	Chapter Summary	148
7	Diffusion Control Using Mobile Sensor and Actuator Networks	149
7.1	Motivation and Background	149
7.2	Mathematical Modeling and Problem Formulation	150
7.3	CVT-Based Dynamical Actuator Motion Scheduling Algorithm	153
7.3.1	Motion Planning for Actuators with The First Order Dynamics	153
7.3.2	Motion Planning for Actuators with The Second Order Dynamics	153
7.3.3	Neutralizing Control	154
7.4	Information Consensus in CVT-Based Diffusion Control	154
7.4.1	Basic Consensus Algorithm	154
7.4.2	Requirements of Diffusion Control	155
7.4.3	Consensus-Based CVT Algorithm	156
7.5	Simulation Results	160
7.6	Chapter Summary	167

8	Conclusions and Future Research Suggestions	168
8.1	Conclusions	168
8.2	Future Research Suggestions	169
8.2.1	VTOL UAS Design for Civilian Applications	169
8.2.2	Monitoring and Control of Fast-Evolving Processes	170
8.2.3	Other Future Research Suggestions	171
	References	172
	Appendices	181
Appendix A	IMU/GPS Serial Communication Protocols	182
A.1	u-blox GPS Serial Protocol	182
A.2	Microstrain GX2 Serial Protocol	182
A.3	Crossbow MNAV Serial Protocol	183
A.4	Xsens Mti-g Serial Protocol	184
Appendix B	Paparazzi Autopilot Software Architecture: A Modification Guide	185
B.1	Autopilot Software Structure	185
B.2	Configuration XML Files	186
B.3	Airborne C Files	187
B.4	OSAM-Paparazzi Interface Implementation	188
B.5	Roll-Channel Fractional Order Controller Implementation	189
Appendix C	List of Documents for CSOIS Flight Test Protocol	195
C.1	Sample CSOIS-OSAM Flight Test Request Form	195
C.2	Sample CSOIS-OSAM 48" UAV (IR) In-lab Inspection Form	197
C.3	Tiger Preflight Checklist for AUVSI SUAS Competition 2009	198
Appendix D	DiffMAS2D Code Modification Guide	199
D.1	Files Description	199
D.2	Diffusion Animation Generation	200
D.3	Implementation of CVT-Consensus Algorithm	200
	Vita	205

List of Tables

Table	Page
2.1 Small UAS categories.	19
2.2 Comparison of physical specifications of autopilots.	30
2.3 Comparison of autopilot functions.	30
2.4 AggieAir2 UAS specifications.	34
2.5 Ghost Finger digital video camera specifications.	39
2.6 Ghost Finger digital camera specifications.	39
2.7 Serial mapping of Gumstix Console-VX board.	47
2.8 Communication protocol between Gumstix and Paparazzi.	53
2.9 Packet definition for data from GhostGX2.	53
2.10 Gumstix resource monitoring for GhostGX2.	58
2.11 UAVs developed (or partly developed) by the author.	59
2.12 Robustness of AggieAir UAS.	59
3.1 IMU categories.	60
4.1 ChangE UAS specifications.	94
6.1 AggieAir UAS specifications.	145
7.1 Comparison of control performance.	163
7.2 Comparison of total neutralizing material.	166

List of Figures

Figure	Page
1.1 Sensors and actuators in an information-rich world.	2
1.2 Unmanned vehicles as mobile sensors/actuators.	3
1.3 System structures of unmanned vehicles.	4
1.4 Typical agricultural field (Cache Junction, UT).	5
1.5 Water watch concept.	5
1.6 Fog evolution (taken in Yellowstone National Park).	7
1.7 Cyber physical systems.	7
2.1 UAS structure.	20
2.2 Functional structure of the UAV autopilot.	21
2.3 Procerus Kestrel autopilot.	27
2.4 Piccolo LT autopilot.	28
2.5 Paparazzi autopilot tiny 13.	29
2.6 AggieAir UAS physical structure.	33
2.7 AggieAir2 UAS airborne layout.	33
2.8 AggieAir2 main bay layout.	34
2.9 Unicorn wing.	35
2.10 CG calculation for flying wings.	36
2.11 AggieAir airborne system structure.	38
2.12 Ghost Finger video camera.	40
2.13 Ghost Finger video camera 2×1	41
2.14 Ghost Finger digital camera.	41

2.15	Ghost Finger DC packages.	42
2.16	Camera body (left) and its CCD sensor (right).	43
2.17	Aircraft coordinate systems.	44
2.18	Definition of initial image corners.	45
2.19	Gumstix Verdex and Console-VX boards.	48
2.20	OSAM-Paparazzi hardware connection.	49
2.21	Flow chart of GhostGX2.	50
2.22	Flow chart of OSAM interface on Paparazzi autopilot.	52
2.23	AggieAir UAS test protocol.	54
2.24	Layout of Pheonix 48" UAV.	56
2.25	Layout of Snow 72" UAV.	56
2.26	Sample flight trajectories of AggieAir2 UAV (Tiger).	57
2.27	AggieAir altitude tracking results.	58
3.1	Central bay layout of three IMUs.	71
3.2	UAV trajectory for sensor data collection.	72
3.3	Roll angle estimation (AggieEKF).	73
3.4	Pitch angle estimation (AggieEKF).	73
3.5	Roll angle estimation (JungEKF).	74
3.6	Pitch angle estimation (JungEKF).	74
4.1	FOPI flight controller design procedure.	78
4.2	System identification procedure.	79
4.3	UAV flight controller design procedure.	88
4.4	System identification of roll-channel.	89
4.5	FOPI flight controller.	90
4.6	Bode plot with designed FOPI controller.	91

4.7	Step response comparison: modified Z-N versus FOPI.	92
4.8	Robustness to wind disturbance.	93
4.9	Effects of payload gain variations.	93
4.10	ChangE UAV platform.	94
4.11	Paparazzi GCS.	95
4.12	Roll-channel system identification.	96
4.13	Proportional controller for outer roll loop.	98
4.14	Bode plot of $G(z)$	99
4.15	Anti-windup for FOPI and IOPI controllers.	99
4.16	FOPI controller for outer roll loop.	100
4.17	FOPI versus IOPI controller with various system gains.	101
5.1	Footprint calculation.	106
5.2	UAV flight path.	107
5.3	Photos before stitch.	109
5.4	Photos after stitching.	110
5.5	Camera frame and mesh.	111
5.6	Cache Junction farm coverage map (courtesy of A. M. Jensen for image stitching).	113
5.7	Beaver resort intersection (courtesy of A. M. Jensen for image stitching). . .	114
5.8	Desert lake coverage map (courtesy of A. M. Jensen for image stitching). . .	116
5.9	River tracking map after stitching (courtesy of A. M. Jensen for image stitching).	117
5.10	Sample pictures for river tracking.	118
5.11	Oneida Narrows imagery (courtesy of A. M. Jensen for image processing). .	119
5.12	UAV trajectory.	120
5.13	Further analysis of data logger 3.	121

5.14	Sample thermal picture.	123
6.1	MASnet experimental platform.	128
6.2	Communication topologies for the rendezvous experiment.	129
6.3	Experimental results of rendezvous for Cases I-III.	130
6.4	Switching information topologies \mathcal{G}_1 - \mathcal{G}_5 and their union \mathcal{G}_u for rendezvous.	131
6.5	Experimental results of rendezvous with topologies randomly switched from $\bar{\mathcal{G}}_s$ versus a time-invariant topology \mathcal{G}_u	131
6.6	Undirected interaction topology for axial alignment.	132
6.7	Experimental result of axial alignment.	132
6.8	Information exchange topology for formation maneuvering.	133
6.9	Experimental result of formation maneuvering.	133
6.10	A random wind field.	138
6.11	UAVs flying in a simplex formation.	142
6.12	Wind measurement (simulation).	143
6.13	Estimation of wind speed \bar{u}	144
6.14	Estimation of wind speed \bar{v}	144
6.15	Example wind field measured by AggieAir UAV.	146
6.16	Estimation of wind speed U	147
6.17	Estimation of wind speed V	147
7.1	Surf plot of a diffusion process modeled by (7.1): $k = 0.01$, $f_c = 0$, $f_d = f_d(0.8, 0.2, 20e^{-t})$	151
7.2	Simulation: rendezvous to the affected area.	158
7.3	Plain CVT diffusion control.	159
7.4	Spraying speed comparison for CVT.	159
7.5	Initial layout of diffusion control.	161
7.6	p_3 alone broadcasts.	162

7.7	p_1 , p_3 and p_4 broadcast.	162
7.8	Trajectory comparison between the consensus-based CVT and plain CVT. . .	163
7.9	Comparison of total pollutants: plain CVT and consensus CVT.	164
7.10	Distance to the source.	164
7.11	Actuator trajectories of consensus-based CVT and plain CVT.	165
7.12	Comparison of total pollutants: plain CVT and consensus CVT.	165
7.13	Comparison of spraying speeds.	167
8.1	UAVs in formation.	171
A.1	Crossbow MNAV IMU.	183
A.2	Xsens Mti-g IMU.	184
B.1	Paparazzi autopilot software structure.	186
D.1	DiffMAS2D Simulink model.	201

Acronyms

AGL	above ground level
ARX	auto-regressive exogenous
AUVSI	Association for Unmanned Vehicle Systems International
BFCS	body-fixed coordinate system
CCD	charge-coupled device
CG	center of gravity
COTS	commercial off-the-shelf
CPS	cyber-physical systems
CSOIS	Center for Self-Organizing and Intelligent Systems
CVT	centroidal Voronoi tessellations
DC	digital camera
DCM	direction cosine matrix
DOF	degree of freedom
DPS	distributed parameter system
DV	digital video camera
ECEF	Earth-centered Earth-fixed
ENAC	Ecole Nationale de l'Aviation Civile
EKF	extended Kalman filter
FOC	fractional order control
FOPI	fractional order proportional integral
FOPTD	first order plus time delay
FOV	field of view
GA	genetic algorithm
GCS	ground control station
GF	Ghost Finger
GF-DC	Ghost Finger digital camera
GF-DV	Ghost Finger digital video camera

GIS	geographic information system
GPS	global position system
gRAID	geospatial real-time aerial image display
ID	identification
IGS	inertial guidance system
IMU	inertial measurement unit
INS	inertial navigation system
IOPI	integer order proportional integral
IR	infrared
LQG	linear quadratic Gaussian
LIDAR	light detection and ranging
LLH	latitude longitude height
LS	least squares
LTV	linear time-varying
MASnet	mobile actuator and sensor network
MEMS	microelectromechanical systems
MIMO	multiple inputs multiple outputs
MZN	modified Ziegler-Nichols
NIR	near infrared
NN	neural network
ODE	ordinary differential equation
OSAM-UAV	open source autonomous multiple unmanned aerial vehicle
PDE	partial differential equation
PI	proportional-integral
PID	proportional-integral-derivative
PPRZ	Paparazzi open source autopilot project
PRBS	pseudo random binary signal
PTP	picture transfer protocol
RC	remote controlled
RGB	red-green-blue
RPV	remote piloted vehicle

SD	secure digital
SISO	single input single output
SO3	special orthogonal group
TWOG	tiny without GPS
UART	universal asynchronous receiver/transmitter
UAS	unmanned aircraft system
UAV	unmanned air/aerial vehicle
UGV	unmanned ground vehicle
USB	universal serial bus
USU	Utah State University
UTM	universal transverse mercator
UUV	unmanned underwater vehicle
UWRL	Utah Water Research Lab
VC	video camera
XML	extensible markup language

Chapter 1

Introduction

1.1 Dissertation Roadmap

This dissertation focuses on how to design and employ networked unmanned systems for remote sensing and distributed control purposes in the current information-rich world. The target scenarios include river/reservoir surveillance, wind profiling measurement, and distributed control of chemical leaks, etc., which are all closely related to the physical environment. Nowadays, threats of global warming and climate change demand accurate and low-cost techniques for a better modeling and control of the environmental physical processes. Unmanned systems could serve as mobile or stationary sensors and actuators. They could save human beings from dangerous, tedious, and repetitious outdoor work, whether it is deep in the ocean, or high up in the sky. With the modern wireless communication technologies, unmanned vehicles could even work in groups for some challenging missions such as forest fire monitoring, ocean sampling, etc. However, unmanned systems still require physics-coupled algorithms to accomplish such tasks mostly in the outdoor unstructured environments. Questions like what to measure, when to measure, where to measure, and how to control all need to be properly addressed. This dissertation presents our approach about how to build and employ networked unmanned vehicles (ground, air, or combined) to solve the problem of distributed sensing and distributed control of agricultural/environmental systems.

1.1.1 Sensing and Control in the information-rich World

Advances in electronics technologies such as embedded systems, microelectromechanical systems, and reliable wireless networks make it possible to deploy low-cost sensors and actuators in large amounts in a large-scale system. This poses a problem for control

scientists and engineers on how to deploy and employ those vast amount of networked sensors/actuators optimally. The sensors and actuators can be static or mobile, single or multiple, isolated or networked, all depending on the application scenario. The options for sensor and actuator types are shown in Fig. 1.1. For example, both the temperature probe (point-wise sensing) and the thermal camera (zone sensing) could be used to measure the temperature of the crop canopy in a given field of interest. But which one to use? Proper sensing techniques are essential for the high-precision farming that can support the sensing of a large scale system with an acceptable cost. Thermal aerial images are better for this mission. On the other hand, there are also coarse agricultural applications, which only need the temperature probe due to the cost limits. Another typical example is to use unmanned vehicles to monitor the forest fires. It is intuitive to use multiple unmanned aerial vehicles (UAVs) since they could provide more real-time information. However, there are questions regarding what information to share among UAVs and how often to share.

Unmanned vehicles can add the mobility to the sensors and actuators, which is especially beneficial for most outdoor environment monitoring applications. Different kinds of sensors and actuators could be installed on the unmanned vehicles based on specific ap-

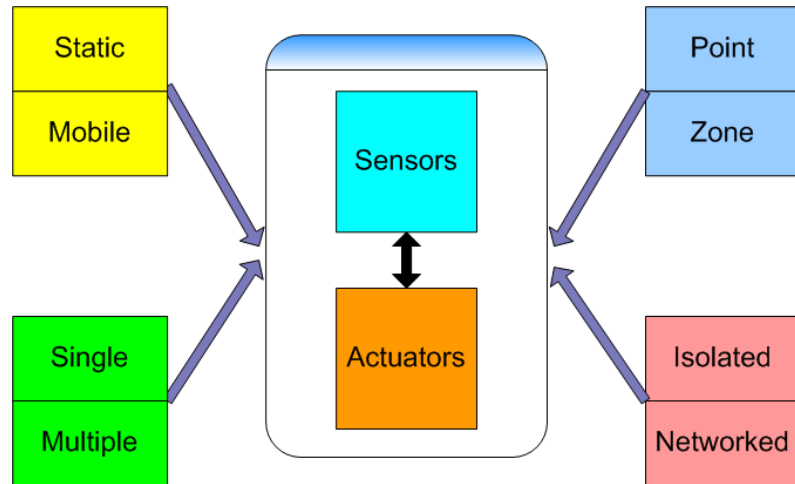


Fig. 1.1: Sensors and actuators in an information-rich world.

plication scenarios, shown in Fig. 1.2. For instance, contact sensors can be installed on unmanned underwater vehicles (UUVs) to make accurate measurements of the temperature and humidity of the sea current. Cameras or radars can be mounted on unmanned aerial vehicles (UAVs) for a more complete view of a farm or a reservoir. Chemical sprayers could be installed on unmanned ground vehicles (UGVs) for neutralizing gas leaks or extinguishing the fires.

In this dissertation, the unmanned system is defined as the unmanned vehicle together with onboard payload sensors or actuators. The fundamental functions of a typical unmanned systems include the mobility, computation, decision making, communication, and sensing/actuation, shown in Fig. 1.3. Most unmanned systems have a powerful embedded processor to coordinate all the functions and make decisions based on information collected from its own or shared from other neighboring vehicles. With the communication subsystems, groups comprising of heterogeneous unmanned systems can now be designed to cooperate with each other to maximize their capabilities and the team's collective performance.

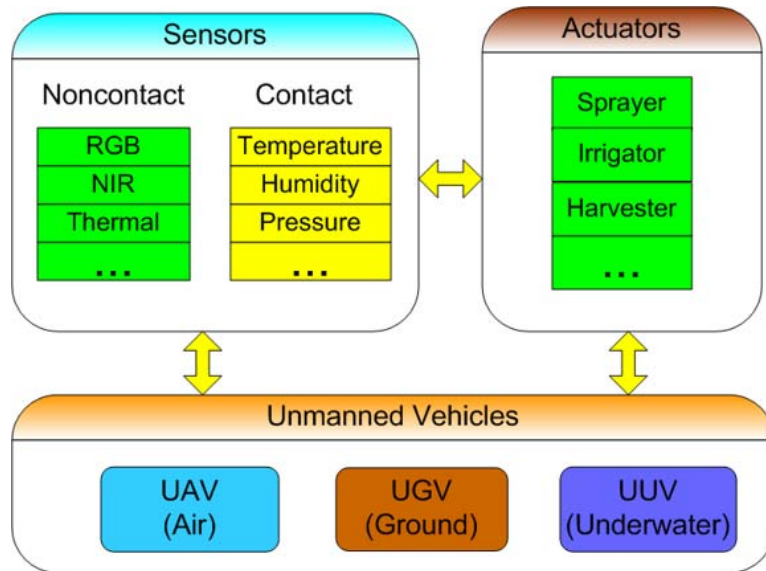


Fig. 1.2: Unmanned vehicles as mobile sensors/actuators.

1.1.2 Typical Civilian Application Scenarios

This dissertation focuses mostly on the monitoring and control of environmental or agricultural systems or processes, which are of course closely related to human beings. Such systems could be categorized into two groups: fast-evolving ones such as chemical spill, gas leak, or forest fire and slow-evolving ones including heat transfer, moisture changing, or wind profiling, etc. The objective of monitoring these kinds of systems is to characterize how one or several physical entities evolve with both time and space. One typical example is an agricultural farm, shown in Fig. 1.4. Water managers are interested in knowing how the soil moisture evolves with time in a farm to minimize the water consumption for irrigations. However, the evolving of soil moisture is affected by many other factors like water flows, wind conditions, weather conditions, and vegetation types, which all require measurements over a large scale (typically tens of square miles or even bigger). For such missions, ground probe stations are expensive to build and can only provide sensor data with very limited range. Satellite images can cover a large area, but have a low spatial resolution and a slow temporal update rate. Small UAVs cost less money but can provide more accurate information from low altitudes with less interference from clouds. Small UAVs combined

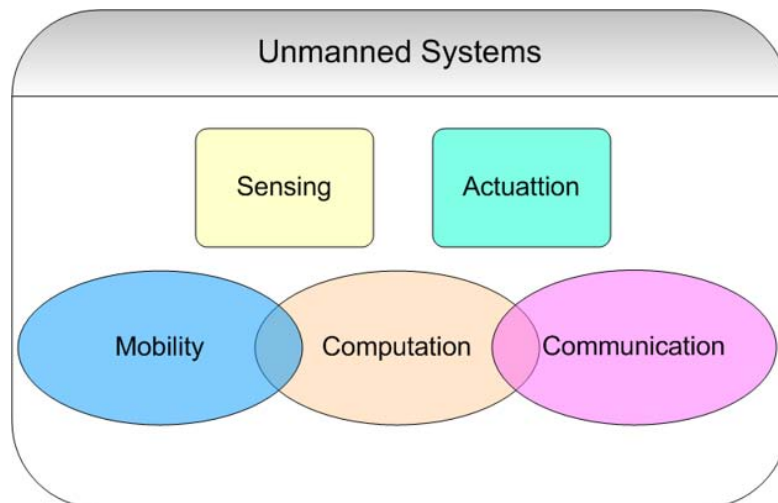


Fig. 1.3: System structures of unmanned vehicles.

with ground and orbital sensors can even form a multi-scale remote sensing system, shown in Fig. 1.5.



Fig. 1.4: Typical agricultural field (Cache Junction, UT).

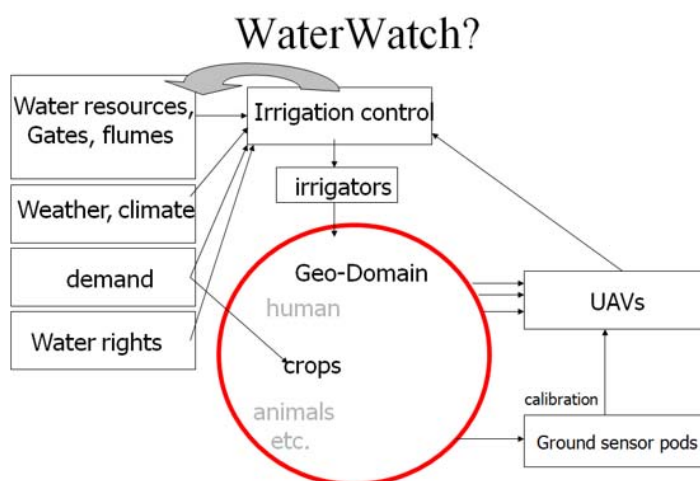


Fig. 1.5: Water watch concept.

Other typical civilian applications of unmanned systems include:

- Forest fire monitoring and containment control: The monitoring, prediction, and containment control of forest fires could greatly reduce the potential property damages. Unmanned systems have obvious advantages over manned vehicles because human operators are not required onboard.
- Fog evolution or chemical leaking monitoring and control: The evolving of hazardous fogs under emergency conditions can cost human lives without accurate and real-time measurements from unmanned systems. Example harmless fog evolutions are shown in Fig. 1.6.
- Wind field measurement: The wind direction and wind speed could have a significant impact on the diffusion of heat, water, or wind powers. However, the wind field is hard to measure because its high variation both temporally and spatially. Unmanned vehicles can be easily sent into the air for accurate 3D measurements.
- Canopy moisture measurement and irrigation control: The moisture on the vegetation canopy represents how much water could be absorbed by the plants. This information can be used for accurate irrigation control. The large scale of most agriculture fields require some cheap sensing techniques.

1.1.3 Challenges in Sensing and Control Using Unmanned Vehicles

The problem of monitoring an environmental field can be defined as below. Let $\Omega \subset R^3$ be a polytope including the interior, which can be either convex or nonconvex. A series of density functions $\varrho_1, \varrho_2, \varrho_3 \dots$ are defined as $\varrho_i(q, t) \in [0, \infty), \forall q \in \Omega$. For instance, ϱ_i could be wind direction, surface temperature, or soil moisture level, etc. The goal of monitoring a spatial-temporal process is to find the distribution of the required density functions:

$$\varrho_1(q, t), \varrho_2(q, t), \varrho_3(q, t) \dots \quad \forall q \in \Omega, \forall t \in [t_1, t_2],$$

with preset spatial and temporal resolutions. The concept of using mobile sensor and actuator network to finish the remote sensing and distributed control missions is shown in Fig. 1.7. For example, a flying sensor network is sent out to collect the information of environmental fields. The ground probe station can be used for sensing validation. A group of ground robots serve as the actuator network to achieve the control missions. The whole system can also be called a cyber-physical system.



Fig. 1.6: Fog evolution (taken in Yellowstone National Park).

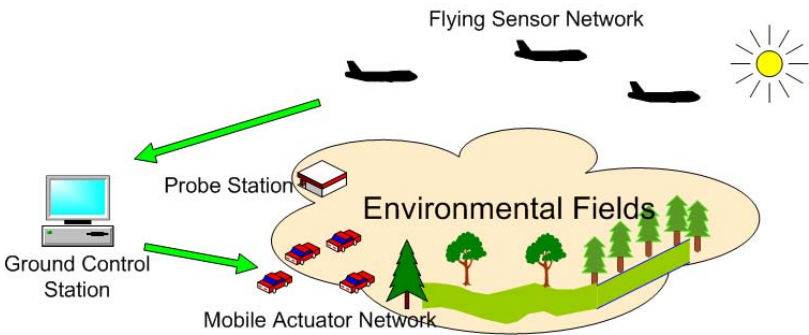


Fig. 1.7: Cyber physical systems.

There are many challenges to achieve this mission especially for water, agriculture, or environmental applications, as stated in the following:

- Low-cost solutions: Most civilian applications are highly constrained by the cost. Sometimes, even satellite images are not affordable in a routine way for farmers.
- Large-scale sensing: Most water lands, agricultural fields are large scale systems as big as tens or hundreds square miles.
- High temporal requirements: Some applications require the collections of images while the day light is as strong as possible.
- High spatial requirements: Many scenarios like vegetation classification need much higher resolution image than what the normal satellite image can provide.
- Easy manipulation: The civilian applications require the data collection procedure to be as easy as possible and as simple as possible.
- Advanced sensor/actuator allocation algorithms: Both the slow and fast evolving processes require properly designed strategies for sensing and control missions.

The above challenges could also be summarized as:

- What to measure and control? What entity needs to be measured and controlled?
- How to measure and control? What sensing or actuation systems are needed given a specific mission?
- When to measure and control? What time or how frequently to perform it?
- Where to measure and control? How to plan the trajectories of mobile sensors and actuators?

1.2 Research Motivations

Several research motivations are listed in the following sections for the sensing and actuation missions of environmental or agricultural fields.

1.2.1 Small Unmanned Aircraft System (UAS) Design for Remote Sensing

Many farms and environmental fields are tens, or hundreds of square miles big. It is too expensive to build ground probes for monitoring purposes in all the interested areas. Remote sensing can provide a good solution here because of the wider sensing footprint from the air. There are several options for remote sensing including satellites, manned aircrafts, and UAVs. Satellite images can cover a large area, but they have low spatial resolutions and slow update rates. Manned aerial imagery is expensive to acquire. Small UAVs cost less money and can provide more accurate information from low altitudes with less interference from clouds. Small UAVs combined with ground and orbital sensors can even form a multi-scale remote sensing system.

Technological advances in wireless networks and microelectromechanical systems make it possible to capture aerial images using small and inexpensive UAVs for civilian applications [1]. Small UAVs have a relatively short wingspan and light weight. They can be operated by one to two people [2]. Many of them can even be hand-carried and hand-launched. In fact, small UAVs are designed to fly at low altitude (normally less than 1000 meters above the ground) to provide a close observation of the ground objects and phenomena.

The problem of remote sensing using small UAVs can be divided into three subproblems.

UAS Integration Problem

The primary problem for using small UAVs in remote sensing is the system integration because there are no commercial off-the-shelf (COTS) inexpensive multi-spectral UAV solutions for civilian applications to the author's best knowledge. To achieve the autonomous navigation and image capture functions, the minimal UAV system requires the navigation subsystem (autopilot) and the image subsystem. However, the autopilot alone costs around \$5000 or more [2]. The integration of the image subsystem to the UAV also requires special considerations not only for the space and weight limits but also for the post-flight image georeferencing processes. Different imagers (red-green-blue (RGB), near infrared (NIR), or thermal band) may have special requirements. It is very challenging to integrate all the

COTS units and open source projects into a robust and fully functional UAS.

Image Collection Problem

The image collection problem is how to plan the waypoints or trajectory of the UAV or group UAVs so that the images could be captured in a fastest way. The problem can be defined as follows. Given a random area of interest Ω ; UAVs with functions of altitude and speed keeping and waypoint navigation: speed v , flight height h ; camera with specification: focal length F , image sensor pixel size $PS_h \times PS_v$, image sensor pixel pitch $PP_h \times PP_v$, the “camera shooting interval” t_{shoot} ; the desired image resolution res ; the control objective is:

$$\min t_{flight} = g(\Omega, h, v, \{q_1, \dots, q_i\}, t_{shoot}, res), \quad (1.1)$$

subject to $v \in [v_1, v_2]$, $h \in [h_1, h_2]$, $t_{shoot} = k \times t_{shoot_{min}}$, where t_{flight} is the flight time of the UAV for effective coverage, $g(\Omega, h, v, t_{shoot})$ is the function to determine the flight path and flight time for effective coverage, k is a positive integer. This solution of this optimal problem is also the endurance time of the unmanned system since both the image acquisition and the UAV trajectory following need to be considered.

Image Registration and Postprocessing Problem

After the images are captured, the next problem is to correlate the images with the temporal and spatial data, which is also called georeferencing or image registration. Then the image information could be further processed to get the final environmental data like soil temperature, or vegetation distributions, etc.

All these three subproblems need to be addressed to design a cheap and robust small UAS for the remote sensing mission.

1.2.2 State Estimation for Small UAVs

The estimation accuracy of the UAV states in the air can greatly affect the UAV flight control performance and the later image georeferencing results. However, many required

states are either not directly measurable (e.g., the orientation) or sampled slowly (e.g., the position) with current MEMS sensors. With the emerging of cheaper and smaller MEMS inertial measurement units (IMUs), it is necessary to develop our own state estimation algorithm to further reduce the system costs and to provide more flexibilities in post-flight georeferencing. The following states are indispensable for both the autonomous control and image registration:

- Position states: Most civilian GPS receivers can only provide position updates at 4 Hz or less, which can introduce a big error if the UAV is moving very fast;
- Orientation states: The orientation data is not directly measurable with the current MEMS technology. It can only be estimated using advanced filters from gyros, accelerometers, magnetometers, etc.

The estimation of the above states requires sophisticated nonlinear filter design techniques and extensive flight test validations for UAV navigation uses. Many researchers have looked into this problem with different hardware platforms. The extended Kalman filter is introduced for MNAV IMU as part of an open-source project [3]. Other researchers also take the speed measurement into consideration for a more accurate acceleration estimation [4]. With the current trend of modularization and standardization in the UAV design, UAV developers can save a large amount of time by buying the cheap COTS IMUs and configure them into a complete navigation system. Thus, a systematic procedure for the state filter design, tuning and validation needs to be developed to support these cheap COTS IMUs. Especially, the Kalman filter must be carefully designed to avoid entering the divergence [5].

1.2.3 Advanced Flight Control for Small UAVs

The UAV has an obvious safety advantage over a manned aircraft at extremely low altitudes (e.g., ~ 100 meters above the ground) because the autopilot can be used for the autonomous navigation replacing the human pilot. The autopilot or flight control system plays a key role not only for the flight stability and navigation but also for sensor interpretation considerations [2]. In a remote surveillance task, the navigation performance of

UAVs while flying horizontally could highly affect the georeferencing accuracy of the acquired aerial images. Small or micro UAV autonomous flight can be easily affected by many factors:

- Wind: Wind gusts present a significant control challenge for low-mass airplanes;
- Flight altitude: UAVs may need to fly at a broad range of altitudes for different missions;
- Payload variations: A good UAV flight controller should be robust to payload variations so that it will not stall with little perturbation;
- Manufacturing variations and modeling difficulties: Many research UAVs are built from remote controlled (RC) air frames, making it hard to get an accurate dynamic model;
- Resource limitations: Small or micro UAVs are also constrained by the onboard resources such as limited accuracy for onboard inertial sensors, limited computational power, limited size and weight, etc.

All the above factors make it very important to design a robust and flexible flight controller. A lot of researchers have looked into the problem of UAV modeling and control. Open-loop steady state flight experiments are proposed for the aileron-(roll rate) and elevator-(pitch rate) loop system identification [6]. But the open-loop system identification has to have special requirements on UAV flight stability, which limits the roll and pitch reference signals to be as small as 0.02 rad. UAV model identification (ID) experiments can also be performed with human operators controlling the UAVs remotely. Different types of auto-regressive with exogenous input (ARX) models are identified while the UAV is flying in loiter mode [7]. Human operators could generate open-loop responses but it may be impossible for some specially designed reference like pseudo random binary signals (PRBS). Other researchers also tried closed-loop system identification method on separate channels of unmanned helicopters [8–10].

1.2.4 Cooperative Remote Sensing Using Multiple UAVs

Because of the large-scale characteristics of most environmental fields, many applications may require remote sensing of a large land area (more than 30 square miles) within a short time (less than one hour). Acquisition of imagery on this geographic scale is difficult for a single UAV. However, groups of UAVs (which we call “covens”) can solve this problem because they can provide images from more spectral bands in a shorter time than a single UAV.

The following missions will need multiple UAVs (covens) operating cooperatively for remote sensing:

- Measure $\eta_1, \eta_2, \eta_3 \dots$ simultaneously;
- Measure $\eta_i(q, t)$ within a short time.

To fulfill the above requirements, UAVs equipped with imagers having different wavelength bands must fly in some formation to acquire the largest number of images simultaneously. The reason for this requirement is that electromagnetic radiation may change significantly, even over a period of minutes, which in turn may affect the final product of remote sensing.

1.2.5 Diffusion Control Using Mobile Actuator and Sensor Networks

The monitoring and control of a diffusion process can be viewed as an optimal sensor/actuator placement problem in a distributed system [11]. Basically, a series of desired actuator positions are generated based on centroidal Voronoi tessellations and later integrated with PID controllers for neutralizing control based on Voronoi partitions. CVT algorithm provides a non-model-based method for coverage control and diffusion control using groups of vehicles. The CVT algorithm is robust and scalable [12,13] and it can guarantee the groups asymptotically converging to the affected area even in multiple/mobile sources application [14].

1.3 Dissertation Contributions

The major contributions of this dissertation include, but are not limited to, the following:

- Designed and tested the AggieAir UAS, a low-cost multi-spectral remote sensing platform, which is one of the major contributions of this dissertation work;
- Developed and implemented a new state estimation algorithm for attitude estimation of small UAVs;
- Being the very first to design and implement the fractional order flight controller to guide the UAV in the real flight;
- Jointly developed the path planning algorithm for the remote sensing mission using a single UAV with different ground resolution requirements;
- Implemented and validated the multi-vehicle consensus algorithm on MASnet platform with different communication topologies;
- Developed the wind profiling measurement algorithm using multiple small fixed-wing UAVs;
- Proposed the consensus CVT-based path planning algorithm for the diffusion control problem.

Most of the algorithms and theories are validated on the following simulation or experimental platforms:

- Aerosonde UAV software simulation platform for flight controller design, state estimation algorithm tests;
- AggieAir UAV experimental platform for remote sensing, flying sensor network;
- MASnet hardware simulation platform for formation control, consensus validations;
- DiffMAS2D software simulation platform for diffusion control simulation.

1.4 Dissertation Organization

The dissertation is organized as the following. The research motivations and dissertation contributions are introduced in Chapter 1. Chapter 2 is dedicated to the introduction of AggieAir UAS platform, a low-cost multi-spectral remote sensing platform, with detailed explanation on the system design requirements, subsystem structures, and flight test protocol developments. Chapter 3 focuses on the state estimation problems for the small UAVs. The fractional order PI^α controller is designed and implemented on the roll-channel in Chapter 4 including model identification methods, controller designing procedure, and simulation/experimental validation results. Chapter 5 explains how to finish a typical remote sensing task using a single UAV with lots of application scenarios like water area, farmland, and road coverage, etc. The remote sensing problem using multiple unmanned vehicles is presented in Chapter 6. The multi-vehicle consensus algorithm is firstly tested on the MASnet platform and then a new algorithm for wind profiling measurement using multiple UAVs is proposed and tested in the simulation. Chapter 7 is devoted to the distributed control of a diffusion process using mobile sensor and actuator networks. The consensus and centroidal Voronoi tessellation (CVT)-based path planning algorithm is proposed and tested in simulations. Chapter 8 is for the conclusions and some future research suggestions.

Chapter 2

AggieAir UAS Platform

2.1 Introduction

This chapter focuses on the design and testing of AggieAir, a small low-cost unmanned aircraft systems (UAS). The primary design purpose of AggieAir is for remote sensing of meteorological and/or other related conditions over agricultural fields or other environmentally important land areas. Small UAS, including unmanned aerial vehicle (UAV) with the payload and ground devices, have many advantages in real-world remote sensing applications over traditional aircraft- or satellite-based platforms or ground-based probes. This is because small UAVs are easy to manipulate, cheap to maintain, and able to remove the need for human pilots to perform tedious or dangerous tasks. Multiple small UAVs can be flown in a group and accomplish challenging tasks such as real-time mapping of large-scale agriculture areas.

The purpose of remote sensing is to acquire information about the Earth's surface without coming into contact with it. One objective of remote sensing is to characterize the electromagnetic radiation emitted by objects [15]. Typical divisions of the electromagnetic spectrum include the visible light band (380-720 nm), near infrared (NIR) band (0.72-1.30 μm), and mid-infrared (MIR) band (1.30-3.00 μm). Band-reconfigurable imagers can deliver images from different bands ranging from visible spectra to infrared or thermal band depending on specific applications. Different combinations of spectral bands can have different purposes. For example, the combination of the red band and infrared band can be used to detect vegetation and camouflage while the combination of red slope can be used to estimate the percent of vegetation cover [16]. Different bands of images acquired remotely through UAS could be used in scenarios like water management and irrigation control [17]. In fact, it is difficult to sense and estimate the state of a water system because most water

systems are large-scale and need monitoring of many factors including the quality, quantity, and location of water, soil, and vegetation. For the mission of accurate sensing of a water system, ground probe stations are expensive to build and can only provide data with very limited sensing range (at specific locations and second-level temporal resolution). Satellite images can cover a large area, but have a low-spatial resolution and a slow update rate (30-250 meter, or lower-spatial resolution and week-level temporal resolution). Small UAVs cost less money but can provide more accurate information (meter or centimeter spatial resolution and hour-level temporal resolution) from low altitudes with less interference from clouds. Small UAVs combined with ground and orbital sensors can even form a multi-scale remote sensing system.

UAVs have been used in several agricultural remote sensing applications for collecting aerial images. High resolution red-green-blue (RGB) aerial photos can be used to determine the best harvest time of wine grapes [18]. Multispectral images are also shown to be potentially useful for monitoring the ripeness of coffee [16]. Images from reconfigurable bands taken simultaneously can increase the final information content of the imagery and significantly improve the flexibility of the remote sensing process. However, most current UAV remote sensing applications use large and expensive UAVs with heavy cameras (one or several kilograms), which makes it impossible for frequent civilian uses. Water management is still a new application area for UAVs, but it has more precision requirements compared with other remote sensing applications. For example, real-time management of water systems requires lots of precise information on water, soil, and plant conditions with preset spatial and temporal resolutions.

Motivated by the above remote sensing problem, AggieAirTM, a band-configurable small UAS-based remote sensing system, has been developed step-by-step at Center for Self Organizing and Intelligent Systems (CSOIS) together with Utah Water Research Lab (UWRL), Utah State University. The objective of this chapter is to present an overview of the ongoing research efforts on AggieAir platform. Particularly, this chapter focuses more on the system level design, integration, and testing with brief introductions on subsystem

details.

The chapter first presents a brief overview of the unmanned aircraft systems focusing on the core of the whole system: the autopilot. After introducing the common UAS structure, the hardware and software aspects of the autopilot control system are then explained. Different types of available sensor suites and autopilot control techniques are summarized. Several typical commercial off-the-shelf and open-source autopilot packages are compared. The chapter then introduces AggieAir, a small and low-cost UAS for remote sensing applications. AggieAir comprises of a flying-wing airframe as the test bed, the OSAM-Paparazzi autopilot for autonomous navigation, the Ghost Foto imaging system for image capture, the Paparazzi ground control station (GCS) for real-time monitoring, and the geospatial real-time aerial image display (gRAID) software for image post-processing. AggieAir UAS is fully autonomous, easy to manipulate, and independent of a runway. AggieAir can carry embedded cameras with different wavelength bands, which are low-cost but have high spatial resolution. These imagers mounted on UAVs can form a camera array to perform multi-spectral imaging with reconfigurable bands, depending on the objectives of the mission. Developments of essential subsystems, such as the airframe, the UAV autopilot, the imaging payload subsystem, and the image processing subsystem, are introduced together with some typical UAVs developed and built at CSOIS.

2.2 Small UAS Overview

In this thesis, the acronym UAV (Unmanned Aerial Vehicle) is used to represent a power-driven, reusable airplane operated without a human pilot on board. The UAS (Unmanned Aircraft System) is defined as a UAV and its associated elements which may include ground control stations, data communication links, supporting equipments, payloads, flight termination systems, and launch/recovery equipments [19]. Small UAS (sUAS) could be categorized into five groups based on gross take-off weight by the sUAS aviation rule making committee [19], as shown in Table 2.1. Group *i* includes those constructed in a frangible manner that would minimize injury and damages if there is a collision, compared with the group *ii*.

Table 2.1: Small UAS categories.

Group	Gross Take-off Weight
i	≤ 4.4 lbs or 2 kgs
ii	≤ 4.4 lbs or 2 kgs
iii	≤ 19.8 lbs or 9 kgs
iv	≤ 55 lbs or 25 kgs
v	lighter than air (LTA) only

The research and development of small UAS has been quite active in the past few years [2]. Many small fixed-wing or rotary-wing UAVs are flying in the air under the guidance from the autopilot systems for different applications like forest fire monitoring, coffee field survey, search and rescue, etc. A typical UAS includes:

- Autopilot: An autopilot is a MEMS system used to guide the UAV without assistance from human operators, consisting of both hardware and its supporting software. The autopilot is the base for all the other functions of the UAS platform.
- Airframe: The airframe is where all the other devices are mounted including the frame body, which can be made from wood, foam, metal, or composite materials. The airframe also includes the flight control surfaces, which could be a combination of either aileron/elevator/rudder, or elevator/rudder, or elevons.
- Payload: The payload of UAS could be cameras of different spectral bands, or other emission devices like LIDAR mostly for intelligence, surveillance, and reconnaissance purposes.
- Communication subsystem: Most UASs have more than one wireless link supported. For example, RC link for safety pilot, WiFi link for large data sharing, and data link for ground monitoring.
- Ground control station: Ground control station is used for real-time flight status monitoring and flight plan changing.

- Launch and recovery devices: Some UAS may need special launching devices like a hydraulic launcher or landing devices like a net [20].

The whole UAS structure is shown in Fig. 2.1. The minimal UAS onboard system requires the airframe for housing all the devices, the autopilot for sensing and navigation, the basic imaging payload for aerial images, and the communication subsystems for data link with the ground. The autopilot overview is focused first since it is the base for the UAS navigation and further image georeferencing.

Autopilot systems are now widely used in modern aircrafts and ships. The objective of UAV autopilot systems is to consistently guide UAVs to follow reference paths, or navigate through preset waypoints. A powerful UAV autopilot system can guide UAVs in all stages of autonomous flight including take-off, ascent, descent, trajectory following, and landing. An autopilot needs also to communicate with the ground station for control mode switch, to receive broadcasts from GPS satellites for position updates, and to send out control commands to the servo motors on UAV.

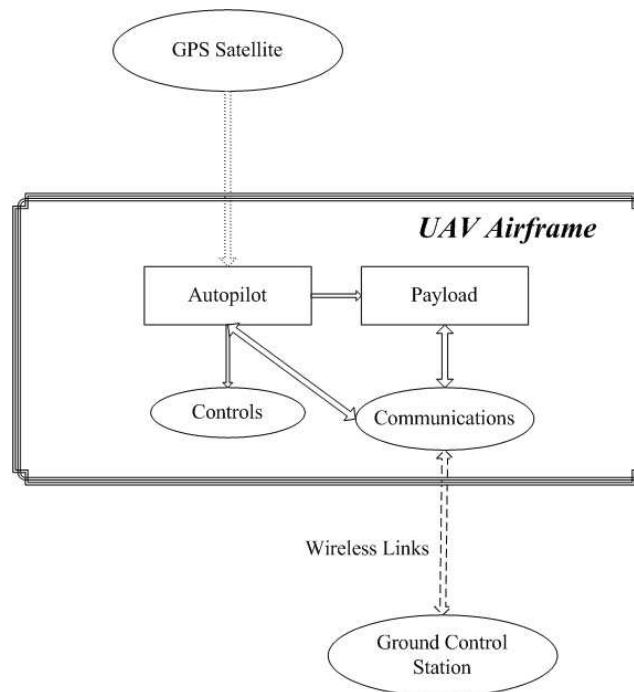


Fig. 2.1: UAS structure.

A UAV autopilot system is a closed-loop control system with two fundamental functions: state estimation and control signal generation based on the reference paths and the current states. The most common state observer is the inertial measurement unit (IMU) including gyros, accelerometers, and magnetic sensors. There are also other attitude determination devices available like infrared or vision-based ones. The sensor readings combined with the GPS information can be passed to a filter to generate the estimates of the current states for later control uses. Based on different control strategies, the UAV autopilots can be categorized as PID-based autopilots, fuzzy-based autopilots, neural network (NN)-based autopilots, etc. A typical commercial off-the-shelf UAV autopilot system comprises of a GPS receiver, an IMU, and an onboard processor (state estimator and flight controller) as illustrated in Fig. 2.2.

2.2.1 Autopilot Hardware

The hardware of a minimal autopilot system includes sensor packages for state determination, onboard processors for estimation and control uses, and some peripheral circuits for servo and modem communications. Due to the physical limitations of small UAVs, the autopilot hardware must be small, light, and have a long endurance time. Moreover, the sensor packages should guarantee precise and robust performances, especially in mobile and temperature-varying outdoor environments.

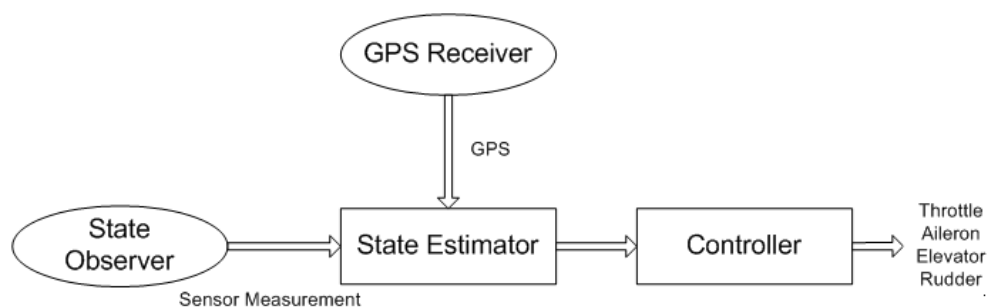


Fig. 2.2: Functional structure of the UAV autopilot.

MEMS Inertial Sensors

Inertial sensors are used to measure the 3D position and attitude information. The current MEMS technology makes it possible to use tiny and light sensors on small or micro UAVs. Available MEMS inertial sensors include:

- GPS receiver: To measure the positions (p_n, p_e, h) and ground velocities (v_n, v_e, v_d) .
- Rate gyro: To measure the angular rates (p, q, r) .
- Accelerometer: To measure the accelerations (a_x, a_y, a_z) . Accelerometers actually measures the acceleration minus the gravity.
- Magnetometer: To measure the magnetic field for the heading correction (ψ) .
- Pressure sensor: To measure the air speed (the relative pressure) and the altitude (h) .
- Ultrasonic sensor or SONAR: To measure the relative height above the ground.
- Infrared sensor: To measure the attitude angles (ϕ, θ) .
- RGB camera or other image sensors: To replace one or several of the above sensors.

GPS receiver plays an indispensable role in the autonomous control of UAVs because it provides an absolute position measurement. A known bounded error between GPS measurement and the real position can be guaranteed as long as there is a valid 3D lock. For instance, u-blox 5 GPS receiver can achieve a three meter 3D accuracy (pAcc for u-blox message) in the best case for civilian applications in the United States [21]. There are also differential GPS units which could achieve centimeter-level positioning accuracy. The disadvantage of GPS is its vulnerability to weather factors and its relatively low updating frequency (commonly 4 Hz or less), which may not be sufficient for UAV applications.

Possible Sensor Configurations

Given all the above inertial sensors, several sensor combinations can be chosen for different types of UAVs to achieve the basic autonomous waypoints navigation task. Most

current outdoor UAVs have GPS receivers onboard for position feedback. The major difference is the attitude measurement solution, which can be IMU, infrared sensor, or image sensor, etc.

Inertial Measurement Unit (IMU): A typical IMU includes 3-axis rate gyro and acceleration sensors, which can be filtered to generate an estimation of the attitude (ϕ, θ, ψ). A straightforward sensor solution for small UAVs is to use the IMU, which can provide a complete set of sensor readings. Microstrain GX2 is this kind of micro IMU with an update rate up to 100 Hz for inertial sensing. It has 3-axis magnetic, gyro, and acceleration sensors [22].

Infrared Sensor: Another solution for attitude sensing is using infrared thermopiles. The basic idea of infrared attitude sensor is to measure the heat difference between two sensors on one axis to determine the angle of the UAV because the Earth emits more IR than the sky. Paparazzi open-source autopilot group use infrared sensors as their primary attitude sensors [23,24]. However, we found that this solution is not accurate enough for post-flight georeferencing purposes.

Vision Sensor: Vision sensor can also be used to estimate the attitude by itself or combined with other inertial measurements [25]. The pseudo roll and pitch can be decided from the onboard video or image streams [26]. Experiments on vision-only-based navigation and obstacle avoidance have been achieved on small rotary wing UAVs [27]. In addition, vision-based navigation has potentials to replace the GPS for position measurements especially in task oriented and feature-based applications. Vision-based navigation for small UAVs is still an undergoing topic and a lot of work is needed for mature commercial autopilots.

2.2.2 Autopilot Software

All the inertial measurements from sensors will be sent to the onboard processor for further filtering and control processing. Autopilot could subscribe services from the available sensors based on different control objectives. The strength of the autopilot software directly affects the robustness of the whole autopilot system.

Autopilot Control Objectives

The UAV waypoints tracking task can be decomposed into several subtasks including:

- Pitch attitude holding;
- Altitude holding;
- Speed holding;
- Automatic take-off and landing;
- Roll-angle holding;
- Turn coordination;
- Heading holding.

State Estimation

To achieve the above control objectives, different system states are needed with relatively high frequency (typically above 20 Hz for small fixed-wing UAVs). However, sensors like GPS can only provide a noisy measurement in 4 Hz. Kalman filter can be used here to make an optimal estimation (H_2) of the current states including the UAV location, velocity, and acceleration. The users need to define a noise estimation matrix, which represents how far the estimate can be trusted from the true states. Kalman filtering needs lots of matrix manipulations, which add more computational burdens to the onboard processor. Therefore, it is necessary to simplify the existing Kalman filtering techniques based on different applications. Besides, several other issues, like gyro drifting and high frequency sensor noise, also need to be canceled out through filtering techniques.

Controller Design for Autopilots

Most current commercial and research autopilots focus on GPS-based waypoints navigation. The path-following control of the UAV can be separated to different layers:

- Inner loop on roll and pitch for attitude;

- Outer loop on heading and altitude for trajectory or waypoints tracking;
- Waypoint navigation.

There are two basic controllers for the UAV flight control: altitude controller, velocity and heading controller. Altitude controller is to drive the UAV to fly at a desired altitude including the landing and take-off stages. The heading and velocity controller is to guide the UAV to fly through the desired waypoints. To achieve the above control requirements, different control strategies can be used including PID, adaptive neural network, fuzzy logic, and fractional order control, etc. [28].

PID Approach: Most commercial autopilots use PID controllers. Given the reference waypoint coordinates and the current UAV state estimates, the controller parameters of different layers can be tuned off-line first and re-tuned during the flight. Most commercial autopilots use traditional PID controllers because they are easy to implement on the small UAV platforms. However, PID controllers have limitations in optimality and robustness. Besides, it is also difficult to tune the parameters under some circumstances.

Fuzzy-Based Autopilot: Research on autopilots for small UAVs is also quite active with other modern control strategies. Fuzzy logic control systems can be used in a lot of applications including flight control. There are totally three fuzzy controllers [29], one for lateral control and two for longitudinal control. A speed controller and a wind disturbance attenuation block are added for robustness. The hardware of this autopilot includes one PC 104 single board computer as the processor and a micro IGS as the sensing unit. This autopilot can guarantee waypoint navigation.

NN-Based Autopilot: Adaptive neural network controller does not require an accurate mathematical model and is suitable for multi-variable flight control. Although the NN-based autopilot is originally developed for unmanned helicopter control [30], it can also be applied in fixed wing UAVs like GT-wing test bed in Georgia Institute of Technology.

LQG/LTR & H_∞ -Based Autopilot: Both PID and NN autopilots are not model-based and the optimality and robustness of the controller can not be guaranteed. As most small UAVs are highly nonlinear systems and hard to get an accurate nonlinear model, a linear model can be used to approximate the UAV dynamics. A combination of Linear Quadratic Gaussian controller and kalman filter can be used to achieve better altitude control performance [31]. H_∞ loop shaping techniques can also be used on small fixed wing UAVs for improvements in noisy or even payload changing circumstances [32].

2.2.3 Typical Autopilots for Small UAVs

In this section, several available autopilots, including both commercial and open-source ones, are introduced and compared in terms of sensor configurations, state estimations, and controller strengths. Most commercial UAV autopilots have sensors, processors, and peripheral circuits integrated into one single board to account for size and weight constraints. The advantage of the open-source autopilots is its flexibility in both hardware and software. Researchers can easily modify the autopilot based on their own specific requirements.

Procerus Kestrel Autopilot

Procerus Kestrel Autopilot is specially designed for small or micro UAVs weighing only 16.7 grams (modem and GPS receiver not included), shown in Fig. 2.3 [33]. The specifications are shown in Table 7.1. Kestrel 2.2 includes a complete inertial sensor set including: 3-axis accelerometers, 3-axis angular rate sensors, 2-axis magnetometers, one static pressure sensor (altitude), and one dynamic pressure sensor (airspeed). With the special temperature compensations for sensors, it can estimate the UAV attitude (ϕ and θ) and the wind speed very accurately [33].

Kestrel has a 29 MHz Rabbit 3000 onboard processor with 512K RAM for onboard data logging. It has the built-in ability for autonomous take-off and landing, waypoint navigation, speed hold, and altitude hold. The flight control algorithm is based on the traditional PID control. The autopilot has elevator controller, throttle controller, and aileron controller separately. Elevator control is used for longitude and airspeed stability of the



Fig. 2.3: Procerus Kestrel autopilot.

UAV. Throttle control is for controlling airspeed during level flight. Aileron control is used for lateral stability of the UAV [33]. Procerus provides in-flight PID gain tuning with real-time performance graph. The preflight sensor checking and failsafe protections are also integrated to the autopilot software package. Multiple UAV functions are supported by Kestrel autopilots via the ground ComBox.

Cloud Cap Piccolo

Piccolo family of UAV autopilots from Cloud Cap Company provide several packages for different applications. PiccoloPlus is a full featured autopilot for fixed-wing UAVs. Piccolo *II* is an autopilot with user payload interface added. Piccolo LT is a size optimized one for small electric UAVs as shown in Fig. 2.4 [34]. It includes inertial and air data sensors, GPS, processing, RF data link, and flight termination, all in a shielded enclosure [34]. The sensor package includes three gyros and accelerometers, one dynamic pressure sensor, and one barometric pressure sensor. Piccolo has special sensor configuration sections to correct errors like IMU to GPS antenna offset, avionics orientation with respect to the body frame.



Fig. 2.4: Piccolo LT autopilot.

Piccolo LT has a 40 MHz MPC555 onboard microcontroller. Piccolo provides a universal controller with different user configurations including legacy fixed wing controller, neutral net helicopter controller, fixed wing generation two controller, and PID helicopter controller. Fixed wing generation two controller is the most commonly used flight controller for conventional fixed wing UAVs. It includes support for altitude, bank, flaps, heading and vertical rate hold, and auto take-off and landing. Piccolo autopilot supports one ground station controlling multiple autopilots and hardware-in-the-loop simulations.

Paparazzi Autopilot

Paparazzi autopilot is a popular project first developed by researchers from Ecole Nationale de l'Aviation Civile (ENAC) University, France. Infrared sensors combined with GPS are used as the default sensing unit. Although infrared sensors can only provide a rough estimation of the attitude, it is enough for a steady flight control once tuned well. Paparazzi Tiny 13 is the autopilot hardware with the GPS receiver integrated, shown in Fig. 2.5. Paparazzi also has Tiny without GPS (TWOOG) autopilot with two open serial ports, which can be used to connect with IMU and modem. A Kalman filter runs on the

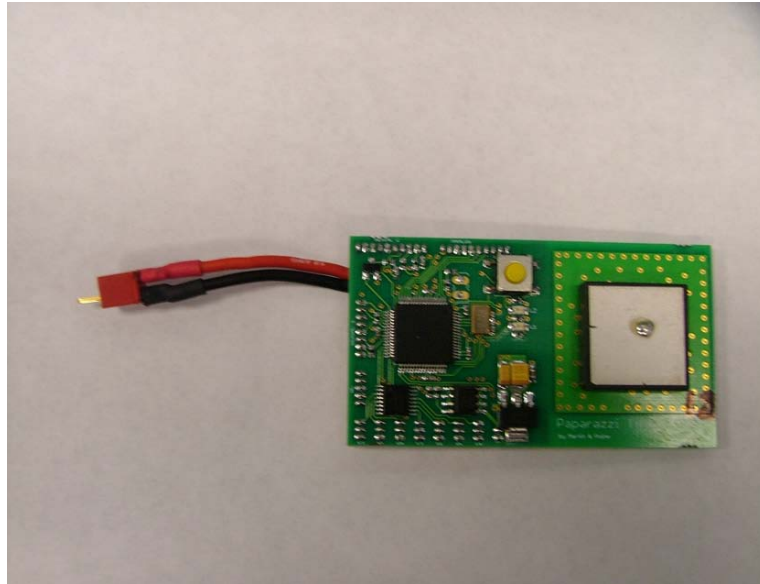


Fig. 2.5: Paparazzi autopilot tiny 13.

autopilot to provide a faster position estimation based on GPS updates.

Paparazzi autopilot uses LPC 2148 ARM7 chip as the central processor. It can achieve waypoints tracking, auto-takeoff and landing, and altitude hold. The flight controller can also be configured if a rate gyro is used for roll and pitch tracking on micro UAVs. However, Paparazzi autopilot does not have supports for speed holding currently since no air speed sensor reading is considered in the controller part. Paparazzi autopilot is also a truly autonomous autopilot without any dependance on the ground control station (GCS). It has many safety considerations such as exceptional handing in conditions like RC signal lost, out of predefined range, GPS lost, etc.

Specification Comparisons

The physical specifications of the autopilots are important since small UAVs demand as fewer space, payload, and power as possible. The size, weight, and power consumption specifications are shown in Table 2.2. The functional specifications of these three typical autopilot are listed in detail in Table 2.3.

Table 2.2: Comparison of physical specifications of autopilots.

	Kestrel 2.2 (GPS not included)	Piccolo LT (w. modem)	Paparazzi TWOG (IR not included)
Size (cm)	5.08*3.5*1.2	11.94*5.72*1.78	4.02*3.05*1
Weight (g)	16.7	45	8
Power	500 mA (3.3 or 5 V)	5 W	N/A
Price (\$)	5000	-	125
DC In (V)	6-16.5	4.8-24	6.1-18
CPU (MHz)	29	40	60
Memory (K)	512	448	512

Table 2.3: Comparison of autopilot functions.

	Kestrel	Piccolo LT	Paparazzi TWOG
Waypoints Navigation	Y	Y	Y
Auto-takeoff and landing	Y	Y	Y
Altitude Hold	Y	Y	Y
Air Speed Hold	Y	Y	N
Multi-UAV Support	Y	Y	Y
Attitude Control Loop	-	-	20/60 Hz
Servo Control Rate	-	-	20/60 Hz
Telemetry Rate	-	25 Hz or faster	Configurable
Onboard Log Rate	≤100 Hz	-	N

2.3 AggieAir UAS Platform

Most current autopilot systems can guide the UAVs to navigate through waypoints. However, it is not enough for real-world remote sensing applications because end users need aerial images with certain spatial and temporal resolution requirements. More importantly, most civilian remote sensing users require the UAV platform to be expendable. AggieAir UAS platform is developed considering all these remote sensing requirements. AggieAir is a small and low-cost UAV remote sensing platform, which includes the flying-wing airframe, the OSAM-Paparazzi autopilot, the GhostFoto image capture subsystem, the Paparazzi ground control station (GCS), and the gRAID software for aerial image processing. All the subsystems are introduced in this section.

2.3.1 Remote Sensing Requirements

Let $\Omega \subset R^2$ be a polytope including the interior, which can be either convex or non-convex. A series of band density functions $\eta_{rgb}, \eta_{mir}, \eta_{mir} \dots$ are defined as $\eta_i(q, t) \in [0, \infty)$ $\forall q \in \Omega$. η_{rgb} can also be treated as three bands η_r, η_g, η_b , which represent RED, GREEN, and BLUE band values of a pixel. The goal of remote sensing is to make a mapping from Ω to $\eta_1, \eta_2, \eta_3 \dots$ with preset spatial and temporal resolutions for any $q \in \Omega$ and any $t \in [t_1, t_2]$ [17].

With the above remote sensing requirements, several specific characteristics need to be considered to get accurate georeferenced aerial images aside from an autonomous flying vehicle:

- Expense: Most civilian applications require expendable UAS platforms instead of expensive military grade unmanned vehicles. However, most commercial-off-the-shelf (COTS) autopilots cost more than \$6000, let alone the camera and the air frame.
- Orientation Data: The orientation information when the image is taken is critical to the image georeferencing. Although the IR sensors can guide the UAV for autonomous flight, it is not enough for accurate georeferencing.
- Image Synchronization: Some COTS UAVs can send videos down to the base station for further processes. But there is a problem that the picture may not match up perfectly with the UAV data from the data log. The images may not synchronize perfectly with the orientation data from the autopilot.
- Band configurable ability: Many remote sensing applications require more than one band of aerial images such as vegetation mapping and some of them may require RGB, NIR, and even thermal images simultaneously.

2.3.2 AggieAir System Structure

AggieAir UAS includes the following subsystems:

- The flying-wing airframe: Unicorn wings with optional 48", 60", and 72" wingspans are used as the frame bed to fit in all the electronic parts. The control actuators include elevons and a throttle motor.
- The OSAM-Paparazzi autopilot: The open-source Paparazzi autopilot is modified by replacing the IR sensors with the IMU as the main sensing unit. Advanced navigation routines such as surveying an arbitrary polygon are also developed to support image acquisition of an area with a more general shape [35].
- The GhostFoto imaging payload subsystem [36]: A high-resolution digital imaging subsystem with both the RGB and NIR bands is developed. More importantly, the image system could guarantee an accurate synchronization with the current autopilot software. COTS imaging payloads can also be fit on AggieAir UAVs including the analog video camera (VC) and the thermal camera.
- The communication subsystem: AggieAir has a 900 MHz data link for GCS monitoring, a 72 MHz RC link for safety pilot backup and an optional 2.4 GHz WiFi link for real-time image transmission.
- The Paparazzi ground control station (GCS): Paparazzi open-source ground station is used for the real-time UAS health monitoring and flight supervising.
- The gRAID software [35]: A new NASA World Wind [37] plug-in named gRAID is developed for aerial image processing including correcting, georeferencing, and displaying the images on a 3D map of the world, similar to GoogleEarth.

There are two types of AggieAir UAVs developed and fully tested at CSOIS. AggieAir1 UAV is typically equipped with IR sensors for navigation and analog DV for the image acquisition. AggieAir2 UAV is equipped with the commercial IMU for navigation and high-resolution GhostFoto imaging subsystem. The physical structure of AggieAir2 UAV is shown in Fig. 2.6, with the specifications in Table 2.4 and the airborne layout in Fig. 2.7 and Fig. 2.8.

AggieAir UAS has the following advantages over other UAS platforms for remote sensing missions:

- Low costs: AggieAir airborne vehicles are built from scratches including the airframes and all the onboard electronics. The total hardware cost is around \$3500.

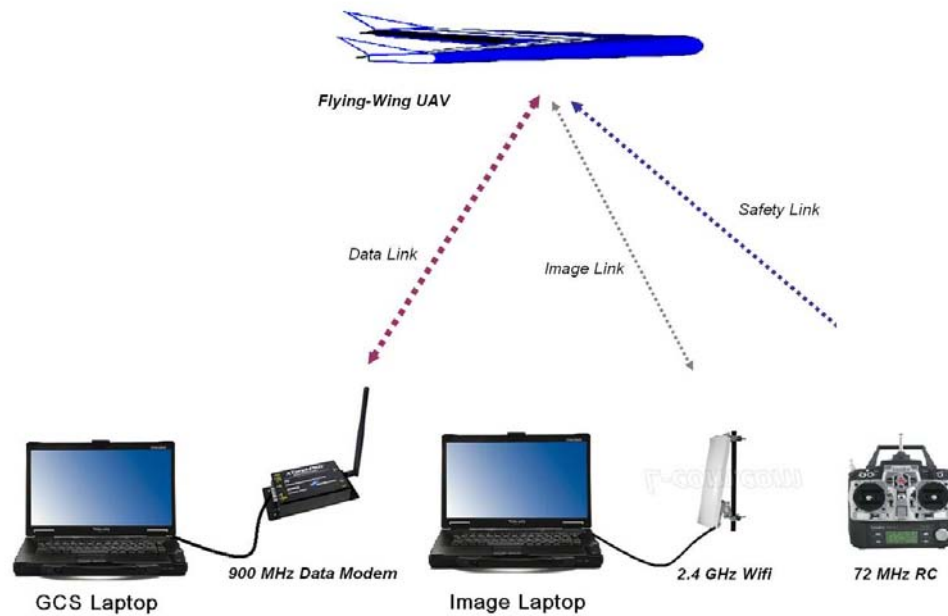


Fig. 2.6: AggieAir UAS physical structure.

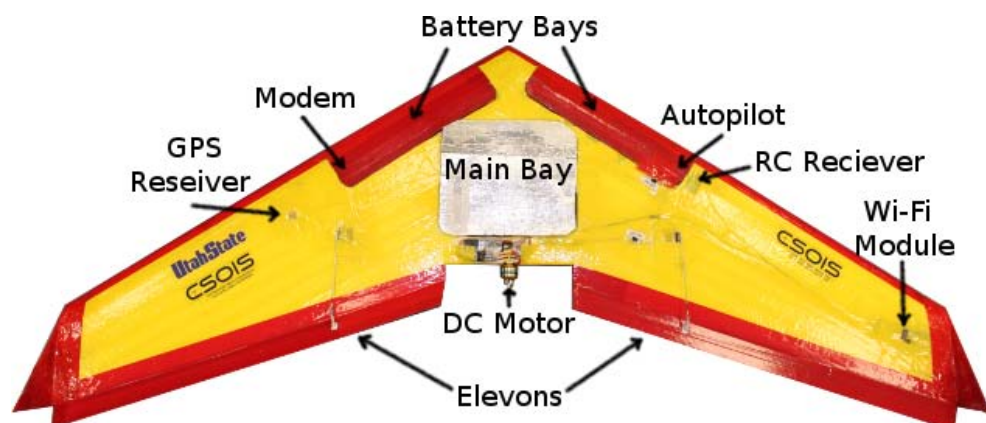


Fig. 2.7: AggieAir2 UAS airborne layout.

- Full autonomy: AggieAir uses the Paparazzi autopilot, which supports the full autonomy of the aerial vehicle even without the ground station.
- Easy manipulation: Only two people are required to launch, manipulate, and land the vehicle.
- Run-way free capability: The bungee launching system supports take-off and landing basically at any soft field with only one launching operator.

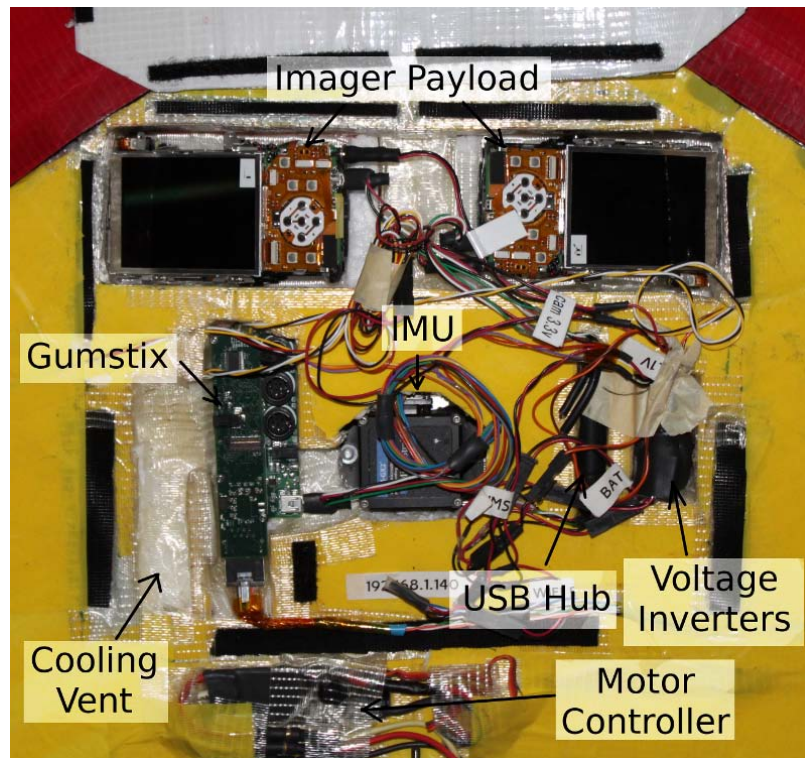


Fig. 2.8: AggieAir2 main bay layout.

Table 2.4: AggieAir2 UAS specifications.

	Specifications
Weight	up to 8 lbs
Wingspan	72"
Flight Time	≤ 1 hour
Cruise Sped	15 m./sec.
Imaging Payload	RGB/NIR/thermal camera
Operational Range	up to 5 miles

- High spatial and temporal resolutions: The image system can achieve submeter-level ground resolution and hour-level time accuracy.
- Multiple spectral bands for imaging payloads: AggieAir supports RGB, NIR, and thermal bands for current image subsystems. More band configurable imagers are also under developments.

2.3.3 Flying-Wing Airframe

The airframe together with the actuators have a big impact on the UAV flight performance. It requires careful considerations to fit in all the sensors, actuators, and other subsystems. The flying-wing, or delta-wing airframe is chosen as the research development platform due to its simplicity to build [33]. The flying-wing airframe is defined as the wings with no definite fuselage or tail. Theoretically, it is the most efficient aircraft design considering the aerodynamics and structural weight [38]. The Unicorn wing used in CSOIS includes 48", 60", and 72" wingspan [39], shown in Fig. 2.9, after gluing and taping.



Fig. 2.9: Unicorn wing.

The Unicorn flying-wing airframe has two control surfaces (left and right elevon) and one throttle motor to power the propeller. The Li-Poly batteries are chosen as the power sources due to their high-power density and light weights. Because of the current constraints from the batteries, both the throttle motor and the propeller need to be carefully selected to maximize the power efficiency while providing enough thrusts.

The major considerations while designing the airborne layout of the flying wings are to minimize the drag and choose the right center of gravity (CG). Most airborne parts like the batteries and inner electronics are embedded inside the airframe and covered with plastic cases to prevent irregular flows, shown in Fig. 2.7. In addition, the aerodynamic shapes are designed for the cameras that have to reach out of the airframe. With the drag minimized, another very important design parameter is the position of the CG. The neutral point of all wings is at about 1/4 chord line [38]. The center of gravity of flying wing airframes could be approximately calculated as follows [40]:

$$CG = \frac{d_s(c_r + 2c_t)}{3(c_r + c_t)} + b_p\%(c_r - \frac{2(c_r - c_t)(0.5c_r + c_t)}{3(c_r + c_t)}), \quad (2.1)$$

where b_p is the percentage of the balance point on the mean aerodynamic chord, d_w is the wing span, c_r is the root chord, c_t is the tip chord, and d_s is the sweep distance. All the parameters above are defined in Fig. 2.10.

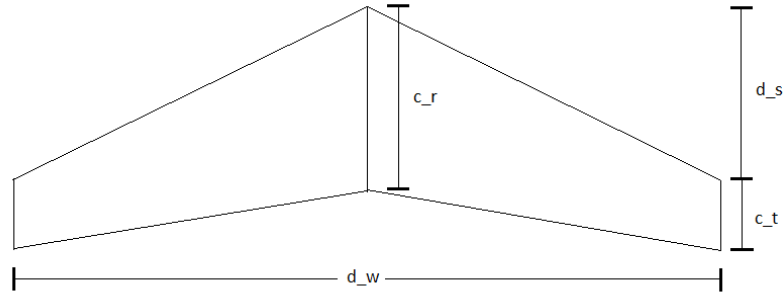


Fig. 2.10: CG calculation for flying wings.

After the theoretical position of the CG is calculated, the layout can be designed to minimize the moment while turning. Most flying-wing airframes are designed to be a little nose heavy to have a positive pitching moment for the stability issues [41].

2.3.4 OSAM-Paparazzi Autopilot

It is clear that Kestrel and Piccolo autopilots are small, light, and powerful. But their prices are relatively high and most of their onboard software is not accessible to users, which is a main disadvantage when georeferencing aerial images after the flight [42]. Paparazzi UAV project provides a cheap, robust, and open-source autopilot solution including both hardware and software. But it uses infrared sensors for the attitude measurement, which is not accurate enough compared with most commercial UAV autopilots.

To achieve an accurate image georeferencing with a fair price, an inertial measurement unit (IMU) is added to the Paparazzi autopilot replacing the IR sensors. The detailed interface design is explained in later sections. Paparazzi TWOG board is used together with a 900 MHz Maxstream modem for real-time communication to the GCS. Microstrain GX2 IMU and u-blox LEA-5H GPS receiver serve as the attitude and position sensors, respectively. Due to the limits from the IO ports, the Gumstix microprocessor [43] is used as a bridge to connect IMU and GPS to the TWOG board. The cascaded PID flight controller then converts all the sensor information into PWM signals for the elevon and throttle motor to guide the vehicle for preplanned navigation. There is also a 72 MHz RC receiver on board so that the human safety pilot can serve as the backup for the autopilot in case of extreme conditions like strong wind gusts. The physical connections of the airborne system is shown in Fig. 2.11.

2.3.5 OSAM Image Payload Subsystem

To achieve the final goal of measuring the density functions of different bands simultaneously, two types of image subsystems have been developed including GhostFinger and GhostFoto subsystems. GhostFinger subsystem is a stand-alone payload that could either output streams of videos or trigger the picture capture by itself [35, 44]. GhostFoto is

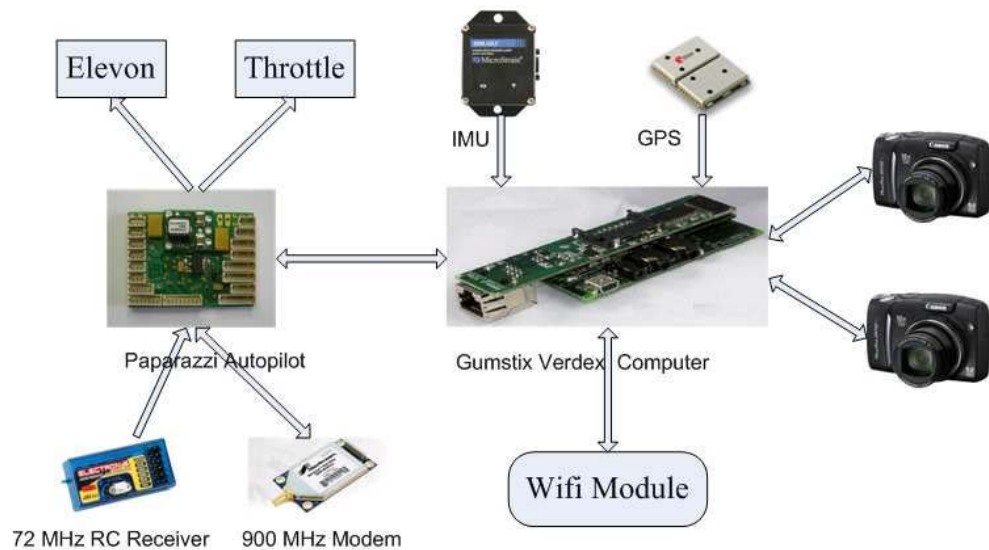


Fig. 2.11: AggieAir airborne system structure.

a high-resolution imager that is connected with the IMU/GPS for more accurate image georeferencing [36].

GhostFinger Subsystem

The weight, shape of the imager, and manner in which the imager is mounted, can significantly affect UAV flight dynamics. Due to the physical limitations of a small UAV platform, the embedded imager must be small, light, and consume low power. Four types of embedded imagers have been developed for small UAV applications: Ghost Finger RGB digital camera (GF-RGB-DC), Ghost Finger NIR digital camera (GF-NIR-DC), Ghost Finger RGB digital video camera (GF-RGB-DV), and Ghost Finger NIR digital video camera (GF-NIR-DV) [44].

Analog Video Camera: GF-DV is developed for real-time image transmission. It is comprised of a single board analog 1/4" CCD camera, one 2.4 GHz Black Widow wireless video transmitter, and peripheral circuits. The CCD camera only weighs about 7.09 grams. The camera specifications are shown in Table 2.5 [44] and GF-DC is shown in Fig. 2.12 and Fig. 2.13 [44]. The communication range for the wireless transmitter and receiver can be

up to one mile with the 3 dB antenna. The power consumption of the imager is estimated similarly with one 7.4 V Li-Poly battery and a voltage regulator. The GF-DV requires a wireless video receiver to get the video back in real-time.

RGB + NIR Digital Camera: The “Ghost Finger digital camera” (GF-DC) is developed from a Pentax OPTIO E30 digital camera. Three photo capturing modes are included: timer triggered, RC triggered, and digital switch triggered. An ATMEG8L microcontroller is embedded with the camera to serve as a camera trigger controller. The timer trigger shot mode is for aerial photo capturing with a preset shooting interval t_{shoot} . The RC triggered mode is to use a spare channel from RC transmitter and receiver to control the picture capture manually via RC. The switch triggered shot mode is for triggering from the UAV autopilot to achieve a better geospatial synchronization. The camera specifications are shown in Table 2.6 [44] and GF-DC is shown in Fig. 2.14 and Fig. 2.15 [44]. The power consumption of the imager is estimated as an average value powered by one 3.7 V Li-Poly battery with 950 mA-hour capacity. The images are saved on an SD card within the camera. The GF-DC has been tested to work for more than one hour in timer triggered mode with one 1GB SD card and a 3.7 V Li-Poly battery (950 mA-hour).

Table 2.5: Ghost Finger digital video camera specifications.

Dimension:	22 × 16 mm
Weight:	≤ 100 g (including transmitter)
Power Consumption:	about 600 mA at 5 V
Pixel Size:	768 × 494
Focal Length:	1.9 mm
Pixel Pitch:	4.75 (h) × 5.55 (v) μm

Table 2.6: Ghost Finger digital camera specifications.

Dimension:	6"
Weight:	174 g (battery not included)
Power Consumption:	about 700 mA at 3.3V
Pixel Size:	3072 × 2112
Focal Length:	6 to 18 mm
Pixel Pitch:	about 1.8 × 1.8 μm

Most CCD chips used on cameras are only sensitive to the electromagnetic light with a spectral wavelength ranging from 400 to 1100 nm, which includes both the visible band and NIR band. Digital cameras use an IR blocking filter to block wavelengths above 750 nm. A CCD-based camera can be changed into an NIR sensor by removing the IR blocking filter and adding one visual band blocking filter. A Lee 87 NIR filter is used in our GF-DC and GF-DV to block the light with the wavelength smaller than 730 nm. So, the Ghost Finger NIR imager has a band of about 730-1100 nm. The NIR filter is added on both GF-DC and GF-DV to form a array of two imagers, which can measure the RGB and NIR simultaneously.

GhostFoto Imaging Subsystem

GhostFoto imaging subsystem is the second generation remote controlled digital camera system developed at CSOIS [45]. The hardware includes the Canon CCD camera for image capture and the Gumstix microprocessor for payload control and georeferencing logging. Canon PowerShot SX100 IS CCD camera is used, shown in Fig. 2.16 [36]. This camera has



Fig. 2.12: Ghost Finger video camera.



(a) Front view.

(b) Back view.

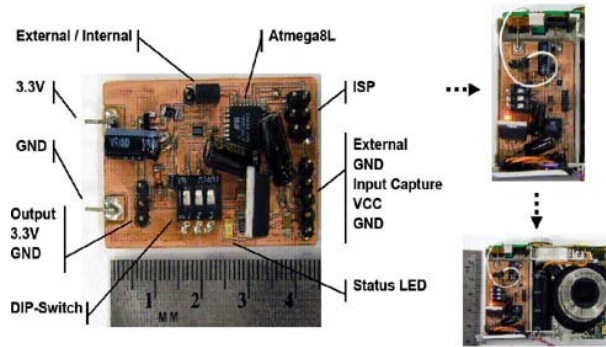
Fig. 2.13: Ghost Finger video camera 2×1 .

Fig. 2.14: Ghost Finger digital camera.

the remote capturing capability, an 8-mega pixel CCD panel supporting up to 3264 by 2448 pixels size and a $10\times$ optical zoom lens with optical image stabilizer. The compact size and relatively light weight (265 grams) of this camera make it easy to fit the camera on small UAVs. Besides the commonly used RGB bands, the camera can also support near infrared spectra by replacing the visible light filter with an NIR filter. Our 72" airframe can carry two or three of these imagers with different bands after removing unnecessary parts.

GFoto cameras are remotely controlled by the Gumstix through USB 1.1 interface with GhostEye image capture software. GhostEye is based on `libgphoto2` [46], which is an open-source portable digital camera library of C functions for UNIX-like operating systems. With `libgphoto2` library functions, GhostEye is able to remotely control and configure



Fig. 2.15: Ghost Finger DC packages.

multiple cameras simultaneously through a Picture Transfer Protocol (PTP) driver. PTP is a widely supported protocol developed by the International Imaging Industry Association for transfer of images from digital cameras to computers [47]. GhostEye also provides the communication link between the payload and the UAV system. Messages can be transmitted from GhostEye to the ground station, or can be shared among UAVs with the same protocol. Meanwhile, messages from the UAV system can trigger the imagers. For example, after the desired altitude is reached, the UAV is able to command the imager to activate or deactivate capturing. The georeferencing data is logged by GhostEye in XML format for easy imports to the gRAID [35].

2.3.6 gRAID Image Georeference Subsystem

The Geospatial Real-Time Aerial Image Display (gRAID) is a plug-in for NASA World Wind, serving as a 3D interactive open-source world viewer [35]. gRAID takes the raw aerial images, makes corrections for the camera radial distortion, and then overlays the images on the 3D Earth based upon the position and orientation data collected when they are captured. This process can be done either in real-time while the plane is flying or after the flight. Human-in-the-loop feature-based image stitching or mosaicing can be done with conventional GIS software after gRAID exports the image to a world file. gRAID can also create a gray scale image from a single RGB channel. The images can be converted into world files and loaded into conventional GIS software for further advanced image processing.



Fig. 2.16: Camera body (left) and its CCD sensor (right).

The detailed georeferencing procedure is described as below.

To georeference the aerial images, several coordinate systems must first be defined, as shown in Fig. 2.17 [35].

- The body frame: The origin is defined at the center of gravity (CG), with the x axis pointing through the nose, the y axis pointing to the right wing, and the z axis pointing down.
- The camera frame: The origin is located at the focal point of the camera. The axes of the camera frame are rotated by ϕ_c , θ_c , and ψ_c with respect to the body frame.
- The inertial frame: The origin is usually defined on the ground with the x , y , z axes pointing towards the north, east, and down, respectively. The orientation of the UAV with respect to the inertial frame is given by ϕ , θ , and ψ .
- The Earth-centered Earth-fixed (ECEF) frame: The z axis passes through the north pole, the x axis passes through the equator at the prime meridian, and the y axis passes through the equator at 90° longitude.

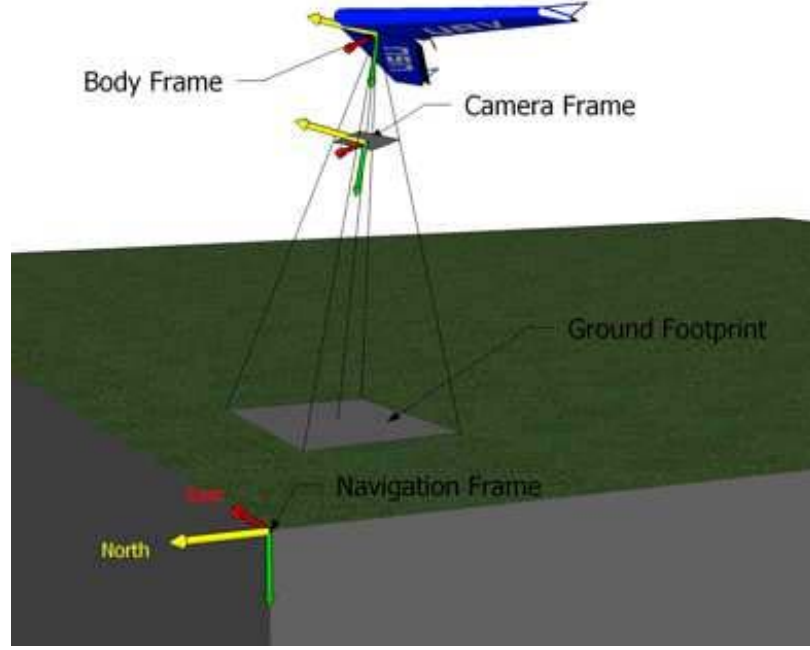


Fig. 2.17: Aircraft coordinate systems.

Any point in an image can be rotated from the camera frame to the ECEF coordinate system in order to find where it is located on the Earth. However, it is only necessary to find the location of the four corners of the image in order to georeference it. Assuming the origin is at the focal point and the image is on the image plane, (2.2) can be used to find the four corners of the image. As defined in Fig. 2.18 [35], FOV_x is the FOV around the x axis, FOV_y is the field of view (FOV) around the y axis, and f is the focal length,

$$\begin{aligned}
 v_c^1 &= \begin{bmatrix} f \tan(FOV_y/2) & -f \tan(FOV_x/2) & f \end{bmatrix}, \\
 v_c^2 &= \begin{bmatrix} f \tan(FOV_y/2) & f \tan(FOV_x/2) & f \end{bmatrix}, \\
 v_c^3 &= \begin{bmatrix} -f \tan(FOV_y/2) & -f \tan(FOV_x/2) & f \end{bmatrix}, \\
 v_c^4 &= \begin{bmatrix} -f \tan(FOV_y/2) & f \tan(FOV_x/2) & f \end{bmatrix}.
 \end{aligned} \tag{2.2}$$

To rotate the corners into the navigation frame, they first need to be rotated to the

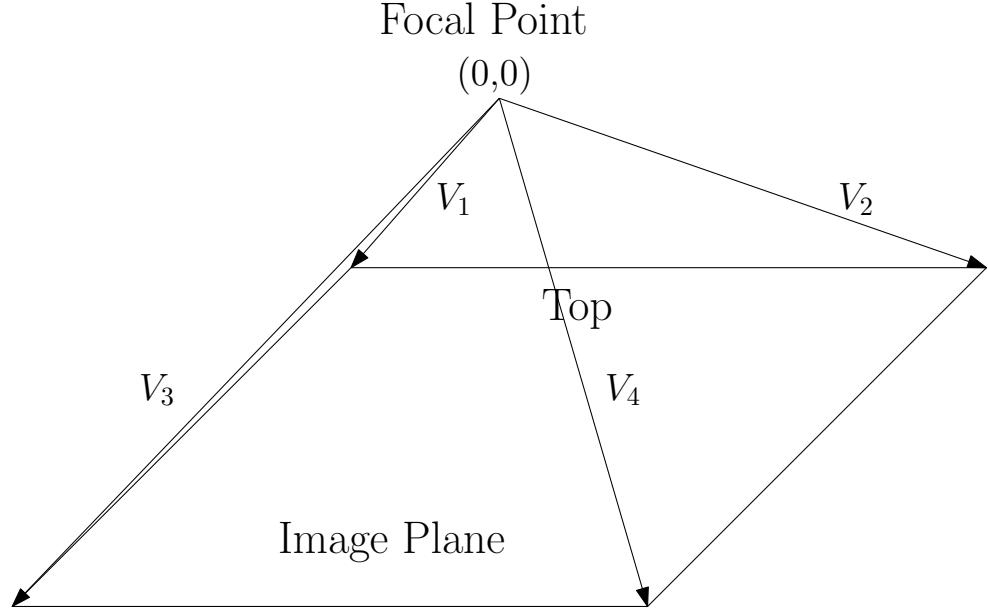


Fig. 2.18: Definition of initial image corners.

body frame. The Euler angles with respect to the body frame are given by ϕ_c , θ_c , and ψ_c , and can be used to create a clock-wise rotation matrix R_c^b which rotates a vector in the body frame to the camera frame,

$$R_c^b = R_{xyz}(\phi_c, \theta_c, \psi_c). \quad (2.3)$$

To rotate from the camera frame to the body frame, the transpose of R_c^b is used.

$$R_b^c = (R_c^b)^T = R_{zyx}(-\theta_c, -\psi_c, -\phi_c) \quad (2.4)$$

The same rotation matrix is used, with ϕ , θ , and ψ to rotate from the body frame into the navigation frame,

$$R_n^b = (R_b^n)^T = R_{zyx}(-\theta, -\psi, -\phi). \quad (2.5)$$

Now each corner is rotated from the camera frame into the navigation frame using (2.6),

$$v_n^i = R_n^b R_b^c v_c^i. \quad (2.6)$$

Since the corners are in the NED coordinate system, they can be scaled to the ground to find their appropriate magnitude (assuming flat Earth) where h is the height of the UAV above the ground and $v_n^i(z)$ is the z component of v_n^i .

$$v_n^i = v_n^i \frac{h}{v_n^i(z)} \quad (2.7)$$

The next step is to rotate the image corners into the ECEF coordinate system. This is done with another rotation matrix and the latitude (λ) and longitude (α) of the UAV, i.e.,

$$R_w^n = R_{zyy}(-\alpha, \frac{\pi}{2}, \lambda), \quad (2.8)$$

$$v_w^i = R_w^n v_n^i. \quad (2.9)$$

After the corners are rotated into the ECEF coordinate system, they are located in the center of the Earth and need to be translated up to the position of the UAV in Cartesian coordinates (p),

$$v_w^i = v_w^i + p. \quad (2.10)$$

So, v_w^i now represents the position of each of the image corners, in Cartesian coordinates, projected on the Earth.

2.4 OSAM-Paparazzi Interface Design for IMU Integration

One of our major breakthroughs of OSAM-Paparazzi autopilot is the integration of the IMU to the Paparazzi autopilot. The advantages to replace the default IR sensors include more accurate flight performance, easier controller tuning, and more accurate image georeferencing results. Due to the price and time requirements, the stand-alone IMU (Microstrain GX2) with orientation outputs is chosen for the AggieAir2 UAV instead of the IMU with GPS integrated (e.g., Xsens Mti-g). The Microstrain GX2 IMU has a RS232 interface [22] and the GPS receiver has a UART interface. With the above hardware, the following constrains for the OSAM-Paparazzi interface design must be considered:

- The interface needs to collect data from the GPS and IMU both through serial ports;
- The only two UARTs of Paparazzi autopilot are already used by GPS and data modem;
- The digital cameras need one more processor for remote control and image logging;
- The onboard devices need to be light, small, and stable to put on the UAV;
- The hardware and software modifications should be minimized due to the time constraints;
- The onboard devices need to be powerful for later onboard image processing and inter-UAV communication purposes.

2.4.1 Hardware Interface Connections

Based on the above constraints, mostly the IO limits, the Gumstix is chosen to serve as both the imager controller and the bridge to connect the sensors to the Paparazzi autopilot. The Gumstix Verdex Pro XM4 board has a 400 MHz PXA270 processor and 64M RAM with the embedded Linux system [43]. The Verdex Pro mother board is connected with a Console-VX board for extra IOs including three RS232 Mini-DIN8 ports and one USB port, shown in Fig. 2.19. There are also three UART ports on the Console-VX board, which can take in TTL logic level (3.3V) signals, shown in Table 2.7.

The Microstrain GX2 IMU is connected with the Gumstix through the Mini-DIN8 port, shown in Fig. 2.20(a). Both the GPS module and the Paparazzi autopilot are connected through the UARTs, shown in Fig. 2.20(b).

Table 2.7: Serial mapping of Gumstix Console-VX board.

<i>Dev ID</i>	<i>UART ID</i>	<i>DIN8 Position</i>	<i>Default Function</i>	<i>Max Rate</i>
/dev/ttyS0	FFUART	Middle	Default Linux Console	230kbps
/dev/ttyS1	BTUART	Upper	Blue Tooth Comm.	921kbps
/dev/ttyS2	STUART	Corner	General Purpose	230kbps

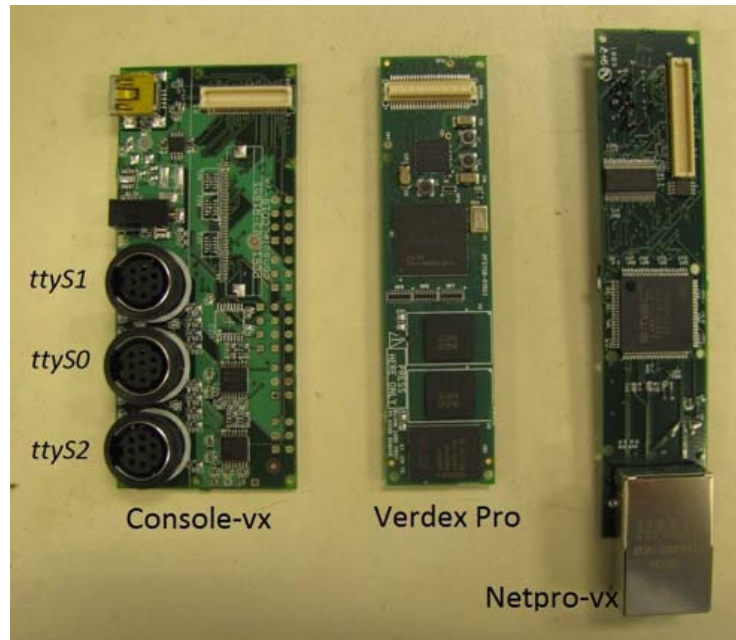
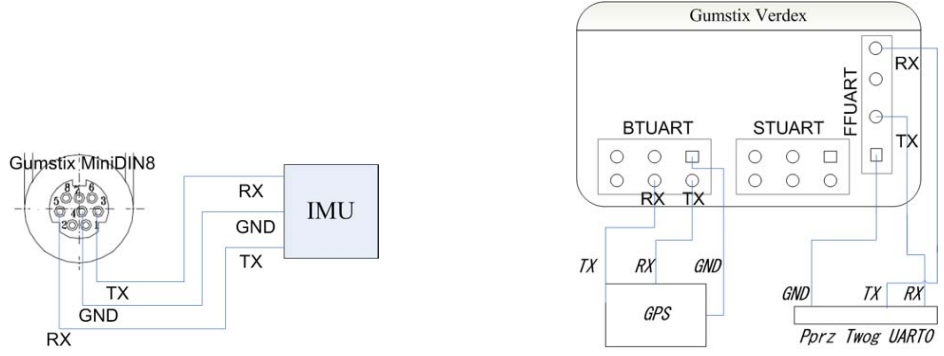


Fig. 2.19: Gumstix Verdex and Console-VX boards.

2.4.2 Software Interface Design

Given the above hardware, two interface software programs are developed. They are (1) GhostGX2 interface running on Gumstix, and (2) OSAM-IMU interface running on Paparazzi autopilot. Both interfaces are written in C for compatibility and efficiency considerations. The GhostGX2 interface has the following functions (in priorities):

- Collect data in bytes from the IMU and GPS *in real-time*;
- Parse the data when the whole packet is ready;
- Transmit the orientation, position, and velocity data to the Paparazzi autopilot *in real-time* for control purposes;
- Control the onboard cameras remotely when needed;
- Share the orientation and position data with the image part for later georeferencing purposes;



(a) Gumstix to GX2 IMU.

(b) Gumstix to GPS and Paparazzi TWOG.

Fig. 2.20: OSAM-Paparazzi hardware connection.

- Transmit the GPS accuracy data and satellite data to the Paparazzi autopilot for monitoring purposes;
- Log all the raw sensor data on the Gumstix for emergency analysis and further data filtering.

Although the Gumstix Verdex has powerful computational abilities (400 MHz), the fast IO manipulations, like camera control and real-time logging (50 or 100 Hz), can still slow down the program and may affect the real-time communication with the autopilot. Thus, GhostGX2 is designed to run in multiple threads to avoid the interference from the slow IOs. The image thread and the logging thread are singled out with only global variable sharing through memory copy in a slow speed (every second or several seconds). The program flow chart of GhostGX2 is shown in Fig. 2.21. The Algorithms 2.4.1 and 2.4.2 are designed to achieve the predefined functions. The communication protocols of several representing IMUs and GPS are provided in Appendix A. The implementation details of GhostGX2 are introduced in Appendix B. The imaging thread implementation is also similarly implemented [45].

The Paparazzi airborne code also needs to be modified slightly to be able to understand the data from the Gumstix. The designed OSAM-IMU interface on Paparazzi autopilot can achieve the following functions:

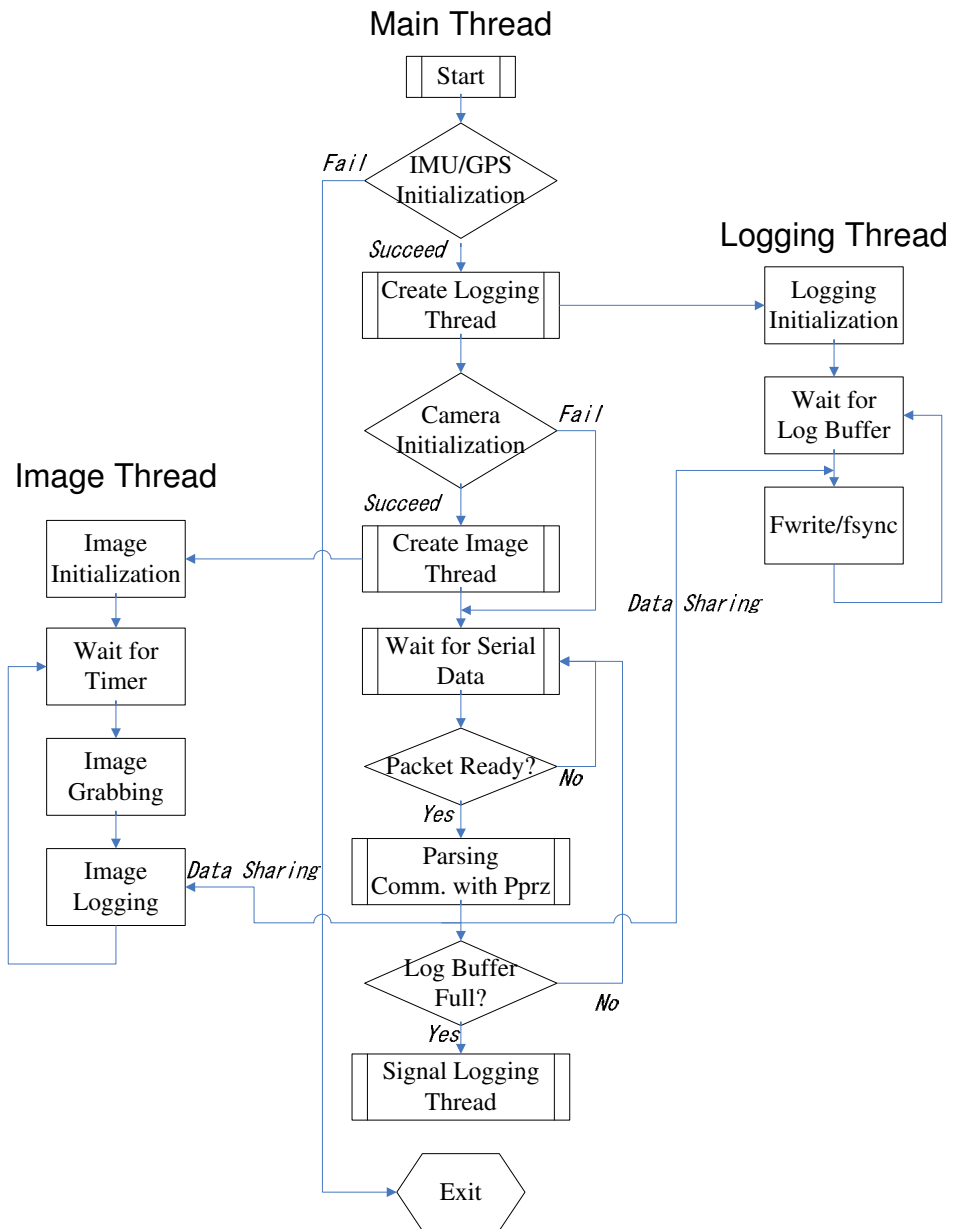


Fig. 2.21: Flow chart of GhostGX2.

- Collect the orientation, position, velocity, and GPS data from the Gumstix;
- Collect the GPS accuracy and satellite information from the Gumstix;
- Parse the data when the packet is ready;
- Update the attitude and GPS variables in the memory.

Algorithm 2.4.1. GhostGX2 Interface

```

while(1){
    ...
    select(imu, gps);                /* Wait data from imu and gps */
    parse_data();
    if (packet_ready)
        osam_link_pprz();           /* Transmit to Paparazzi. */
    ...
    pthread_mutex_lock(andmutex);     /* Main thread locks log buff */
    write_global_log_buf();
    if (log_buf_ready)
        pthread_cond_signal(andlog_buf_ready); /* Signal the log thread */
    pthread_mutex_unlock(andmutex);
    ...
    pthread_mutex_lock(andmutex2);    /* Main thread locks image buff */
    write_global_image_buf();
    pthread_mutex_unlock(andmutex2);
    ...
}

```

Algorithm 2.4.2. Real-Time Logging

```

while(no_error){
    ...
    pthread_mutex_lock(andmutex);     /* Log thread locks log buff */
    pthread_cond_wait(andlog_buf_ready, andmutex);
    global_buf_sharing();
    pthread_mutex_unlock(andmutex);
    ...
    fwrite(andglobal_buf, log_file);
    fflush(log_file);
    fsync(log_file);                 /* Time-consuming IO manipulations */
    ...
}

```

The OSAM-IMU files written in C are added on the airborne codes with the program flow chart shown in Fig. 2.22. The whole data receiving and parsing parts are implemented in an interrupt or event task. The communication protocol between Gumstix and Paparazzi is defined in Table 2.8. The packet types received on the Paparazzi autopilot are defined in Table 2.9.

2.5 AggieAir UAS Test Protocol and Tuning

With the new GhostGX2 interface added to Paparazzi autopilot, it is very important to test the whole AggieAir system for both the functionality and robustness. Besides, many controller parameters and exceptional values need to be determined based on our specific UAV platform. Both the test protocol and the controller tuning procedure are developed in this dissertation work.

2.5.1 AggieAir UAS Test Protocol

To maximize the outcome of the flight test results and minimize the potential property damages, the AggieAir UAS Test Protocol is developed for the whole testing procedure with any airborne code modifications. A series of flight test preparation and manipulation documents are developed, shown in detail in the Appendix C. The whole code test procedure

Event Task (Interrupt)

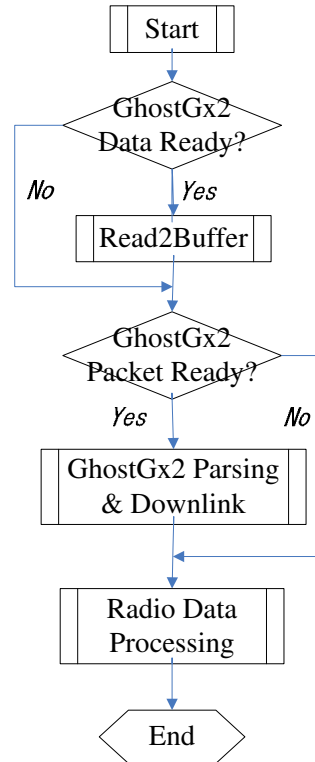


Fig. 2.22: Flow chart of OSAM interface on Paparazzi autopilot.

is as follows, shown in Fig. 2.23. First, each problem is analyzed and attacked separately. Then, the code is developed and verified on the ground. All the new functions are tested in the lab first before the flight test. Finally, the real flight tests serve as the feedback for the testing procedure.

One example of ground test is shown in Table 2.10. This ground test was for monitoring the memory and CPU usage of GhostGX2. Top is used to get the Gumstix resource information. GhostGX2 is left running for more than an hour with the camera capturing every five second. It can be seen that the memory used only increased slowly due to the slow speed of the data logging and the system is stable enough during the designed maximal time period.

2.5.2 AggieAir Controller Tuning Procedure

The flight control system of Paparazzi autopilot comprises of several cascaded PID controllers, which need some tunings for every specific airframe. A well-tuned controller can maximize the flight time and minimize the probability of stalling. A special controller tuning procedure is developed here for our flying-wing airframes.

The key controller parameters of Paparazzi autopilot include [48]:

- `nominal_speed`, the default ground speed;

Table 2.8: Communication protocol between Gumstix and Paparazzi.

Bytes	1	2	3	4	5 ~ 4+LEN	5+LEN	6+LEN
	93	E0	ID	LEN	PAYLOAD	CHECKSUM1	CHECKSUM2

Table 2.9: Packet definition for data from GhostGX2.

Packet ID	Length (byte)	Rate (Hz)	Description
0	38	4	GPS position, velocity, and accuracy
1	12	50	Orientation
2		1	GPS status and satellite infor.
3		0.5	Image capturing info.

- `cruise_throttle`, the default throttle percentage in steady flights;
- `default_circle_radius`, the default turning radius;
- `roll_neutral`, for the compensation on the roll channel caused by building asymmetries;
- `pitch_neutral`, for the default angle of attack during steady flights;
- `roll_pgain`, k_p of the roll loop P-controller;
- `pitch_pgain`, k_p of the pitch loop P-controller;
- `course_pgain`, k_p of the course loop PI-controller;
- `altitude_pgain`, k_p of the altitude loop PI-controller.

Based extensive flight test experiences, Algorithm 2.5.1 is summarized for the controller tuning of AggieAir UAV platforms.

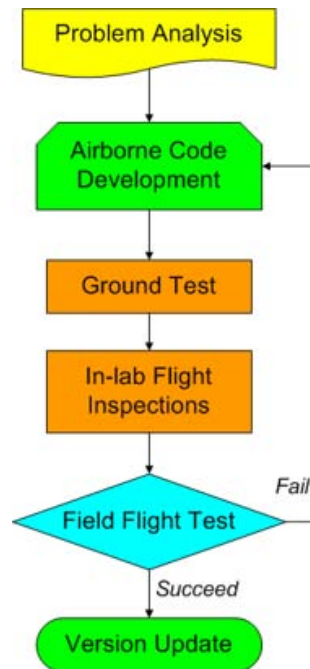


Fig. 2.23: AggieAir UAS test protocol.

Algorithm 2.5.1. *The OSAM-UAV controller tuning procedure can be described as below:*

- (1) *Set up default values for all the parameters based on RC flight performance;*
- (2) *Trim tuning in manual mode to achieve the steady flight at the preset cruise_throttle;*
- (3) *Pitch-loop rough tuning (pitch_neutral, pitch_pgain) to guarantee no altitude loss while flying straight in Auto1 mode;*
- (4) *Roll-loop rough tuning (roll_neutral, roll_pgain) for the symmetry of left and right circle in Auto1 mode;*
- (5) *Pitch-loop and roll-loop fine tuning while following the flight pattern of straight line following, left circling, and right circling (Auto2 mode);*
- (6) *Course-loop tuning in Auto2 mode.*

2.6 Typical Platforms and Flight Test Results

Both AggieAir1 and AggieAir2 UAV platforms have been built and fully tested at CSOIS for different purposes. The autonomous flight data shown in the flight test results part, is to demonstrate the effectiveness and robustness of the AggieAir UAS.

2.6.1 Typical Platforms

Several AggieAir UAVs developed or tested by the author are shown in Table 2.11 with detailed specifications. One typical AggieAir1 UAV, “Pheonix” is shown in Fig. 2.24 mounted with the IR sensors and GF-DV. AggieAir2 UAV, “Snow” is specially designed for the thermal camera application with a cover on the top for protection and aerodynamic considerations, shown in Fig. 2.25. Other than airframes made from foam, there is also one airframe, “PinkPanther,” covered by fiber glass. Both the electronics and the autonomous tuning are finished by the author.

2.6.2 Flight Test Results

One example flight result is shown in the following from the 2009 AUVSI student UAS competition. The desired and real-flight path is shown in Fig. 2.26 and the altitude tracking results are shown in Fig. 2.27. It can be seen that the altitude error is roughly around ten

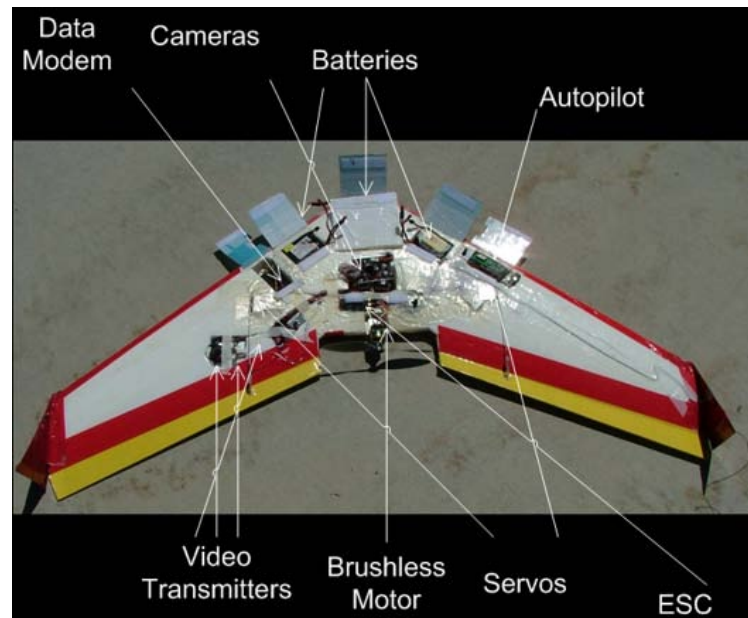


Fig. 2.24: Layout of Pheonix 48" UAV.



Fig. 2.25: Layout of Snow 72" UAV.

meters, which is close to the system limit considering the UAV relies on GPS for the altitude control.

The failure rate during the preparation for the 2009 AUVSI student UAS competition is summarized in Table 2.12. The successful rate for autonomous navigation during fourteen flight tests shows the effectiveness and robustness of the AggieAir UAS platform.

2.7 Chapter Summary

In this chapter, the AggieAir1 and AggieAir2 UAV platforms are explained in detail from both the hardware and software levels. The current autopilot markets are investigated thoroughly based on the remote sensing requirements. The Paparazzi open-source autopilot is adapted to support the COTS IMU through our OSAM-Paparazzi interface. A series of testing protocols are proposed for flight safety considerations. Finally, some flight data are shown to prove the effectiveness of the whole system.

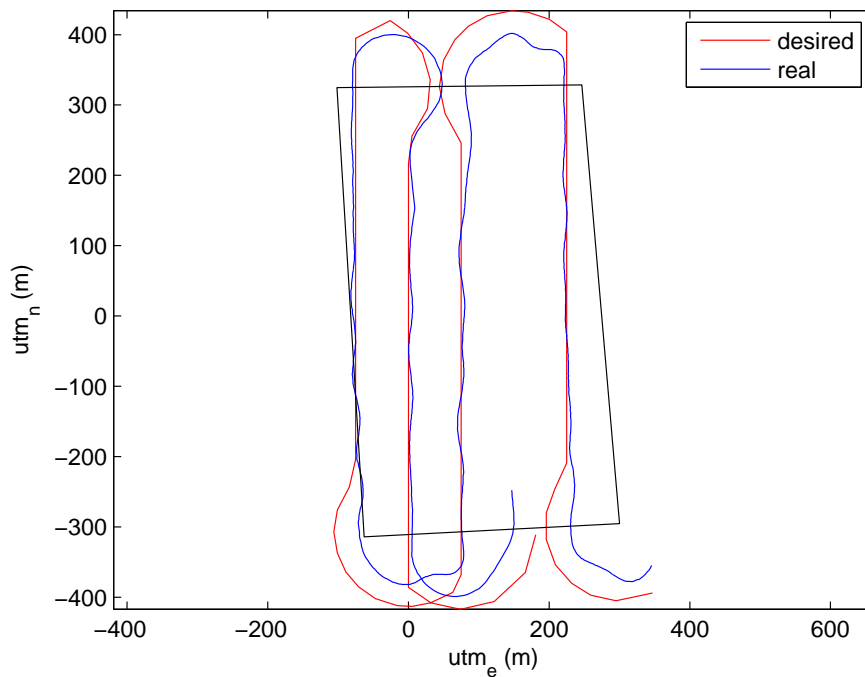


Fig. 2.26: Sample flight trajectories of AggieAir2 UAV (Tiger).

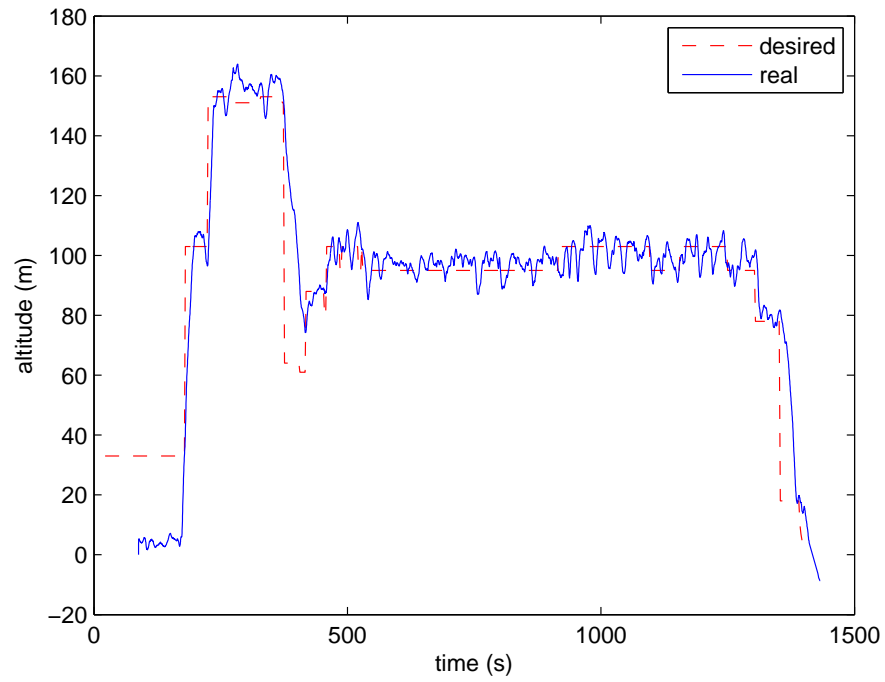


Fig. 2.27: AggieAir altitude tracking results.

Table 2.10: Gumstix resource monitoring for GhostGX2.

No	Time (h:mm)	Used Mem. (k)	Free Mem. (k)	CPU Usage
1	4:29	21472	41452	N/A
2	4:34	22492	40432	N/A
3	4:44	24748	38176	N/A
4	4:50	25984	37940	N/A
5	4:54	26800	36124	N/A
6	4:59	27940	35004	N/A
7	5:04	28972	33952	7.6%
8	5:12	30880	32044	7.6%
9	5:17	31936	30988	7.6%
10	5:27	34552	28372	7.6%
11	5:34	35584	27340	7.6%

Table 2.11: UAVs developed (or partly developed) by the author.

Name	Wing Span	Weight	Sensors	Imagers	RC Ch.	IP
Pheonix	48"	4.4 lbs	IR	3 VC	59	N/A
ChangeE	60"	6.4 lbs	GX2 IMU	N/A	42	252
Falcon	72"	about 7 lbs	Mti-g IMU	2 DC	59	107
Griffin	72"	about 7 lbs	GX2 IMU	2 DC	50	120
Tiger	72"	7.8 lbs	GX2 IMU	2 DC	59	140
PinkPanther	72"	about 8 lbs	GX2 IMU	N/A	59	
Snow	72"	4.4 lbs	GX2 IMU	Thermal	50	133

Table 2.12: Robustness of AggieAir UAS.

Flight Test Summary	
Number of Flight Tests	14
UAV Flight Time	14.3 hours
Autonomous Flight Time	10.9 hours
Success Rate (Auto-takeoff)	99.4% (51 out of 54)
Success Rate (Auto-landing)	98.1% (51 out of 52)
Success Rate (Auto-navigation)	94.2% (49 out of 52)

Chapter 3

State Estimation Filters for Small UAVs

In the past decade, the GPS and inertial sensors become increasingly smaller, lighter, and cheaper, which can be easily fit in small or micro UAVs. The commercial inertial measurement unites (IMUs) can be categorized into three types based on the performance: navigation grade, tactical grade, and industrial grade. The brief specifications are shown in Table 3.1. Recently, many MEMS IMUs become available for as cheap as \$500 or less [49] because of their increasing uses on consumer electronics, like smart phones. However, these cheap industrial grade IMUs have bigger measurement errors or noises compared with expensive navigation grade or tactical grade IMUs. Besides, there are more challenges on how to design, test, and integrate the cheap IMUs to the whole unmanned aircraft system (UAS). More considerations on the system design and the sensor fusion algorithms need to be addressed thoroughly to achieve the autonomous navigation mission.

Many researchers have looked into the state estimation problem using GPS and inertial sensors. The most important states for small UAVs are their attitude or orientations, which can be represented by Euler angles, rotation matrix, or quaternion. One disadvantage of industrial grade IMUs comes from the gyro drift and acceleration measurement inaccuracy. The extended Kalman filter is introduced for IMUs with gyros, accelometers, and magnetometers such as MNAV from Crossbow Technology as part of an open-source

Table 3.1: IMU categories.

IMU Type	Navigation Grade	Tactical Grade	Industrial Grade
Cost(\$)	> 50k	10-20k	0.5-3k
Weight	> 5 lb	about 1 lb	< 5 oz
Gyro Bias	< 0.1 deg./hour	0.1-10 deg./hour	> 10 deg./hour
Example	Honeywell HG9848	Honeywell HG1900	Microstrain GX2

project [3]. However, this method assumes the UAV acceleration to be zero for the measurement equation, which may cause errors in the pitch estimation especially while turning. The measurement of the air speed or the ground speed can be incorporated into the filter for more accurate estimation of the acceleration on each body axis [4]. There are also other approaches to this problem, like the complementary filter [50]. However, all the above approaches are specially designed for a specific hardware platforms. With the current trend of modularization and standardization in the UAV design, the UAV developers can save a large amount of time by buying the cheap commercial-off-the-shelf (COTS) IMUs and configure them into a complete navigation system. The systematic procedure for the state filter design, tuning, and validation needs to be developed to support these cheap COTS IMUs.

This chapter focuses on the implementation of the state estimation filter together with in-flight filter testing and comparison for small UAV applications. The preliminaries of the rigid body rotations are discussed first. Then, two example approaches using extended Kalman filter are introduced. AggieEKF, the extended Kalman filter with compensation from the GPS speed, is proposed and validated in through real flight data.

3.1 Problem Definition and Notations

The state estimation problem is defined in this section in consideration of small UAV constrains. The UAV system states include:

- Position: For example longitude (p_e), latitude (p_n), altitude (h) (LLH);
- Velocity: Defined in the body frame, (u), (v), (w);
- Attitude: The representation can be Euler angles: roll (ϕ), pitch (θ), and yaw (ψ), or any other format such as quaternion or rotation matrix;
- Rate gyro: Angular velocity expressed in the body frame (p , q , r);
- Acceleration: Acceleration expressed in the body frame (a_x , a_y , a_z);
- Air speed (v_a), ground speed (v_g), angle of attack (α), and slide-slip angle (β).

The following states need extra estimation filters since no direct measurements are available or the update rate is not fast enough:

- Position: The position information can greatly affect the georeferencing result. However, civilian GPS receivers can only provide measurements at 4 Hz with the 3D accuracy of more than three meters.
- Attitude: The orientation information is very important for both the flight control and the image georeferencing.
- Wind speed: The wind, especially the wind gust, is a key factor for UAV flight control and the weather prediction.

To make an accurate estimation of the above system states, the UAV motions need to be characterized first. Here, the UAVs are assumed to be rigid bodies moving in Euclidean space. The rigid body rotations are reviewed first and then the UAV kinematics equation is formulated.

3.1.1 Rigid Body Rotations Basics

Rigid body rotations are to model the rotation movements of rigid bodies between the body frame and the inertial reference frame. There are several representations available including Euler angles, rotation matrix, and unit quaternion. Euler angles are the most intuitive way to model the rotations. However, Euler angles have gimbal lock problems at certain extreme orientations [41]. Rotational matrix and unit quaternion do not have the gimbal lock problem with more variables used. The different representations of rotations are introduced together with conversions between each other. Then, the kinematic equation is included with different formats to form a basis for the attitude estimation analysis.

Representation of Rotations

Euler Angles: Euler angles are the most intuitive way to model the rotations, with only three variables, roll (ϕ), pitch (θ), and yaw (ψ). Given the reference frame and the body

frame, Euler angles could be calculated through three basic rotations (each around one axis). The most common notation is the yaw-pitch-roll rotation or so called $z - y - x$ rotation [38]. However, Euler angles have the singularity problem at some extreme points, which is also called gimbal lock problem.

Rotation Matrix: Rotation matrix is the matrix that transforms a vector expressed in the body frame to the corresponding one expressed in the reference frame [51]. It is defined as follows:

$$R = \begin{bmatrix} r_{11} & r_{12} & r_{13} \\ r_{21} & r_{22} & r_{23} \\ r_{31} & r_{32} & r_{33} \end{bmatrix} \quad s.t. \quad RR^T = I, \quad \det(R) = 1, \quad (3.1)$$

where r_{ij} is a scalar.

The space of rotation matrices is also denoted as $SO(3)$ (Special Orthogonal Group), which are also called direction cosine matrices (DCM). It is worth mentioning here that the column vectors of R are actually the unit vectors of the body frame expressed in the inertial reference frame and the row vectors of R are actually the unit vectors of the inertial reference frame expressed in the body frame [52]. For example, the vector $[1, 0, 0]^T$ expressed in the body frame is the same with the vector $[r_{11}, r_{21}, r_{31}]^T$ expressed in the inertial reference frame because $R[1, 0, 0]^T = [r_{11}, r_{21}, r_{31}]^T$.

Unit Quaternion: Unit quaternion is another way of accurate modeling of rotations with only four variables used [51]. It is defined as follows:

$$q = \begin{bmatrix} q_0 \\ q_1 \\ q_2 \\ q_3 \end{bmatrix}, \quad s.t. \quad |q|^2 = q_0^2 + q_1^2 + q_2^2 + q_3^2 = 1. \quad (3.2)$$

The unit quaternion is usually denoted as (q_0, \vec{q}) with $\vec{q} = [q_1, q_2, q_3]^T$.

Conversion Between Representations

These three representations can all be used to model the rotation of the UAV. For the autonomous navigation mission, Euler angles are needed for control purposes. However, the rotation matrix or quaternion format is more widely used in the attitude estimation problem due to their completeness and constraints. For instance, the rotation matrix must maintain its orthogonality among vectors. Thus, the conversion between any two of them is also needed for the estimation and control problems of small UAVs.

Euler Angles to Rotation Matrix: This conversion is needed to make a vector mapping from the body frame to the reference inertial frame.

$$R = \begin{bmatrix} \cos \theta \cos \psi & -\cos \phi \sin \psi + \sin \phi \sin \theta \cos \psi & \sin \phi \sin \psi + \cos \phi \sin \theta \cos \psi \\ \cos \theta \sin \psi & \cos \phi \cos \psi + \sin \phi \sin \theta \sin \psi & -\sin \phi \cos \psi + \cos \phi \sin \theta \sin \psi \\ -\sin \theta & \sin \phi \cos \theta & \cos \phi \cos \theta \end{bmatrix} \quad (3.3)$$

Rotation Matrix to Euler Angles: This conversion is needed if the rotation matrix is used in the estimation problem while Euler angles are needed for controls.

$$\phi = \tan^{-1}\left(\frac{r_{32}}{r_{33}}\right), \quad (3.4)$$

$$\theta = -\sin^{-1}(r_{31}), \quad (3.5)$$

$$\psi = \tan^{-1}\left(\frac{r_{21}}{r_{11}}\right). \quad (3.6)$$

Quaternion to Euler Angles: This conversion is needed if the rotation matrix is chosen in the estimation problem and Euler angles for controls.

$$\phi = \tan^{-1} \frac{2(q_2q_3 + q_0q_1)}{q_0^2 - q_1^2 - q_2^2 + q_3^2}, \quad (3.7)$$

$$\theta = \sin^{-1}(-2(q_1q_3 - q_0q_2)), \quad (3.8)$$

$$\psi = \tan^{-1} \frac{2(q_1q_2 + q_3q_0)}{q_0^2 + q_1^2 - q_2^2 - q_3^2}. \quad (3.9)$$

3.1.2 UAV Kinematics

Kinematics is to describe the motion of the UAV without considering the forces and torques that cause it [41]. UAV kinematics can be used for estimation of the UAV orientation. The six degrees of freedom UAV dynamics can be modeled by a series of nonlinear equations.

$$\dot{X} = f(X, U), \quad (3.10)$$

$$X = [p_n \ p_e \ h \ u \ v \ w \ \phi \ \theta \ \psi \ p \ q \ r]^T, \quad (3.11)$$

$$U = [\delta_a \ \delta_e \ \delta_r \ \delta_t]^T, \quad (3.12)$$

where δ_a is the aileron, δ_e is the elevator, δ_r is the rudder, and δ_t is the throttle. Not all these equations are needed for the estimation of the attitude. Only the angle kinematic equation is provided for later estimation uses.

Angle Kinematic Equation

The angle kinematic equation deals with the derivatives of the orientations. They can be expressed in Euler angles, unit quaternion, or rotation matrix.

Euler Angles Representation [41]:

$$\dot{\phi} = p + q \sin \phi \tan \theta + r \cos \phi \tan \theta, \quad (3.13)$$

$$\dot{\theta} = q \cos \phi - r \sin \theta, \quad (3.14)$$

$$\dot{\psi} = \frac{q \sin \phi + r \cos \phi}{\cos \theta}, \quad (3.15)$$

where p, q, r are the angular rates expressed in the body frame.

Quaternion Representation [41]:

$$\dot{q} = \frac{1}{2} \begin{bmatrix} 0 & -p & -q & -r \\ p & 0 & r & -q \\ q & -r & 0 & p \\ r & q & -p & 0 \end{bmatrix} q. \quad (3.16)$$

The above equations can be used for the estimation of the UAV orientation given the angular rate measurements. However, there must be some compensations because the real MEMS gyro sensors have big drift errors and random noises.

3.2 Extended Kalman Filter for Attitude Estimation

Extended Kalman filters are frequently used in nonlinear estimation problems, especially the attitude estimation problem of rigid bodies like a spacecraft or an aircraft. The extended Kalman filter can recursively estimate the system states from system measurements corrupted with Gaussian noises. It has advantages here since both gyro and accelerometer sensors has drifts and Gaussian like noises. The general extended Kalman filter and two representing approaches for the attitude estimation problem are introduced in the following sections.

3.2.1 General Extended Kalman Filter

Assume that a general nonlinear discrete-time system can be modeled as follows:

$$x_k = f(x_{k-1}, u_k) + w_k, \quad s.t. \quad w \sim N(0, Q), \quad (3.17)$$

$$y_k = g(x_k) + v_k, \quad s.t. \quad v \sim N(0, Q), \quad (3.18)$$

where x_k is a $m \times 1$ vector, y_k is a $n \times 1$ vector, $f(x_{k-1}, u_k)$ and $g(x_k)$ are nonlinear functions. The first equation is called propagation equation and the second one is called the measurement equation.

Given the initial values P_0 , the measurement covariance R and the state covariance Q . The optimal Kalman estimate of the states can be updated using the following steps [53]:

- (1) State estimation extrapolation: $\hat{x}_{k|k-1} = f(x_{k-1|k-1}, u_k)$,
- (2) Error covariance extrapolation: $P_{k|k-1} = F_k P_{k-1|k-1} F_k^T + Q_k$,
- (3) Kalman gain: $K_k = P_{k|k-1} G_k^T (G_k P_{k|k-1} G_k^T + R_k)^{-1}$,
- (4) State estimate update: $\hat{x}_{k|k} = x_{k|k-1} + K_k (y_k - g(x_{k|k-1}))$,
- (5) Error covariance update: $P_{k|k} = (I - K_k G_k) P_{k|k-1}$.

The F_k is the Jacobian matrix of $f(x_{k-1}, u_k)$, and the G_k is the Jacobian matrix of $g(x_k)$.

3.2.2 Quaternion-Based Extended Kalman Filter

Unit quaternion has many applications in the state estimation problems because its simplicity. A quaternion-based extended Kalman filter is proposed originally for the MNAV IMU from Crossbow Technology [3]. The system state variables include both the unit quaternion q and the gyro biases. The measurements or observation of the system is the acceleration: a_x, a_y, a_z , and the yaw angle ψ derived from the magnetometer. The propagation equation and the measurement equation are listed below [3].

$$\dot{q} = \frac{1}{2} \begin{bmatrix} 0 & -\hat{p} & -\hat{q} & -\hat{r} & 0 & 0 & 0 \\ \hat{p} & 0 & \hat{r} & -\hat{q} & 0 & 0 & 0 \\ \hat{q} & -\hat{r} & 0 & \hat{p} & 0 & 0 & 0 \\ \hat{r} & \hat{q} & -\hat{p} & 0 & 0 & 0 & 0 \\ \hline 0 & 0 & 0 & 0 & 0 & 0 & 0 \\ 0 & 0 & 0 & 0 & 0 & 0 & 0 \\ 0 & 0 & 0 & 0 & 0 & 0 & 0 \end{bmatrix} q + w_k, \quad q = \begin{bmatrix} q_0 \\ q_1 \\ q_2 \\ q_3 \\ \hline b_p \\ b_q \\ b_r \end{bmatrix}, \quad (3.19)$$

$$\begin{bmatrix} \hat{p} \\ \hat{q} \\ \hat{r} \end{bmatrix} = \begin{bmatrix} p \\ q \\ r \end{bmatrix} - \begin{bmatrix} b_p \\ b_q \\ b_r \end{bmatrix}, \quad (3.20)$$

$$\begin{bmatrix} a_x \\ a_y \\ a_z \\ \psi \end{bmatrix} = \begin{bmatrix} 2g(q_1q_3 - q_0q_2) \\ 2g(q_2q_3 + q_0q_1) \\ g(q_0^2 - q_1^2 - q_2^2 + q_3^2) \\ \tan^{-1} \frac{2(q_1q_2 + q_3q_0)}{q_0^2 + q_1^2 - q_2^2 - q_3^2} \end{bmatrix} + v_k \quad v_k = N(0, R). \quad (3.21)$$

It is worth pointing out that the measurement equation has an assumption that the acceleration measured is only the projection of the gravity vector. However, this assumption may not be true for small UAVs.

3.2.3 Euler Angles-Based Extended Kalman Filter

Euler angles can also be chosen as the system states for the attitude estimation problem. Assume that the system state is a vector x , representing the roll and pitch angle, and the system output is a vector \hat{y} , representing the accelerometer readings, the system can then be modeled [33]:

$$x = \begin{bmatrix} \phi \\ \theta \end{bmatrix}, \quad \hat{y} = \begin{bmatrix} a_x \\ a_y \\ a_z \end{bmatrix}, \quad (3.22)$$

$$\dot{x} = \begin{bmatrix} p + q \sin \phi \tan \theta + r \cos \phi \tan \theta \\ q \cos \phi - r \sin \phi \end{bmatrix} + v_w, \quad v_w \sim N(0, Q), \quad (3.23)$$

$$\hat{y} = \begin{bmatrix} \dot{u} - rv + qw + g \sin \theta \\ \dot{v} + ru - pw - g \cos \theta \sin \phi \\ \dot{w} - qu + pv - g \cos \theta \cos \phi \end{bmatrix} + v_k, \quad v_k \sim N(0, R). \quad (3.24)$$

In fact, the velocities (u, v, w) are not easily measurable at a high frequency. The air speed can be used instead to simplify the measurement equation for small UAVs. The

following assumptions can be made [33]:

- $\dot{u} = \dot{v} = \dot{w} = 0$. The small UAV will not accelerate all the time;
- $v = 0$. The small UAV will not go sideways;
- $u = v_a \cos \theta$, $w = v_a \sin \theta$;

where V_a is the air speed measured by the pitot tube. The measurement equation can then be simplified.

$$\hat{y} = \begin{bmatrix} qV_a \sin \theta + g \sin \theta \\ rV_a \cos \theta - pV_a \sin \theta - g \cos \theta \sin \phi \\ -qV_a \cos \theta - g \cos \theta \cos \phi \end{bmatrix} + v_k, \quad v_k \sim N(0, R). \quad (3.25)$$

The attitude can then be estimated using the extended Kalman filter following the steps described in the above section.

3.3 AggieEKF: GPS-Aided Extended Kalman Filter

AggieEKF, a GPS-aided extended Kalman filter is proposed in this section with considerations from both filters designed in the above sections. Unit quaternion is chosen for our approach because of its simplicity and constraints from its unit scalar. An extended Kalman filter similar to the one developed by Jung [3] is developed. However, the measurement equation is replaced by a more accurate estimation of the gravity vector with the help from the GPS speed measurements. The system equations are shown as below where V_g is the ground speed measured by the GPS. The attitude state estimation can be calculated using the steps described in the above section.

$$\dot{q} = \frac{1}{2} \begin{bmatrix} 0 & -\hat{p} & -\hat{q} & -\hat{r} & 0 & 0 & 0 \\ \hat{p} & 0 & \hat{r} & -\hat{q} & 0 & 0 & 0 \\ \hat{q} & -\hat{r} & 0 & \hat{p} & 0 & 0 & 0 \\ \hat{r} & \hat{q} & -\hat{p} & 0 & 0 & 0 & 0 \\ \hline 0 & 0 & 0 & 0 & 0 & 0 & 0 \\ 0 & 0 & 0 & 0 & 0 & 0 & 0 \\ 0 & 0 & 0 & 0 & 0 & 0 & 0 \end{bmatrix} q + w_k, \quad (3.26)$$

$$\begin{bmatrix} \hat{a}_x \\ \hat{a}_y \\ \hat{a}_z \end{bmatrix} = \begin{bmatrix} 2g(q_1q_3 - q_0q_2) \\ 2g(q_2q_3 + q_0q_1) \\ g(q_0^2 - q_1^2 - q_2^2 + q_3^2) \end{bmatrix} + v_k \quad v_k = N(0, R), \quad (3.27)$$

$$\text{where } \begin{bmatrix} \hat{a}_x \\ \hat{a}_y \\ \hat{a}_z \end{bmatrix} = \begin{bmatrix} a_x \\ a_y - rV_g + g \sin \phi_{t-1} \\ a_z + qV_g + g \cos \phi_{t-1} \end{bmatrix}. \quad (3.28)$$

3.4 Experimental Results

To validate the proposed AggieEKF algorithm, a AggieAir2 UAV is modified to fit in different types of CTOS IMUs for sensor data collection. Two flight tests were performed at the Cache Junction research farm on Nov. 16th and 23rd for the comparison of three IMUs including Microstrain GX2, AggieNav, and Crossbow MNAV. The central bay layout of the three IMUs is shown in Fig 3.1.

The AggieAir2 UAV uses Microstrain GX2 IMU and the Paparazzi TWOG autopilot as the onboard navigation control system. The UAV is commanded to follow the line 1-2 task by circling back with the turning radius of 70 meters if passing waypoint 1 or 2. The UAV trajectory is plotted in Fig. 3.2. All the inertial sensor data is saved on the Gumstix while flying at 50 Hz together with the timer on Gumstix. The GPS sensor data is also logged at 4 Hz. The AggieEKF is then implemented in the MATLAB for validations. The roll and pitch angle estimations from the AggieEKF algorithm are plotted together with the

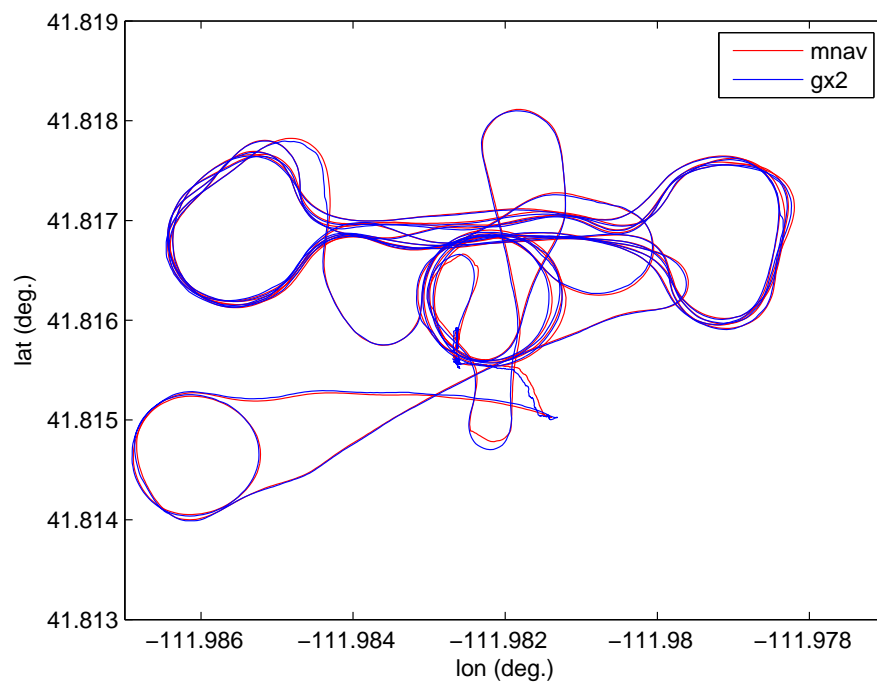


Fig. 3.1: Central bay layout of three IMUs.

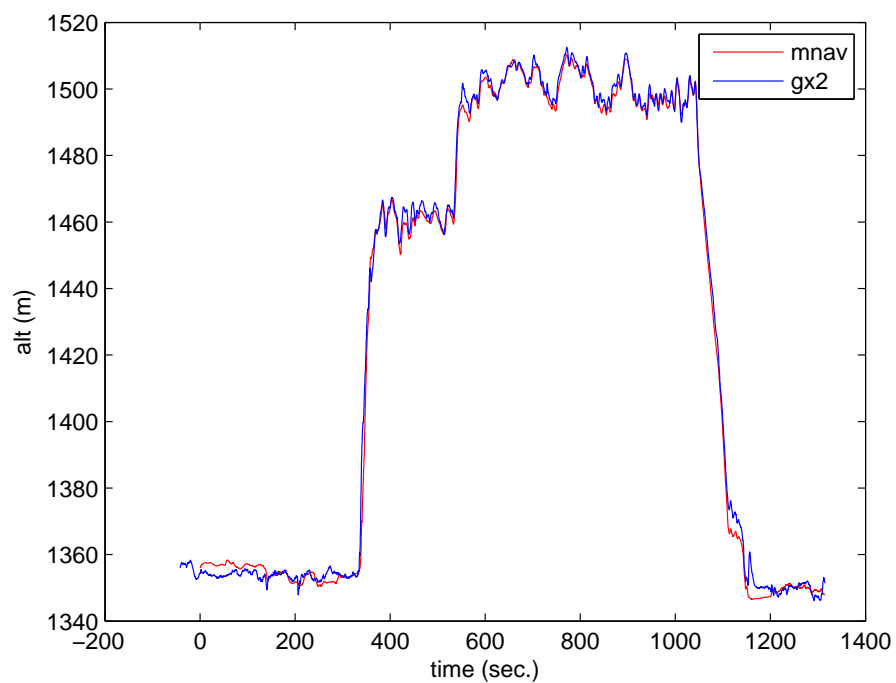
orientation outputs from the Microstrain GX2 IMU for reference in Fig. 3.3 and Fig. 3.4. It can be observed that the roll estimation is good and the pitch estimation is a little bit noisy. As a comparison, the roll and pitch estimation based on the EKF algorithm developed by Jung [3] is also provided in Fig. 3.5 and Fig. 3.6.

3.5 Chapter Summary

In this chapter, the attitude estimation problem is focused. Several estimation algorithms are compared including the complementary filter approach and the extended Kalman filter solution. A new attitude estimation algorithm AggieEKF is then introduced with the compensation to the accelerometer measurements. The simulation results show the feasibility of the proposed algorithm.



(a) Latitude and Longitude plot.



(b) Altitude plot.

Fig. 3.2: UAV trajectory for sensor data collection.

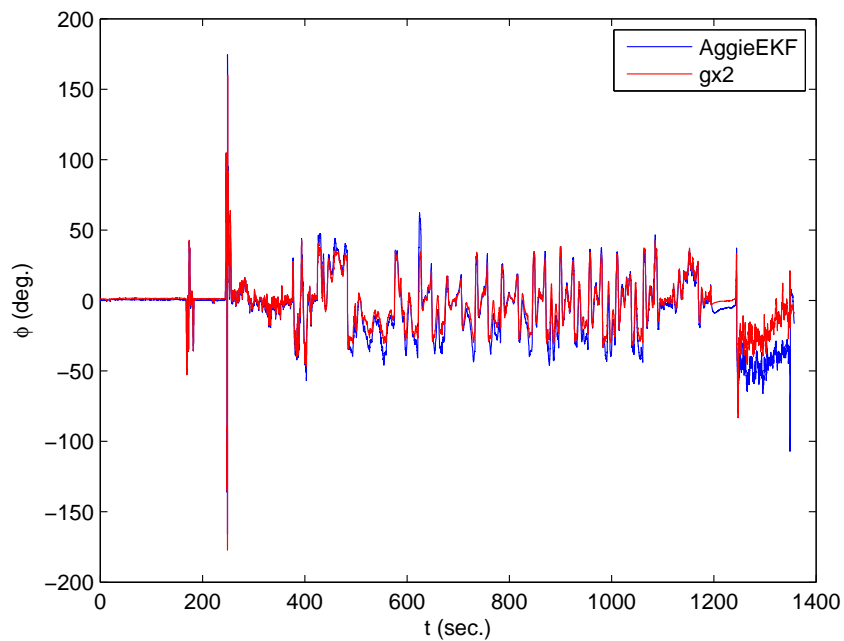


Fig. 3.3: Roll angle estimation (AggieEKF).

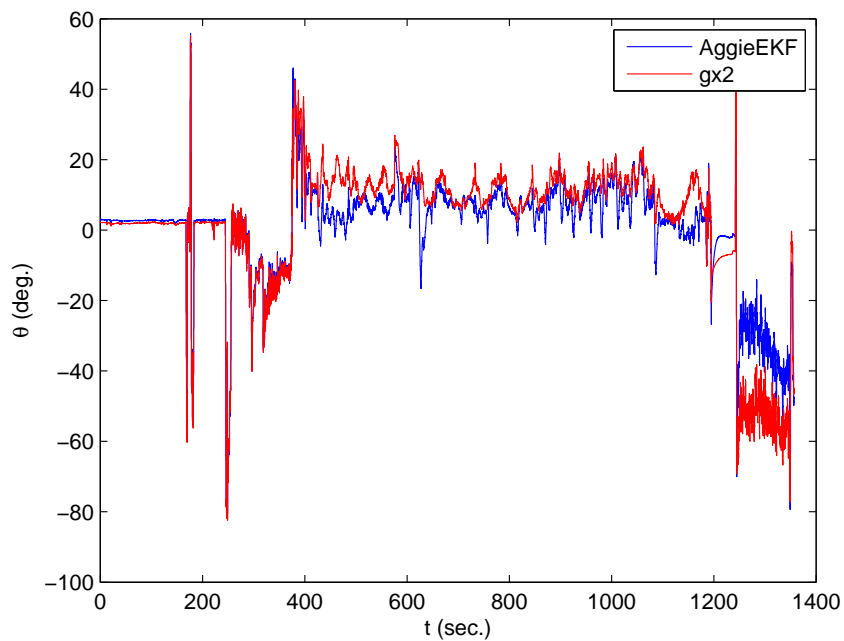


Fig. 3.4: Pitch angle estimation (AggieEKF).

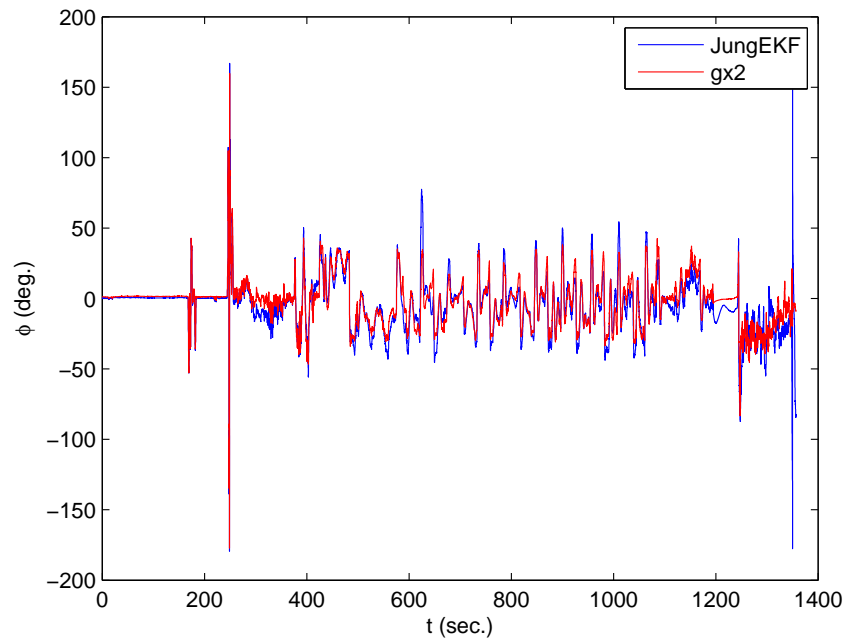


Fig. 3.5: Roll angle estimation (JungEKF).

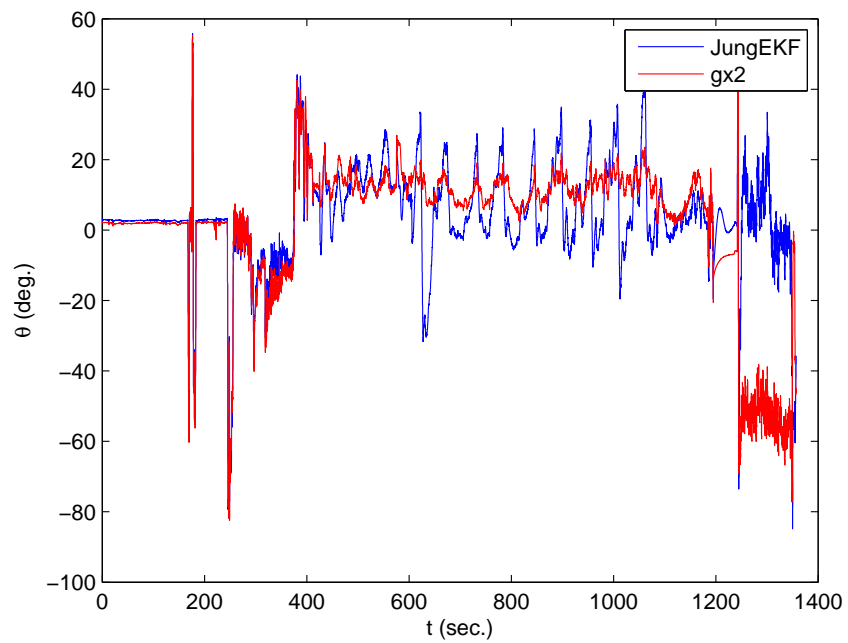


Fig. 3.6: Pitch angle estimation (JungEKF).

Chapter 4

Advanced Lateral Flight Controller Design

4.1 Introduction

The lateral flight controller is to control the movement around the roll axis, which is critical to the flight stability. This chapter introduces a fractional order controller design for the roll-channel of a small fixed-wing UAV for better flight performance. Many researchers have looked into the problem of UAV modeling and control. Open-loop steady state flight experiments are proposed for the aileron-(roll rate) and elevator-(pitch rate) loop system identification [6]. But the open-loop system identification has to have special requirements on UAV flight stability, which limits the roll and pitch reference signals to be as small as 0.02 rad. UAV model identification (ID) experiments can also be performed with human operators controlling the UAVs remotely. Different types of auto-regressive with exogenous input (ARX) models are identified while the UAV is flying in loiter mode [7]. Human operators could generate open-loop responses but it may be impossible for some specially designed reference like pseudo random binary sequences (PRBS). Other researchers also tried closed-loop system identification method on separate channels of unmanned helicopters [8–10].

There are trade-offs, like safety and maneuverability, while designing UAV system identification experiments. The system ID experiments are not easy to repeat since the UAV system could easily stall, given a too aggressive control input. On the other hand, very small excitations may not be adequate to excite the system dynamics. A closed-loop system identification method is used in this chapter with considerations for flight stability and test difficulty. The UAV is first roughly tuned with a set of initial proportional integral derivative (PID) parameters sufficient to guarantee stability while flying horizontally. Then the UAV initial closed-loop model is identified and the controllers are designed based on

the identified models, which will be discussed in detail in this chapter.

Fractional order control (FOC) has attracted a lot of interest recently. FOC introduces new fractional derivative and fractional integral operators to the classical PID control. It provides additional design freedom for the controller tuning [54]. FOC has advantages in application scenarios such as servo control [55], water tank control, quad rotor [56], and other industrial applications [57]. The fractional order proportional integral (PI^λ) controller is one of the simplest fractional order controllers similar to the classical proportional integral (PI) controller. FOC can have advantages over traditional controllers because FOC introduces fractional order operators [58]. To simplify the flight control problem, the aileron-roll loop is singled out for controller comparisons between the fractional order PI (FOPI) controller and the integer order PID controller. The proposed controllers are tested in conditions like strong wind gusts and payload variations in simulation and real-flight tests.

4.2 Preliminaries of UAV Flight Control

UAV dynamics can be modeled using system states including:

- (1) Position: e.g., longitude (p_e), latitude (p_n), height (h) (LLH);
- (2) Velocity: three axis (u), (v), (w);
- (3) Attitude: roll (ϕ), pitch (θ), and yaw (ψ);
- (4) Gyro rate: gyro acceleration p , q , r ;
- (5) Acceleration: acceleration a_x , a_y , a_z ;
- (6) Air speed (v_a), ground speed (v_g), angle of attack (α) and slide-slip angle (β).

UAV control inputs generally include: aileron (δ_a), elevator (δ_e), rudder (δ_r), and throttle (δ_t). There are also elevons which combine the functions of the aileron and the elevator. Elevons are frequently used on flying wing airplanes. Different types of UAVs

may have different control surface combinations. For example, some delta wing UAVs can just have elevator, aileron, and throttle with no rudder control.

The six degrees of freedom UAV dynamics can be modeled by a series of nonlinear equations.

$$\dot{x} = f(x, u), \quad (4.1)$$

$$x = [p_n \ p_e \ h \ u \ v \ w \ \phi \ \theta \ \psi \ p \ q \ r]^T, \quad (4.2)$$

$$u = [\delta_a \ \delta_e \ \delta_r \ \delta_t]^T. \quad (4.3)$$

The ultimate objective of UAV flight control is to let the UAV follow a preplanned 3D trajectory with pre-specified orientations. Due to the limits from the hardware, most current UAV autopilots can only achieve the autonomous waypoints navigation objective. There are basically two types of controller design approaches: the precise-model-based nonlinear controller design and the in-flight-tuning-based PID controller design. The first method requires a precise and complete dynamic model, which is usually very expensive to obtain. On the other hand, it is estimated that more than 90% of the current working controllers are PID controllers [59]. Most commercial UAV autopilots use cascaded PID controllers for autonomous flight control [2].

The cascaded PID controller can be used for UAV flight control because the nonlinear dynamic model can be linearized around certain trimming points and be treated as a simple single-input and single-output (SISO) or multiple-input and multiple-output (MIMO) linear system. The UAV dynamics can be decoupled into two modes for the low level control:

- (1) Longitudinal mode: pitch loop;
- (2) Lateral mode: roll loop.

After dividing the 3D rigid body motion control problem into several loops, cascaded controllers can be designed to accomplish the UAV flight control task. The roll loop control problem or lateral dynamics is carefully studied in this chapter. The roll loop of a UAV can be treated as a SISO (roll-aileron) system around the equilibrium point. In other words, it

can be treated as a SISO system around the point where it can achieve a steady state flight. Steady state flight means all the force and moment components in the body coordinate frame are constant or zero [41]. An intuitive controller design is to use the classical PID controller structure as follows:

$$C(s) = K_p(1 + \frac{K_i}{s} + K_d s). \quad (4.4)$$

All the controller parameters (K_p , K_i , K_d) will be determined by either off-line or on-line controller tuning experiments.

4.3 Roll-Channel System Identification and Control

The most intuitive method for roll-channel system identification is to go through an open-loop analysis. However, this method can only be employed with several constraints including small reference (as little as 0.02 rad. for the roll set point [6]) and difficulties in keeping the UAV stable under the open-loop configuration. Therefore, the closed-loop system identification method is used in this chapter because it can guarantee the flight stability of the UAV. The only prior condition is that a rough PID parameter tuning must be performed before the system identification experiment.

The whole system identification procedure includes UAV trim tuning, rough PID tuning to determine $C_0(s)$ and UAV system identification experiments with pre-specified excitations, as shown in Fig. 4.1.

Once the system model is derived, another outer-loop controller $C(s)$ will be designed based on modified Ziegler-Nichols tuning algorithm or fractional order PI^λ design method, shown in Fig. 4.2.

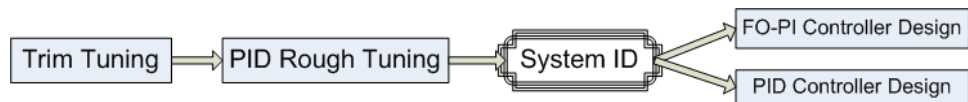


Fig. 4.1: FOPI flight controller design procedure.

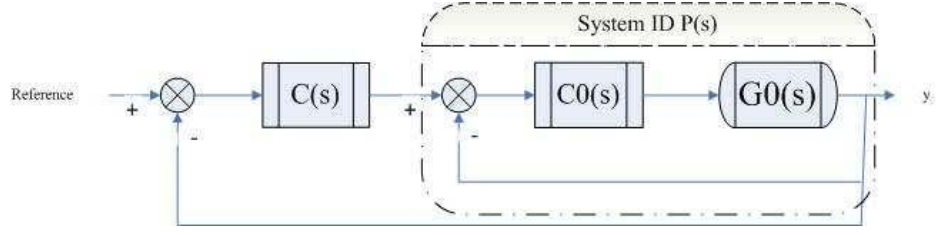


Fig. 4.2: System identification procedure.

4.3.1 System Model

For the system model, a simple ARX model is used since the first order ARX model can provide some simplicity for the further fractional order controller design. The ARX model is defined as

$$\frac{Y(z)}{R(z)} = \frac{a_0 + a_1 z^{-1} + \dots + a_m z^{-m}}{b_0 + b_1 z^{-1} + \dots + b_n z^{-n}}, \quad (4.5)$$

where $Y(z)$ is the system output, (e.g., the roll angle), and $R(z)$ is the reference signal, (e.g., the reference roll angle).

To make a comparison, the first order plus time delay (FOPTD) model is also simplified via frequency-domain fitting [60] from the high order ARX model for applying the modified Ziegler Nichols PID tuning rule,

$$P(s) = \frac{Y(s)}{R(s)} = \frac{K e^{-Ls}}{Ts + 1}. \quad (4.6)$$

4.3.2 Excitation Signal for System Identification

The excitations for the system ID could be step response, square wave response or pseudo random binary sequence (PRBS) or other pre-specified references. The excitation of the system needs also to be carefully chosen because the frequency range of the input reference signal may have a huge impact on the final system identification results. Two reference signals are chosen: square-wave reference and PRBS. PRBS is chosen in this chapter for simulation study because its signal is rich in all the interested frequency.

4.3.3 Parameter Optimization

Least squares error method is used for fitting the model to the real data. Assume the ARX model is given by (4.5). Then

$$\begin{aligned} \hat{y}(k) = & \frac{1}{b_0}(a_0r(k) + \cdots + a_mr(k-m) \\ & - b_1y(k-1) - \cdots - b_ny(k-n)) + e(k), \end{aligned} \quad (4.7)$$

where $e(k)$ is the white noise caused by sensor measurements.

The evaluation function defined below is used to minimize the least squares of the errors

$$V = \sum_{k=1}^N e^T(k)e(k), \quad (4.8)$$

where N is the total data length. The classical least squares method can be used here to get the optimal ARX model parameter. In MATLAB, the related function is called `arx` [61]. FOPTD model is simplified from the higher order ARX model using the `getfoptd` function [60].

4.4 Fractional Order Controller Design

Based on the identified simple model, a new fractional order PI controller is then designed with pre-specified performance requirements.

4.4.1 Fractional Order Operators

There are several definitions for fractional order operators including Riemann-Liouville (RL) definition, Caputo definition, and Grünwald-Letnikov definition. Riemann-Liouville definition is one of the most used definitions. The RL fractional integral of function $f(t)$ is defined as [62]

$${}_0D_t^{-\lambda}f(t) \triangleq \frac{1}{\Gamma(\lambda)} \int_0^t (t-\tau)^{\lambda-1} f(\tau) d\tau, \quad (4.9)$$

where $0 < \lambda < 1$, $\Gamma(\cdot)$ is the Gamma function defined as

$$\Gamma(z) = \int_0^{\infty} e^{-t} t^{z-1} dt, \text{Re}(z) > 0. \quad (4.10)$$

The Laplace transform of the RL fractional integral under zero initial conditions can be derived as

$$\mathcal{L}[{}_0D_t^{-\lambda} f(t)] = \frac{1}{s^\lambda} F(s), \quad (4.11)$$

where $F(s)$ is the Laplace transform of $f(t)$.

The Caputo fractional integral of order $0 < \lambda < 1$ is defined as [62]

$${}_0D_t^{-\lambda} f(t) = \frac{1}{\Gamma(\lambda)} \int_0^t \frac{y(\tau)}{(t-\tau)^{1-\lambda}} d\tau. \quad (4.12)$$

The RL definition and Caputo definition are almost the same except for some initial value settings.

4.4.2 PI^λ Controller Design

With the introduction of fractional derivatives and integrals, the most commonly used PID controller can be extended to $PI^\lambda D^\mu$ controllers with more tuning knobs. PI^λ controller is studied in this chapter since it has the same amount of tuning parameters as the integer order PID controllers to allow a fair comparison. The fractional order proportional integral controller to be designed has the following form of transfer function,

$$C(s) = K_p \left(1 + \frac{K_i}{s^\lambda}\right), \quad (4.13)$$

where $\lambda \in (0, 2)$.

Controller Design Specifications

Assume that the open-loop transfer function for the system is given by $G(s)$, the gain crossover frequency is given by ω_c , and phase margin is specified by ϕ_m . To ensure the

system stability and robustness, three specifications are proposed as follows [63],

(i) phase margin specification,

$$\text{Arg}[G(j\omega_c)] = \text{Arg}[C(j\omega_c)P(j\omega_c)] = -\pi + \phi_m;$$

(ii) gain crossover frequency specification,

$$|G(j\omega_c)|_{dB} = |C(j\omega_c)P(j\omega_c)|_{dB} = 0;$$

(iii) robustness to gain variation of the plant demands that the phase derivative with respect to the frequency is zero, which is to say that the phase Bode plot is flat around the gain crossover frequency. It means the system is more robust to gain changes and the overshoots of the response are almost unchanged,

$$\frac{d(\text{Arg}(G(j\omega)))}{d\omega}\bigg|_{\omega=\omega_c} = 0.$$

FOPI Controller Design for the First Order Systems

To simplify the presentation, the simple form of $G(s)$ is studied in the later part without loss of generality since any complex system can be simplified to a simple model. The typical first order control plant discussed in this chapter has the following form of transfer function,

$$P(s) = \frac{K}{Ts + 1}. \quad (4.14)$$

Note that, the plant gain K in (4.14) can be normalized to 1 without loss of generality since the proportional factor in the transfer function (4.14) can be incorporated in the proportional coefficient of the controller.

According to the form of the typical first order systems considered and the FOPI controller discussed, the FOPI controller can be systematically designed following the three specifications introduced above. The FOPI controller parameters can be obtained using the following steps.

The open-loop transfer function $G(s)$ of the fractional order PI controller for the fractional order system is that,

$$G(s) = C(s)P(s).$$

(1) According to the fractional order PI controller transfer function form (4.13), its frequency response could be plotted as follows:

$$C(j\omega) = K_p(1 + K_i\omega^{-\lambda} \cos(\lambda\frac{\pi}{2}) - jK_i\omega^{-\lambda} \sin(\lambda\frac{\pi}{2})).$$

The phase and gain are as follows:

$$\begin{aligned} \text{Arg}[C(j\omega)] &= -\tan^{-1} \frac{K_i\omega^{-\lambda} \sin(\lambda\pi/2)}{1 + K_i\omega^{-\lambda} \cos(\lambda\pi/2)}, \\ |C(j\omega)| &= K_p J(\omega), \end{aligned}$$

where

$$J(\omega) = [(1 + K_i\omega^{-\lambda} \cos(\lambda\pi/2))^2 + (K_i\omega^{-\lambda} \sin(\lambda\pi/2))^2]^{\frac{1}{2}}.$$

(2) According to the first order system transfer function (4.14), its frequency response could be plotted as below:

$$P(j\omega) = \frac{1}{T(j\omega) + 1}.$$

The phase and gain of the plant are as follows:

$$\begin{aligned} \text{Arg}[P(j\omega)] &= -\tan^{-1}(\omega T), \\ |P(j\omega)| &= \frac{1}{\sqrt{1 + (\omega T)^2}}. \end{aligned}$$

(3) The open-loop frequency response $G(j\omega)$ is that,

$$G(j\omega) = C(j\omega)P(j\omega).$$

The phase and gain of the open-loop frequency response are as follows:

$$\begin{aligned}\text{Arg}[G(j\omega)] &= -\tan^{-1} \frac{K_i \omega^{-\lambda} \sin(\lambda\pi/2)}{1 + K_i \omega^{-\lambda} \cos(\lambda\pi/2)} - \tan^{-1}(\omega T), \\ |G(j\omega)| &= \frac{K_p J(\omega)}{\sqrt{1 + (\omega T)^2}}.\end{aligned}$$

(4) According to Specification (i), the phase of $G(j\omega)$ can be expressed as,

$$\text{Arg}[G(j\omega_c)] = -\pi + \phi_m. \quad (4.15)$$

From (4.15), the relationship between K_i and λ can be established as follows:

$$K_i = \frac{-\tan(\tan^{-1}(\omega_c T) + \phi_m)}{\omega_c^{-\lambda} \sin(\lambda\pi/2) + M}, \quad (4.16)$$

where $M = \omega_c^{-\lambda} \cos(\lambda\pi/2) \tan(\tan^{-1}(\omega_c T) + \phi_m)$.

(5) According to Specification (iii) about the robustness to gain variations of the plant,

$$\frac{d(\text{Arg}(G(j\omega)))}{d\omega} \Big|_{\omega=\omega_c} = \frac{K_i \lambda \omega_c^{\lambda-1} \sin(\lambda\pi/2)}{\omega_c^{2\lambda} + 2K_i \omega_c^{\lambda} \cos(\lambda\pi/2) + K_i^2} - \frac{T}{1 + (T\omega_c)^2} = 0. \quad (4.17)$$

From (4.17), the relationship between K_i and λ is:

$$\begin{aligned}E \omega_c^{-2\lambda} K_i^2 + E + [2E \omega_c^{-\lambda} \cos(\lambda\pi/2) - \lambda \omega_c^{-\lambda-1} \sin(\lambda\pi/2)] K_i &= 0, \\ E \omega_c^{-2\lambda} K_i^2 + F K_i + E &= 0,\end{aligned}$$

where $F = 2E \omega_c^{-\lambda} \cos(\lambda\pi/2) - \lambda \omega_c^{-\lambda-1} \sin(\lambda\pi/2)$, then,

$$K_i = \frac{-F \pm \sqrt{F^2 - 4E^2 \omega_c^{-2\lambda}}}{2E \omega_c^{-2\lambda}}, \quad (4.18)$$

where $E = \frac{T}{1 + (T\omega_c)^2}$.

(6) From Specification (ii), an equation about K_p is:

$$|G_2(j\omega_c)| = |C_2(j\omega_c)P(j\omega_c)| = \frac{K_p J(\omega_c)}{\sqrt{1 + (\omega_c T)^2}} = 1. \quad (4.19)$$

The above equations (4.17), (4.18), and (4.19) can be solved to get λ , K_i , and K_p . However, the solution may not exist for the integer order PID controller. In other words, fractional order controllers provide a larger solution candidate set compared with integer order ones. A graphical plotting method is used in this chapter to obtain the solutions.

FOPI Controller Design for FOPTD Systems

Similarly, the FOPI controller could be designed for the FOPTD systems. The FOPTD system could be modeled by the following:

$$P(s) = \frac{1}{Ts + 1} e^{-Ls}. \quad (4.20)$$

Following the similar derivation described above, the parameters for the FOPI controller could be calculated from the following equations:

$$K_i = \frac{-\tan[\arctan(\omega_c T) + \phi_m + L\omega_c]}{W}, \quad (4.21)$$

$$A\omega_c^{-2\lambda} K_i^2 + BK_i + A = 0, \quad (4.22)$$

$$K_p = \frac{\sqrt{1 + (\omega_c T)^2}}{J(\omega_c)}, \quad (4.23)$$

where

$$W = \omega_c^{-\lambda} \cos(\lambda\pi/2) \tan[\arctan(\omega_c T) + \phi_m + L\omega_c] + \omega_c^{-\lambda} \sin(\lambda\pi/2),$$

$$A = \frac{T}{1 + (\omega_c T)^2} + L,$$

$$B = 2A\omega_c^{-\lambda} \cos(\lambda\frac{\pi}{2}) - \lambda\omega_c^{-\lambda-1} \sin(\lambda\frac{\pi}{2}).$$

4.4.3 Fractional Order Controller Implementation

To implement a PI^λ fractional order controller, an approximation must be used since the fractional order operator has infinite dimensions. The Oustaloup approximation method is to use a band-pass filter to approximate the fractional order controller based on frequency domain response. There are also other methods that directly approximate the FO controller responses [64].

Oustaloup Approximation

The Oustaloup Recursive Approximation Algorithm [65] is used in this chapter for simulation part due to its easiness to adapt to MATLAB Simulink environment. Assuming the frequency range is chosen as (ω_b, ω_h) , the Oustaloup approximate transfer function for s^γ can be derived as follows:

$$G_{appr}(s) = V \prod_{k=-N}^N \frac{s + \omega'_k}{s + \omega_k},$$

where N is a pre-specified integer, and the zeros, poles, and the gain can be evaluated from

$$\omega'_k = \omega_b \left(\frac{\omega_h}{\omega_b} \right)^{\frac{k+N+\frac{1}{2}(1-\gamma)}{2N+1}},$$

$$\omega_k = \omega_b \left(\frac{\omega_h}{\omega_b} \right)^{\frac{k+N+\frac{1}{2}(1+\gamma)}{2N+1}},$$

$$V = \left(\frac{\omega_h}{\omega_b} \right)^{-\frac{\gamma}{2}} \prod_{k=-N}^N \frac{\omega_k}{\omega'_k}.$$

Digital Approximation

However, the Oustaloup approximation can not be directly used in digital control because of digital accuracy issues. s^λ can also be realized by the Impulse Response Invariant Discretization (IRID) method [66] in time domain, where a discrete-time finite dimensional (z) transfer function is computed to approximate the continuous irrational transfer function

s^λ , s is the Laplace transform variable, and λ is a real number in the range of $(-1, 1)$. s^λ is called a fractional order differentiator if $0 < \lambda < 1$ and a fractional order integrator if $-1 < \lambda < 0$. This approximation keeps the impulse response invariant.

4.5 Simulation Results

The proposed system identification algorithm and fractional order controller design techniques are first tested on the Aerosim simulation platform, a complete six degrees of freedom UAV dynamic model. For comparison, an integer order PID controller is also designed using modified Ziegler-Nichols tuning method. Both controllers are tested in scenarios including step response, wind gust response, and payload variation cases. Simulation results verify the advantage of FOC controllers over traditional PID controllers.

4.5.1 Introduction to Aerosim Simulation Platform

Aerosim is a nonlinear six degrees of freedom MATLAB Simulink model designed for the aerosonde UAV [67]. It is developed by Marius Niculescu from u-dynamics with the educational version for free with all the key blocks implemented through dynamic link libraries (dlls).

The control inputs of the aerosonde model include flap, aileron, elevator, rudder, throttle, and the wind. The outputs comprise of:

- System states including ground speed: v_n, v_e, v_d ; angular rate: p, q, r ; quaternion: q_0, q_1, q_2, q_3 ; position: p_n, p_e, h , etc.;
- Sensors measurements including GPS: $p_n, p_e, h, v_n, v_e, v_d$; inertial measurement unit (IMU): a_x, a_y, a_z, p, q, r ; wind: v_n^w, v_e^w, v_d^w ; magnetic: h_x, h_y, h_z .

The minimal simulation time step is $0.02s$ (50 Hz).

4.5.2 System Identification of Roll-Channel

According to the controller design procedure shown in Fig. 4.1, the trim tuning experiment is performed first in open-loop to get the control input trims for a steady flight state.

The trims are $\delta_a = 0$, $\delta_e = -3$ with throttle set as 0.7 (Aerosim does not provide the units for the above variables). It needs to be pointed out that δ_a may not be zero for real UAV platforms due to the manufacturing accuracy. Then the pitch-elevator loop and aileron-roll loop PID controllers should be added with references as shown in Fig. 4.3. For simplicity, the reference pitch angle is set as 0 all the time. The PID parameters are tuned roughly through step response analysis to achieve a steady flight.

A square wave is chosen as the reference input because no sensor noises are added in the simulation. The Steiglitz-Mcbride iteration method is used to get the ARX model of $\phi_{ref}-\phi$ loop. Here, time domain system identification method is chosen because the difficulties in choosing the trustable frequency range when analyzing the flight log. MATLAB function `stmcb` is used to get the models including: 1st order ARX model, 5th order ARX model, and first order plus time delay (FOPTD) model simplified from the 5th order ARX model.

$$G_1(s) = \frac{13.86}{s + 13.76} = \frac{1.0073}{0.0727s + 1}, \quad (4.24)$$

$$G_2(s) = \frac{N_1(s)}{D_1(s)}, \quad (4.25)$$

$$G_3(s) = \frac{1.0336e^{-0.0491s}}{0.0440s + 1}, \quad (4.26)$$

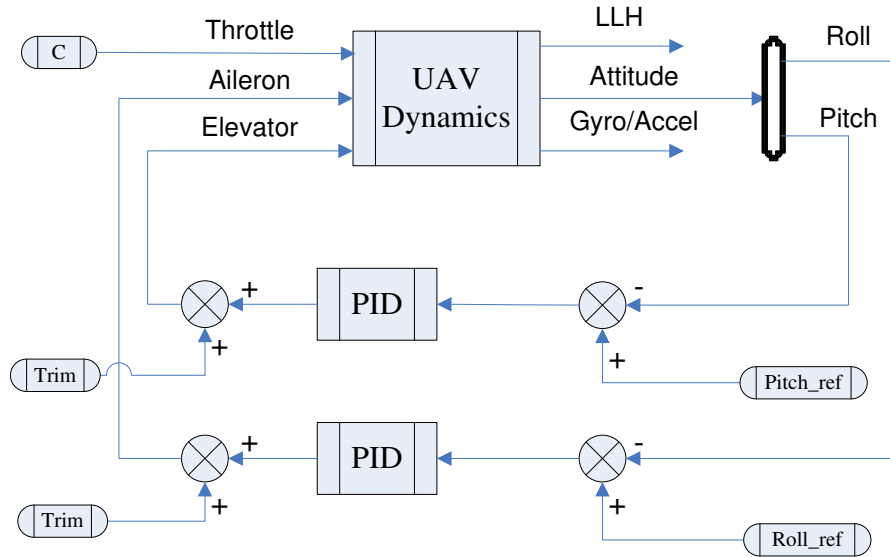


Fig. 4.3: UAV flight controller design procedure.

where $N_1(s) = -9.393s^4 + 553.8s^3 + 952.8s^2 + 10960s - 632.9$ and $D_1(s) = s^5 + 21.15s^4 + 662.1s^3 + 1705s^2 + 10920s - 612.3$.

The roll reference $R(N)$ and the roll angle $Y(N)$ are shown together with the simulated square wave responses from the identified models in Fig. 4.4. It can be seen that the simulated time domain responses match the outputs from Aerosim nonlinear model quite accurately for both the first order and the fifth order ARX models. The order of five is decided based on numerical experiments.

4.5.3 Fractional Order PI Controller Design Procedure

Given the first order model identified above, it can be written as $K = 1.0073 \text{ rad.}^{-1}$, $T = 0.0727 \text{ sec.}$ as (4.14). The fractional order PI controller to be designed is shown in Fig. 4.5.

The procedure of parameter selection is summarized as below:

(1) The controller performance specifications are chosen as $\omega_c = 10 \text{ rad./sec.}$, $\phi_m = 70^\circ$;

(2) The graphic plotting method is used to find the solution for the FOPI parameters.

Plot the curve of K_i versus λ according to (4.17), and plot the curve of K_i with respect to λ according to (4.18). The values of λ and K_i can be obtained from the intersection of the two curves, which reads $\lambda = 1.111$, $K_i = 28.31 \text{ rad.}^{-1}$;

(3) K_p can be calculated from (4.19), $K_p = 0.5503 \text{ rad.}^{-1}$;

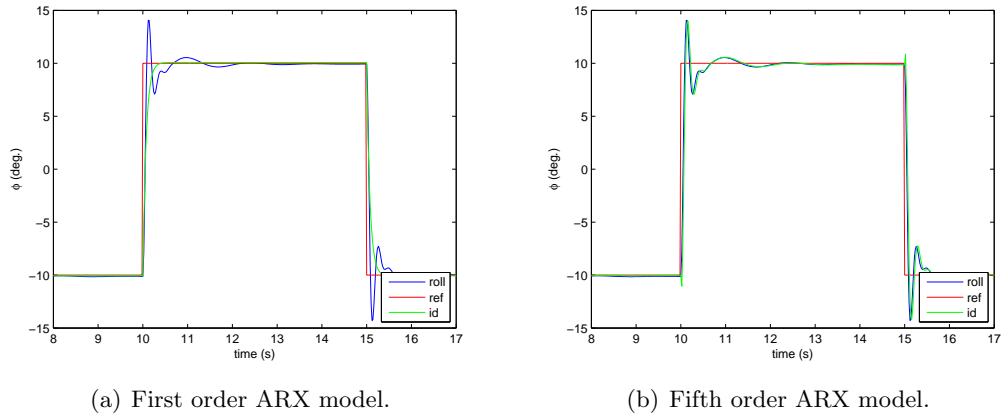


Fig. 4.4: System identification of roll-channel.

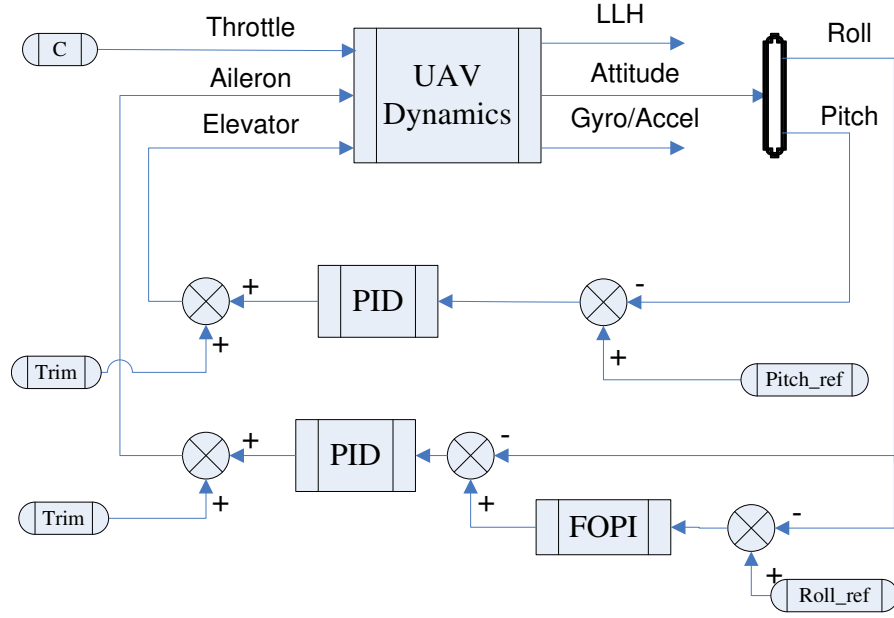


Fig. 4.5: FOPI flight controller.

(4) Then the designed fractional order PI controller needs to be validated first, with $K_p = 0.5503 \text{ rad.}^{-1}$, $K_i = 28.31 \text{ rad.}^{-1}$, $\lambda = 1.111$. The Bode plots of the system designed are plotted in Fig. 4.6. It can be seen that the phase Bode plot is flat, at the gain crossover frequency, all three specifications are satisfied precisely.

The Oustaloup realization of FOC controller is used in simulation [65]. The related parameters are chosen as $N = 3$, $\omega_b = 0.05 \text{ rad./sec.}$, $\omega_h = 50 \text{ rad./sec.}$

4.5.4 Integer Order PID Controller Design

As one of the most popular PID controller tuning rules, Modified Ziegler-Nichols (MZN) PID tuning rule is chosen to make a comparison with the designed FOPI controller. MZN tuning method [60] divides the tuning problem into several cases based on different system dynamics:

- Lag dominated dynamics ($L < 0.1T$): $K_p = 0.3T/K/L$, $K_i = 1/(8L)$;
- Balanced dynamics ($0.1T < L < 2T$): $K_p = 0.3T/K/L$, $K_i = 1/(0.8T)$;
- Delay dominated dynamics ($L > 2T$): $K_p = 0.15/K$, $K_i = 1/(0.4L)$.

The first order plus time delay (FOPTD) model is identified as $L = 0.0491$ sec., $T = 0.0440$ sec. It falls into the balanced dynamics category. So, the PID parameters are designed as $K_p = 0.2601$ rad. $^{-1}$, $K_i = 28.4091$ rad. $^{-1}$, $K_d = 0$. The step response comparison (10° for roll tracking) using Modified Ziegler-Nichols (MZN) controller and FOPI controller are shown in Fig. 4.7. It can be observed that the designed FOPI controller respond more quickly and settle faster than the IOPI controller.

4.5.5 Comparison

To show the advantages of FOPI controller over integer order PID controller, two more experiments were performed to examine the robustness. Wind gusts are very common and nontrivial disturbances to the flight control system. Especially for small or micro UAVs, the wind gust can cause crashes if the controller is not well designed. So both FOPI controller and MZN PID controller are tested under extreme conditions when the wind gust arrives 10 m./sec. for 0.25 second. The results are shown in Fig. 4.8. It can be seen that the FOPI

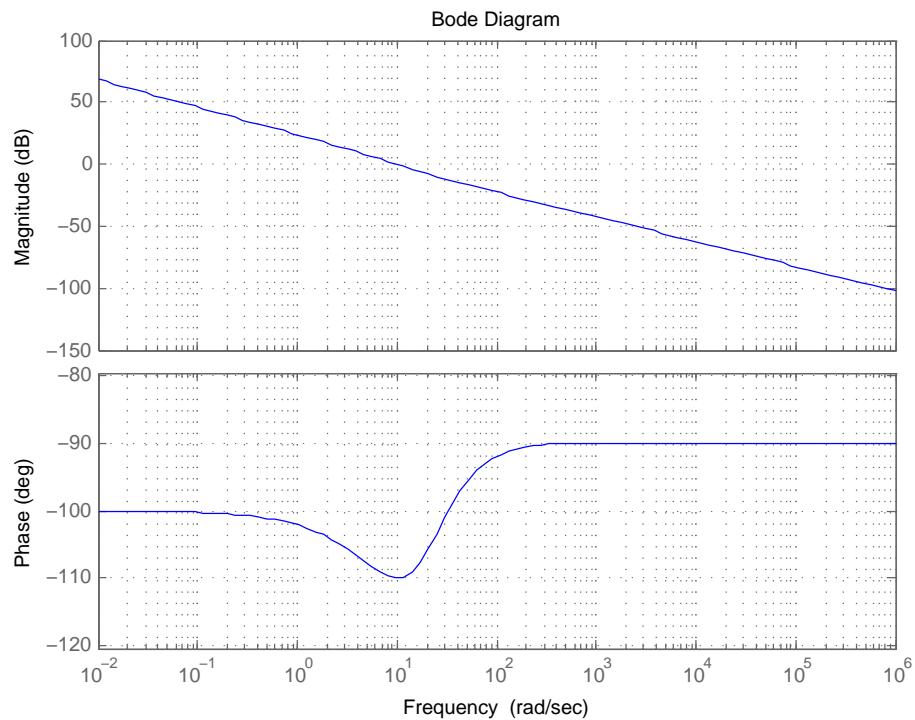


Fig. 4.6: Bode plot with designed FOPI controller.

controller has less overshoot than the MZN PID one and returns to the steady state faster.

Payload variation is also a big issue for small and micro UAVs since the payload can have a big impact on the flight performance. It could be useful if the controller could adapt itself for different sensor payloads. A controller robust to the payload variations could save the UAV end users a lot of time while changing different payloads. To demonstrate the robustness to payload, different controller gains $C1(s)$ are tested with $80\%K$ and $120\%K$ of the original roughly tuned proportional gain, shown in Fig. 4.9. The final step response plots show that the FOPI controller is more robust as compared to the MZN PI controller.

4.6 UAV Flight Testing Results

Real-flight test results are provided in this section together with the implementation details. The AggieAir2 UAV platform is used to test the proposed fractional order PI controller.

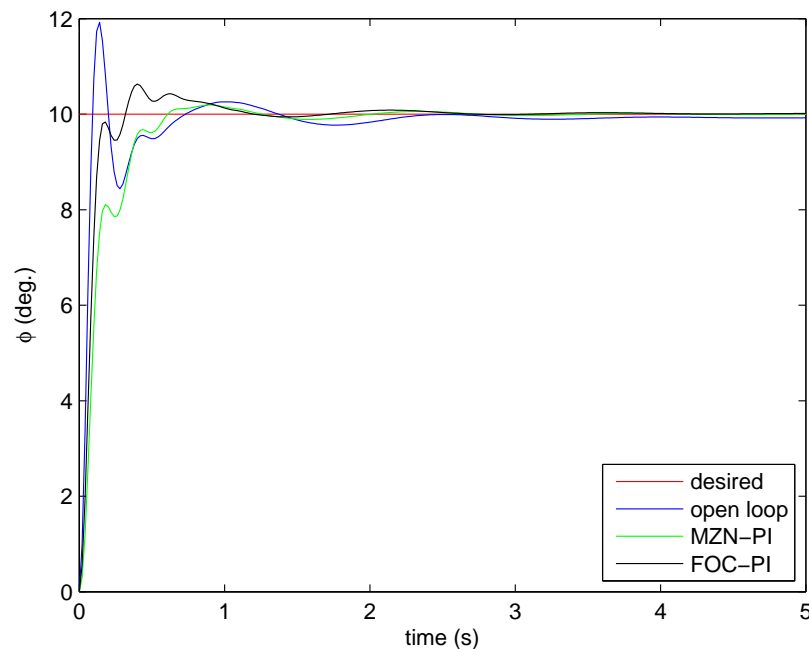


Fig. 4.7: Step response comparison: modified Z-N versus FOPI.

4.6.1 The ChangE UAV Platform

ChangE, an AggieAir UAS platform [68] developed at CSOIS, is used as the experimental platform for the flight controller design and validation [69]. It is built by the authors from the delta wing RC airframe called Unicorn. The UAV airborne system includes inertial sensors (Microstrain GX2 IMU and u-blox 5 GPS receiver), actuators (elevon and throttle

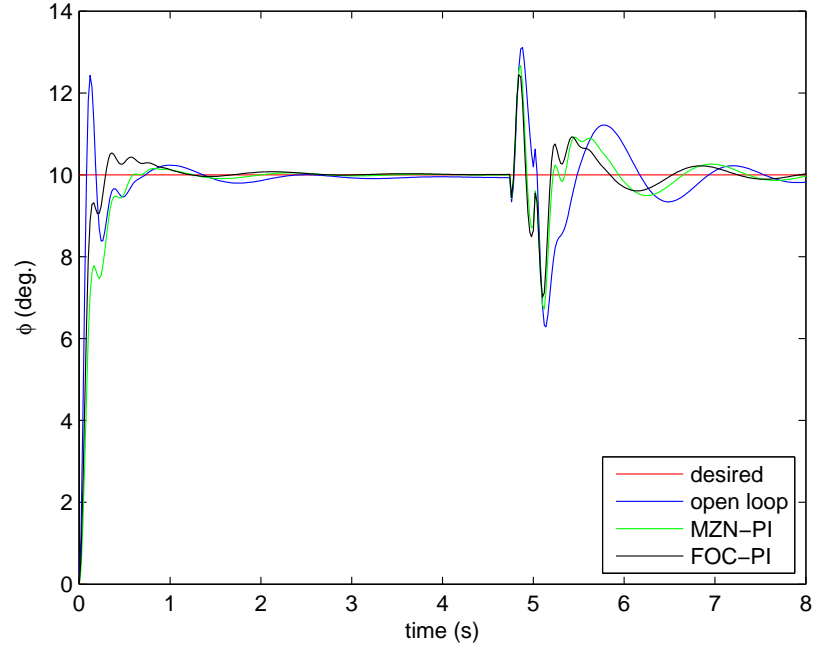


Fig. 4.8: Robustness to wind disturbance.

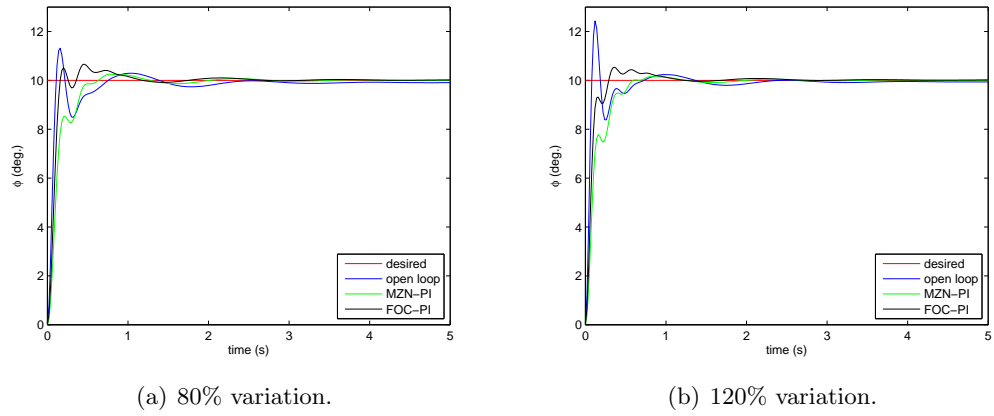


Fig. 4.9: Effects of payload gain variations.

motor), a data modem, an open source Paparazzi Tiny Twog autopilot, and lithium polymer batteries, as shown in Fig. 4.10. The Microstrain GX2 IMU could provide angle readings (ϕ, θ, ψ) at up to 100 Hz with a typical accuracy of $\pm 2^\circ$ under dynamic conditions [22]. The major specifications of the ChangeE UAV are shown in Table 4.1.

The ChangeE UAV has both manual RC control mode and autonomous control mode. It communicates with the ground control station (GCS) through a 900 MHz serial modem. The navigation waypoints and flying modes could be changed in real-time from the GCS,

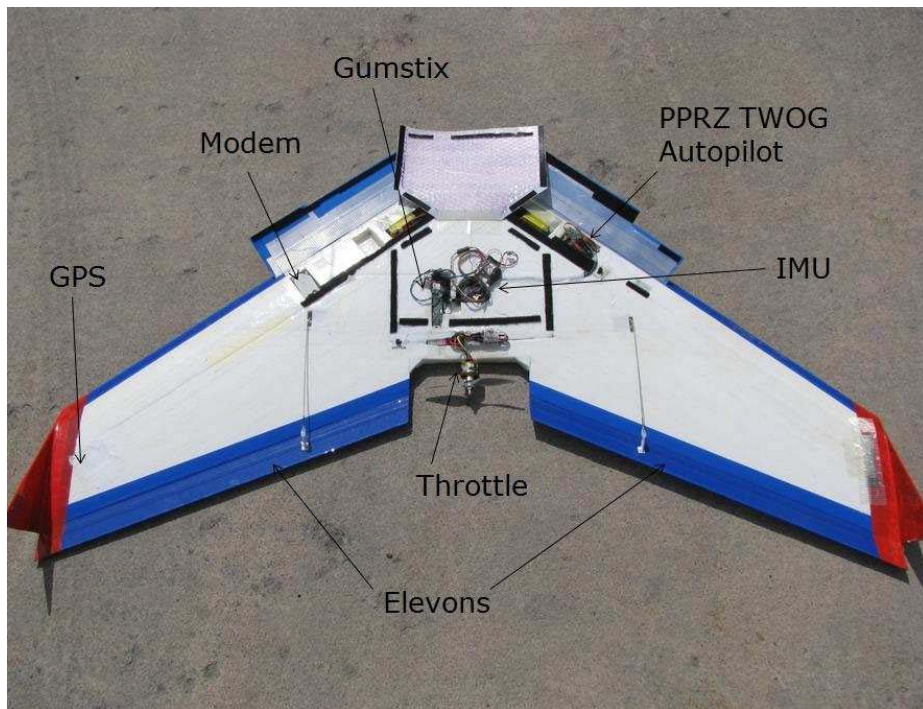


Fig. 4.10: ChangeE UAV platform.

Table 4.1: ChangeE UAS specifications.

ChangeE UAV	Specifications
Weight	about 5.5 lbs
Wingspan	60"
Control Inputs	elevon and throttle
Flight Time	≤ 1 hour
Cruise Speed	15 m./sec.
Take-off	bungee
Operational Range	up to 5 miles

shown in Fig 4.11. The safety pilot could also switch between the manual and autonomous control mode through the RC transmitter in case of emergency. In addition, the Paparazzi GCS software provides on-line parameter changing and plotting functions, which could be easily modified for in-flight tuning of the user-defined controller parameters.

4.6.2 System Identification

The steady flight tuning is the first step to do a roll-loop system identification. The UAV needs to be manually tuned first to achieve a steady state flight with zero trim on the elevon at the nominal throttle, which is chosen as 70% based upon the RC flight experiences. The Paparazzi flight controller is replaced by the user designed flight controller (Aggie controller inner loop) both at 60 Hz, as shown in Fig. 4.3. Both the inner roll and pitch PID controllers only include the proportional part. The inner K_p for roll loop is selected as 10038 count/rad., or the maximum value before oscillations is observed by the RC safety pilot. The aileron control inputs are limited within $[-9600, 9600]$ counts. The square response ($[-20^\circ, 20^\circ]$) is generated for the system identification. The reference pitch angle is set as zero all the time. The system response (roll) and the reference roll angle are shown in

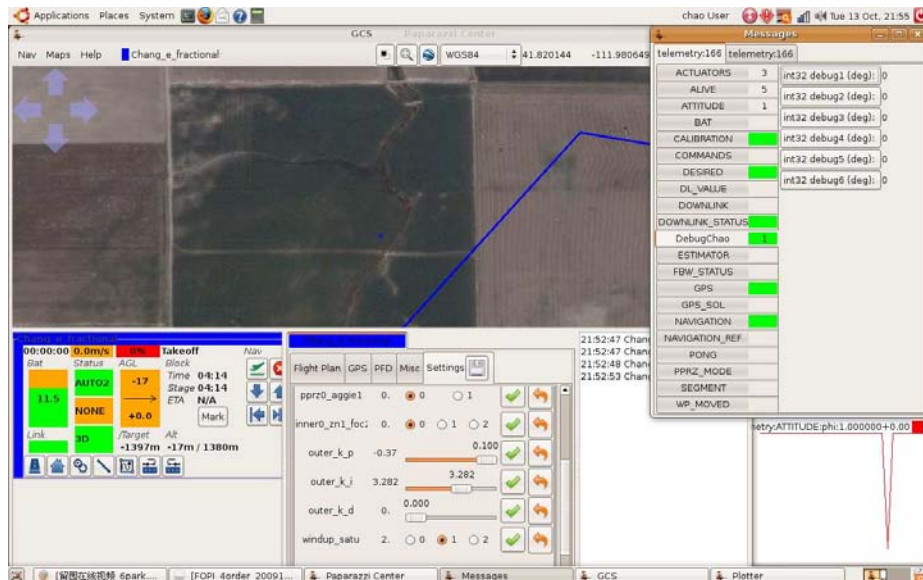


Fig. 4.11: Paparazzi GCS.

Fig 4.12.

The first order ARX model of $\phi_{ref} - \phi$ loop is then calculated based on the flight data log (20 Hz) using least squares algorithm as follows:

$$G(s) = \frac{1.265}{0.901s + 1}.$$

The 5th-order ARX model of $\phi_{ref} - \phi$ loop is also calculated based on the flight log (20 Hz) using least squares algorithm as:

$$G(s) = \frac{N_2(s)}{D_2(s)},$$

where $N_2(s) = 0.06108s^5 - 6.825s^4 + 593.2s^3 - 15720s^2 + 220300s + 1071000$ and $D_2(s) = s^5 + 361.5s^4 + 28940s^3 + 136900s^2 + 929000s + 1081000$.

The square wave responses based on the identified model are simulated and plotted together with the real system response in Fig 4.12. “id5” means the identified 5th-order

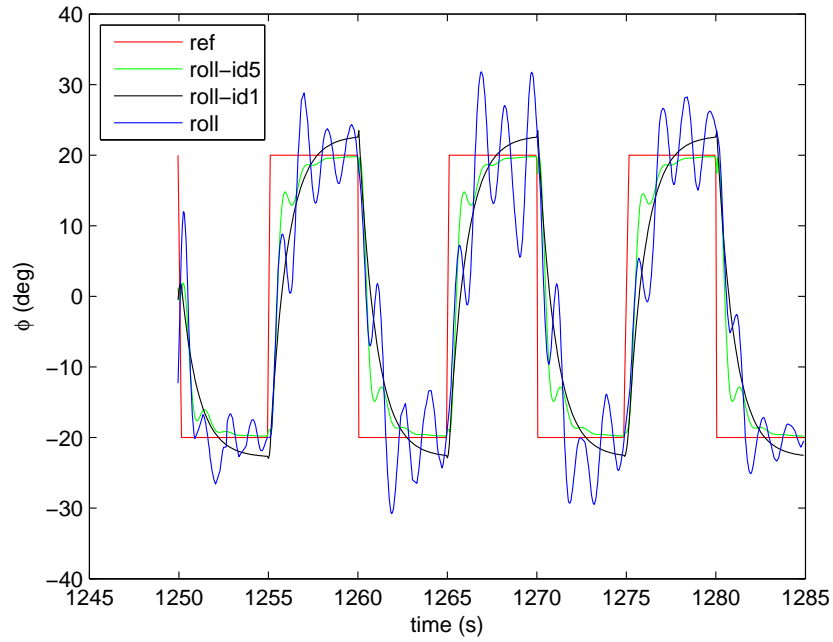


Fig. 4.12: Roll-channel system identification.

ARX model and “id1” means the 1st-order one. It can be seen that the response of the identified model can track the reference signal, and the 5th-order ARX model identified has better transient responses compared to the first order ARX model.

The FOPTD model could be calculated from the 5th-order ARX model above using `getfoptd` function [60]:

$$G(s) = 0.9912 \frac{e^{-0.2793s}}{0.3414s + 1}. \quad (4.27)$$

4.6.3 Proportional Controller and Integer Order PI Controller Design

Given the FOPTD model identified above (4.27), a proportional controller could be designed using Ziegler-Nichols tuning rule [60],

$$K_p = \frac{1}{KL/T} = 1.2332.$$

The actual roll tracking result for square reference is shown in Fig. 4.13. It is obvious that the proportional controller has a hard time tracking the roll reference smoothly without overshoots. At the same time, the steady-state tracking error with the designed proportional controller is clearly shown.

Similarly, an integer order PI controller could be designed using Modified Ziegler-Nichols tuning rule based upon the identified FOPTD model (4.27),

$$K_p = \frac{0.3T}{KL} = 0.37, \quad K_i = 0.8T = 3.66.$$

The actual step tracking result with this designed integer order PI controller are shown in the later section.

4.6.4 Fractional Order PI Controller Design

The 60-inch UAV model is identified as the first order plus time delay (FOPTD) system in (4.27). According to this model, the design procedure of the fractional order PI controller is summarized below,

(1) Given $T=0.3414$ sec., $\omega_c=1.3$ rad./sec., $\phi_m=80^\circ$;

(2) Plot curve 1, K_i with respect to λ and plot curve 2, K_i with respect to λ based on part I. Obtain the values of λ and K_i from the intersection point on the above two curves, which reads $\lambda = 1.1546$, $K_i = 1.482$;

(3) Calculate the K_p from (4.23), $K_p = 0.8461$;

(4) Then the designed fractional order PI controller can be obtained.

The fractional order part $1/s^{0.1546}$ could be approximated by a 4th-order discrete controller using IRID algorithm (sampling period $T_s = 0.0167$ sec.) [66]:

$$G(z) = \frac{N(z)}{D(z)},$$

where $N(z) = 0.5203z^4 - 1.1750z^3 + 0.8691z^2 - 0.2245z + 0.0117$, $D(z) = z^4 - 2.4276z^3 + 1.9873z^2 - 0.6062z + 0.0478$.

The Bode plot of $G(z)$ is shown in Fig. 4.14. It can be observed that the 4th-order discrete controller could approximate the frequency response of $1/s^{0.1546}$ around the gain

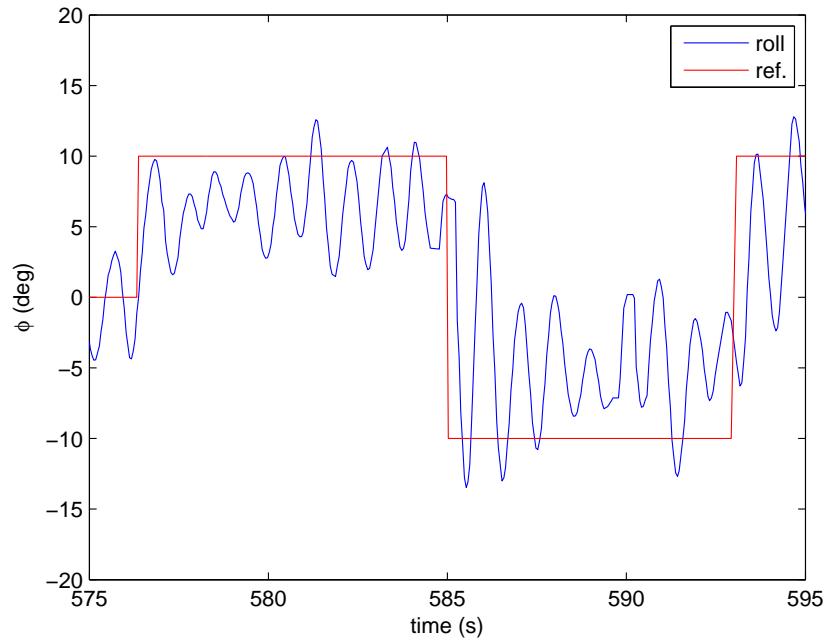


Fig. 4.13: Proportional controller for outer roll loop.

crossover frequency 1.3 rad./sec. of the open-loop system designed.

An anti-windup block is also added for both the FOPI and IOPI controllers shown in Fig. 4.15. k_t is chosen as $2K_i$.

4.6.5 Flight Test Results

To make a fair comparison between controllers designed using the modified Ziegler-Nichols tuning rule and using the flat phase FOPI tuning rule, the flight tests were conducted

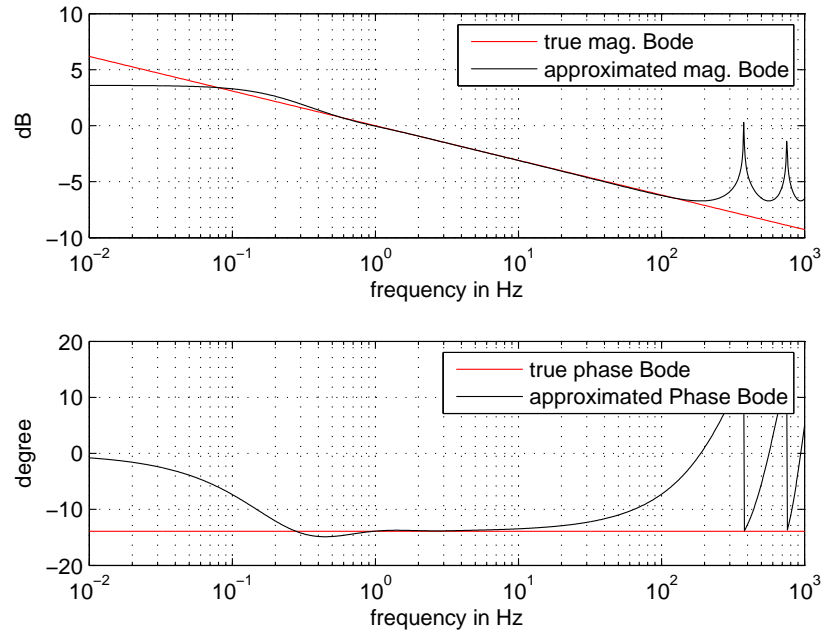


Fig. 4.14: Bode plot of $G(z)$.

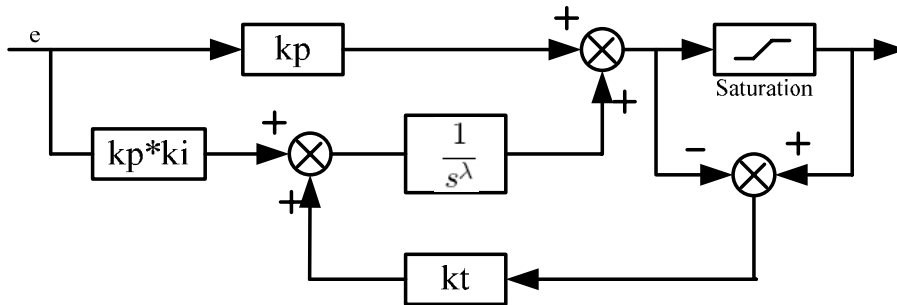


Fig. 4.15: Anti-windup for FOPI and IOPI controllers.

for three hours on October 21st, 2009, in the Cache Junction research farm owned by Utah State University. The wind on the ground was predicted to be 0.45-0.9 m./sec. (1-2 mile/hour). Figure 4.16 shows one of the five flight tests for both IOPI and FOPI controllers. The results are fairly repeatable and reproducible. The designed FOPI controller could track the step 10° within the sensor resolution range $\pm 2^\circ$ [22]. From Fig. 4.16, it can be observed and concluded that the designed FOPI controller outperforms the designed IOPI controller in both the rise time and overshoot.

The FOPI flight controller is also tested under various system gains to show the robustness of the FOPI controller, shown in Fig. 4.17. It can be observed that the rise time with the FOPI controller is shorter than that with the IOPI controller.

4.7 Chapter Summary

In this chapter, the fractional order proportional integral (FOPI) controller is designed and implemented on the roll loop of a small UAV. To the authors' best knowledge, it is the first fractional order flight controller that has been implemented to guide the UAV in

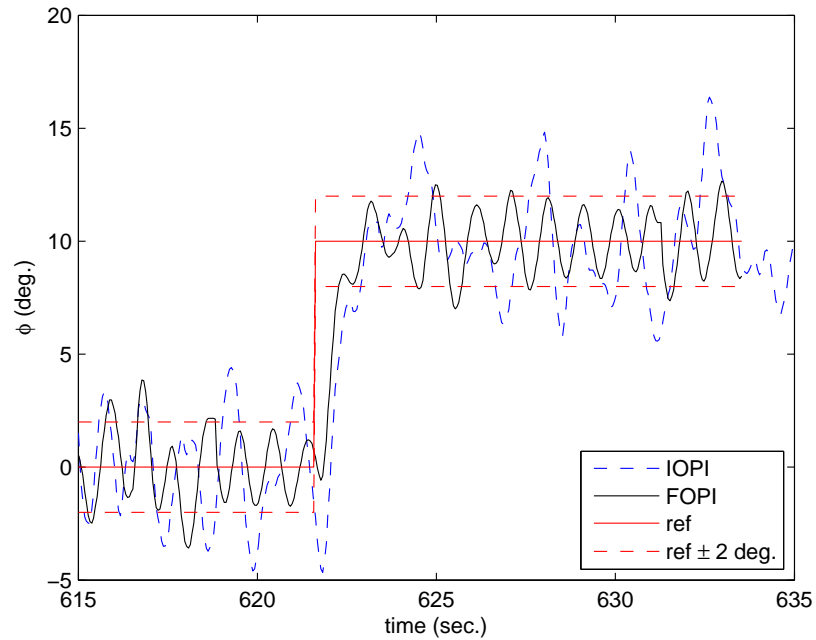
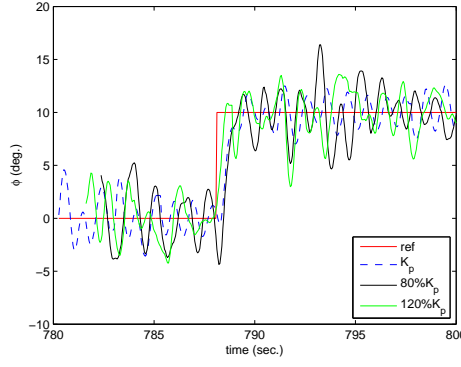
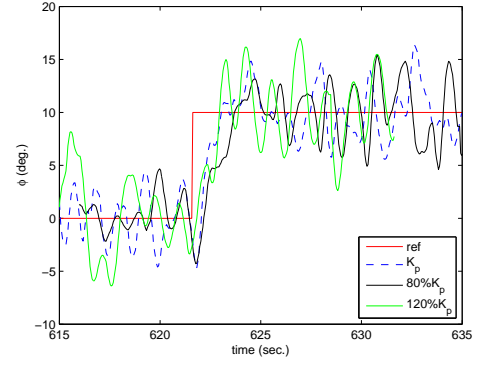


Fig. 4.16: FOPI controller for outer roll loop.



(a) FOPI controller.



(b) IOPI controller.

Fig. 4.17: FOPI versus IOPI controller with various system gains.

autonomous flights. Both simulation results and real-flight test data show the effectiveness of the proposed controller design techniques. Future work is to make more comparisons between IOPI and FOPI controller performance for different scenarios like various wind conditions, various payloads, etc.

Chapter 5

Single UAV-Based Remote Sensing

For the mission of remote sensing of an environmental or agricultural system, the ground-based sensing device can provide a highly accurate mapping but with a limited range (inch level spatial resolution and second level temporal resolution). Satellite photos can provide global level resolution with a large range (30-250 meter or lower spatial resolution and week level temporal resolution). But these photos are expensive and cannot be updated at arbitrary spatial or temporal scales. Small UAVs can provide a high resolution (meter or centimeter spatial resolution and hour-level temporal resolution) even with an inexpensive camera since most UAVs do not fly so high as satellites.

UAVs equipped with imagers have been used in several agricultural remote sensing applications. High resolution red-green-blue (RGB) aerial photos can be used to determine the best harvest time of wine grapes [18]. Multispectral images are also shown to be potentially useful for monitoring the ripeness of coffee [16]. However, most current UAV remote sensing applications use large and expensive UAVs with heavy cameras and collect only one band of aerial imagery. As mentioned in Chapter 2, AggieAir UAS is a low-cost multi-spectral system for this remote sensing mission. This chapter considers the problem of using a single UAV for the remote sensing missions. Firstly, the remote sensing requirements for water management and irrigation control are discussed, and the problem is divided into two subproblems. The path planning algorithm is introduced to solve the coverage control subproblem. Then, the georeference subproblem is considered with different image stitching and registration techniques. Finally, several typical example missions together with real UAV flight test results are provided including land survey, water area survey, riparian applications, and remote data collection.

5.1 Motivations for Remote Sensing

5.1.1 Water Management and Irrigation Control Requirements

The goal of irrigation control is to minimize the water consumption while sustaining the agriculture production and human needs [70]. This optimization problem requires remote sensing to provide real-time feedback from the field including:

- Water: Water quantities and qualities with temporal and spatial information, for example the water level of a canal or lake;
- Soil: Soil moisture and type with temporal and spatial information;
- Vegetation: Vegetation index, quantity and quality with temporal and spatial information, for example the stage of growth of the crop.

The “real time” here means daily or weekly temporal resolution based on different applications.

5.1.2 Introduction of Remote Sensing

The purpose of remote sensing is to acquire information about the Earth’s surface without coming into contact with it. One objective of remote sensing is to characterize the electromagnetic radiation emitted by objects [15]. Typical divisions of the electromagnetic spectrum include the visible light band (380-720 nm), near infrared (NIR) band (0.72-1.30 μm), and mid-infrared (MIR) band (1.30-3.00 μm). Band-reconfigurable imagers can generate several images from different bands ranging from visible spectra to infrared or thermal bands for various applications. The advantage of an ability to examine different bands is that different combinations of spectral bands can have different purposes. For example, the combination of red-infrared can be used to detect vegetation and camouflage and the combination of red slope can be used to estimate the percent of vegetation cover [16].

After the acquisition of images, further analysis must be made. One widely used processing technique is the normalized difference vegetation index (NDVI) [71]:

$$NDVI = \frac{CH_{NIR} - CH_{RED}}{CH_{NIR} + CH_{RED}}, \quad (5.1)$$

where CH_{NIR} and CH_{RED} are spectral reflectance measurements of red and NIR bands. There are also other vegetation index methods, such as the enhanced vegetation index (EVI), soil adjusted vegetation index (SAVI) [71], etc.

The remote sensing problem is defined in detail in Chapter 2. Here only a brief statement is provided. Given an arbitrary area $\Omega \subset R^2$, the goal of remote sensing is to make a mapping from Ω to $\eta_1, \eta_2, \eta_3, \dots$, representing the density functions for different spectral bands, with preset spatial and temporal resolutions for any $q \in \Omega$ and any $t \in [t_1, t_2]$.

5.2 Remote Sensing Using Small UAVs

Small UAVs are UAVs that can be operated by only one or two people with a flight height less than 10,000 feet above the ground surface. Many of them can be hand-carried and hand-launched. Small UAVs with cameras can easily achieve a meter-level spatial resolution because of their low flight heights. However, this also leads to a smaller footprint size which represents a limitation on the area that each image can cover. In other words, more georeferencing work is needed to stitch or put images taken at different places together to cover a large-scale water system. Thus, the UAV remote sensing mission can be divided into two subproblems:

- Coverage control problem: The path planning of the UAV to take aerial images of the whole domain Ω ;
- Georeference problem: The registry of each pixel from the aerial images with both temporal and spatial information. For example, the GPS coordinates and time the picture was taken.

There can be two types of solutions. The open-loop solution is to solve the two sub-problems separately with the path planning before the UAV flight, and with the image georeferencing after the flight. This method is simple and easy to understand but requires significant experiences to set up all the parameters. The closed-loop solution is to do the path planning and georeference in real-time so that the information from the georeference part can be used as the observer for the path planning controller. This chapter focuses on an open-loop solution.

5.2.1 Coverage Control

Given an arbitrary area Ω , UAVs with functions of altitude and speed keeping and waypoint navigation: speed $v \in [v_1, v_2]$, possible flight height $h \in [h_1, h_2]$; camera with specification: focal length F , image sensor pixel size $PS_h \times PS_v$, image sensor pixel pitch $PP_h \times PP_v$; the interval between images acquired by the camera (the “camera shooting interval”) t_{shoot} , the minimal shooting time $t_{shoot_{min}}$, the desired aerial image resolution res ; the control objective is:

$$\min t_{flight} = g(\Omega, h, v, \{q_1, \dots, q_i\}, t_{shoot}, res), \quad (5.2)$$

subject to $v \in [v_1, v_2]$, $h \in [h_1, h_2]$, $t_{shoot} = k \times t_{shoot_{min}}$, where t_{flight} is the flight time of the UAV for effective coverage, $g(\Omega, h, v, t_{shoot})$ is the function to determine the flight path and flight time for effective coverage, k is a positive integer.

The control inputs of the coverage controller include bounded velocity v , bounded flight height H , a set of preset UAV waypoints $\{q_1, q_2, \dots, q_i\}$ and the camera shooting interval t_{shoot} . The system states are the real UAV trajectory $\{\bar{q}_{t_1}, \dots, \bar{q}_{t_2}\}$ and the system output is a series of aerial images or a video stream taken between t_1 and t_2 .

Assume that the imager is mounted with its lens vertically pointing down into the Earth; its footprint (shown in Fig. 5.1) can be calculated as:

$$FP_h = \frac{h \times PP_h \times PS_h}{F}, FP_v = \frac{h \times PP_v \times PS_v}{F}.$$

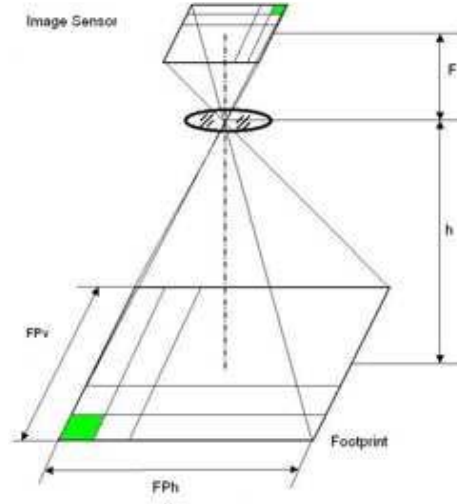


Fig. 5.1: Footprint calculation.

Most UAVs can maintain the desired altitude while taking pictures so the UAV flight height h can be determined first based on camera and resolution requirements. Assuming that different flight altitudes have no effect on the flight speed for small UAVs, we get

$$h = \frac{\sqrt{res} \times F}{\max(PP_h, PP_v)}. \quad (5.3)$$

Given the flight height h and the area of interest Ω , the flight path, cruise speed, and camera shooting interval must also be determined. Without loss of generality, Ω is assumed to be a rectangular since most other polygons can be approximated by several smaller rectangles. The most intuitive flight path for UAV flight can be obtained by dividing the area into strips based on the group spatial resolution, shown in Fig. 5.2(a). The images taken during UAV turning are not used for our remote sensing missions because all the aerial images should have similar resolutions for georeferencing simplicities. Due to the limitation from the UAV autopilot, GPS accuracy and wind, the small UAV cannot follow a straight line perfectly along the preset waypoints. To compensate the overlapping percentage between two adjacent sweeps, o must also be determined before flight; this compensation is based on experiences from the later image stitching as shown in Fig. 5.2(b) [17].

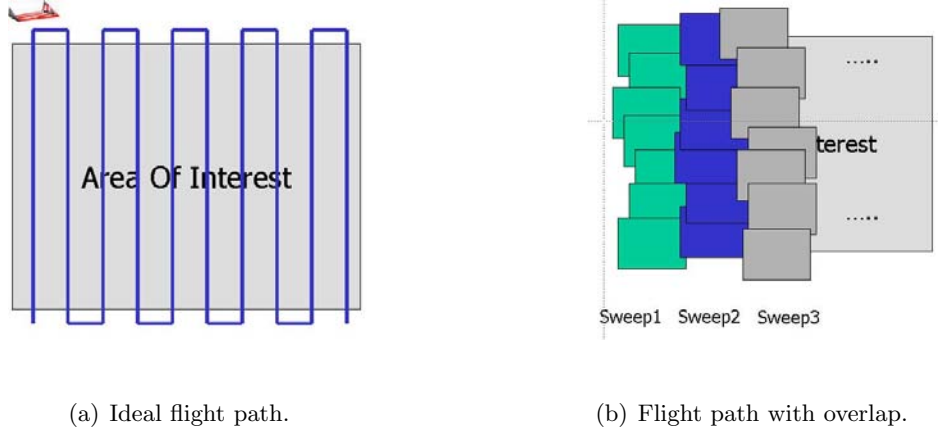


Fig. 5.2: UAV flight path.

Given the overlapping percentage $o\%$ between sweeps, the ground overlapping o_g can be determined by:

$$o_g = (1 - o\%) \times FP_h. \quad (5.4)$$

The minimal camera shooting interval can be computed as:

$$t_{shoot_{min}} = \frac{(1 - o\%) \times FP_v}{v}. \quad (5.5)$$

This open-loop solution is intuitive, robust to all the polygons and requires little computations. However, this method requires that many parameters, especially the overlapping percentage $o\%$ to be set up based on experiences; it cannot provide an optimal solution. More work on a closed-loop real-time solution is needed for an optimal solution.

5.2.2 Georeference Problem

After the aerial images are taken and sent back to the ground, post flight image processing is needed since the UAV cannot maintain perfectly level flights all the time [72,73].

Problem Statement for Post Flight Image Stitching

Given the aerial images stream $\{I_1, I_2, \dots, I_m\}$ and the UAV flight data logger stream $\{t_1, \dots, t_n\}, \{q_1, \dots, q_n\}, \{\psi_1, \dots, \psi_n\}, \{\theta_1, \dots, \theta_n\}, \{\phi_1, \dots, \phi_n\}$, map $\eta(R^3, \psi, \theta, \phi, t)$ back to $\eta(R^2, 0, 0, \phi, t)$, where ψ , θ and ϕ represent the roll, pitch, and yaw angles, respectively.

This problem can be solved by feature-based mapping, or GIS-based mapping, or both.

Feature-Based Stitching

With feature-based stitching, the aerial images are stitched together based on some common features such as points, lines, or corners. These features can either be specified manually by humans or recognized automatically by some algorithms. For example, PTGui software needs reference points to perform image stitching [74]. This method works well for photos sharing several common features. A simple example is shown in Fig. 5.3 and Fig. 5.4 [17]. The aerial photos were taken at about 150 meters above the ground by a GF-DC mounted on an RC airplane controlled by a human operator. The problem with this method is that the photos are not georeferenced, and with no absolute coordinates to tie to. The error can keep increasing with the image numbers. Because of the small image footprint of small UAVs and the lack of permanent distinguishing features of most agricultural fields, it is almost impossible to find enough common features in every picture to correctly tie the photos together. There are also feature-based stitching methods that georeference the photos. These take features on each photo and compare them to photos which already have GIS information. This method performs the stitching task better because each photo is georeferenced and has some absolute coordinates to tie to. However, the photos with the GIS information are often taken once a year. For some photos taken from the UAV, they are not current enough to find similar features.

UAV Position and Attitude-Based Stitching

This method uses the data from the UAV including q , θ , ϕ , ψ to map the image back to the related ground frame and registry each pixel with its ground coordinates and electromagnetic density measurements. The advantage is that this method uses all the information from the UAV and can guarantee a bounded global error even for the final big image. However, it requires perfect synchronization between the aerial images and the attitude logs, which means the full authority in UAV autopilot and sensor package. The inability to access the autopilot code is one of the disadvantages of using off-the-shelf UAVs



Fig. 5.3: Photos before stitch.

for remote sensing missions.

A three-dimensional (3D) mesh M_{hw} must first be generated in F_{cam} [17], which describes the spatial distribution of its corresponding image. This mesh has $n \times n$ elements, illustrated in Fig. 5.5 [35]. Each element of (M_{hw}) can be calculated as:

$$q(w, h)_{cam} = \begin{bmatrix} x(w, h)_{cam} \\ y(w, h)_{cam} \\ f \end{bmatrix}, \forall q(w, h)_{cam} \in M_{wh}, \quad (5.6)$$

$$x(w, h)_{cam} = \frac{S_w(2w - n)}{2n}, y(w, h)_{cam} = \frac{S_h(2h - n)}{2n},$$

where $w, h \in [1, n]$, f is the focal length of the camera, w is the column index of the mesh, h is the row index of the mesh, S_w and S_h are the width and height of the image sensor, respectively.

The mesh must be rotated first with respect to F_{body} , F_{nav} and then translated to the

ground frame F_{gps} . The manner in which the camera is mounted on the UAV body decides the rotation matrix R_{body}^{cam} , which can be a constant or a dynamic matrix. The angles (yaw, pitch, and roll ψ_c, θ_c, ϕ_c) describe the orientation of the camera with respect to the body frame.

$$R_{body}^{cam} = (R_{cam}^{body})^T = (R_{zyx}(\psi_c + 90, \theta_c, \phi_c))^T, \quad R_{body}^{cam}, R_{cam}^{body} \in SO(3). \quad (5.7)$$

The rotation matrix from F_{body} to F_{nav} can be determined from the orientation of the aircraft (ψ, θ, ϕ) with respect to the navigation coordinate system, which can be measured by the UAV onboard sensors.

$$R_{nav}^{body} = \begin{bmatrix} c_\theta c_\psi & -c_\phi s_\psi + s_\phi s_\theta c_\psi & s_\phi s_\psi + c_\phi s_\theta c_\psi \\ c_\theta s_\psi & c_\phi c_\psi + c_\phi s_\theta s_\psi & -s_\phi c_\psi + c_\phi s_\theta s_\psi \\ -s_\theta & s_\phi c_\theta & c_\phi c_\theta \end{bmatrix}, \quad R_{nav}^{body} \in SO(3), \quad (5.8)$$



Fig. 5.4: Photos after stitching.

where c_θ , s_θ stand for $\cos(\theta)$ and $\sin(\theta)$, respectively.

The rotation transformations can be then calculated with all the above rotation matrices as follows:

$$q_{nav} = R_{nav}^{body} R_{body}^{cam} q_{cam}, \quad (5.9)$$

The mesh now represents the location of the image sensor in the Navigation Frame F_{nav} . To represent the location of the picture on the Earth, the vectors in the mesh are scaled down to the ground. It is assumed that the Earth is flat because each picture has such a small footprint. q_{nav} is the element of the new projected mesh, $q_{nav}(z)$ is the z component of the element in the unprojected mesh, and h is the height of the UAV when the picture was taken.

$$q_{nav}^P = \frac{h}{q_{nav}(z)} q_{nav} \quad (5.10)$$

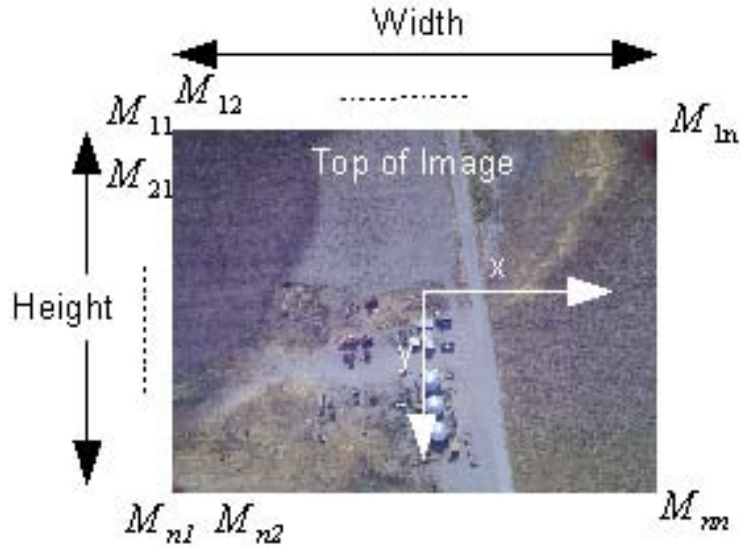


Fig. 5.5: Camera frame and mesh.

The elements of the mesh are now rotated into ECEF coordinates using the latitude (λ) and the longitude (φ) of the UAV when the picture was taken. Then the mesh is translated by the position vector (\vec{P}) of the UAV in ECEF coordinates.

$$R_{gps}^{nav} = R_{yyz}(-\lambda, 90^\circ, \varphi), \quad R_{gps}^{nav} \in SO(3), \quad (5.11)$$

$$q_{gps} = R_{body}^{nav} q_{nav}^P + \vec{P}. \quad (5.12)$$

After the above calculations, the meshes can be further processed by some 3D imaging software like NASA World Wind [37]. NASA World Wind can place the meshes correctly on the Earth and provide an interactive 3D displaying.

5.3 Sample Applications for AggieAir

Experimental results are shown in this section to demonstrate the effectiveness of the proposed algorithm for remote sensing missions using AggieAir, a small UAV. Several sample applications are introduced in detail. Firstly, a farmland coverage mission is introduced with the image stitching. Acquisition of photographic data for road survey, water area coverage, and riparian survey are illustrated involving the use of both the RGB and NIR imagers. Finally, a remote data collection application is offered to demonstrate the feasibility of using UAVs to collect data from ground-based sensors through wireless modems.

5.3.1 Farmland Coverage

This irrigation optimization problem requires remote sensing to provide real-time feedback from the farmland field including water, soil, and vegetation. The “real-time” here means daily or weekly temporal resolution based on different applications. The UAV is needed to measure the soil moisture of the area to help save water. More importantly, the ground probes and Landsat data can be used to calibrate the images from small UAVs

using the downscaling techniques [75, 76]. After calibration, these images should be able to measure soil moisture and evapotranspiration for water managers and farmers whenever it is needed. A research farm (one square mile) coverage map is provided in Fig. 5.6 to show the capability of AggieAir.

5.3.2 Road Surveying

AggieAir UAS can also provide low-cost aerial images for road and highway construction and maintenance. Figure 5.7 shows a highway intersection located in Logan Canyon, which was rebuilt in 2008 for better safety to turn onto the main road. The Utah Department of Transportation (UDOT) provides the picture taken by a manned aircraft before construction, shown in the left of Fig. 5.7. The aerial images acquired by AggieAir is shown in the right. It can be seen that the aerial images from AggieAir have a better resolution with feature-based stitching.



Fig. 5.6: Cache Junction farm coverage map (courtesy of A. M. Jensen for image stitching).



(a) Before construction (manned aircraft picture from UDOT).



(b) After construction (AggieAir picture).

Fig. 5.7: Beaver resort intersection (courtesy of A. M. Jensen for image stitching).

5.3.3 Water Area Coverage

Water areas include wetlands, lakes, or ponds, etc. Water areas could provide lots of information to ecological environment changes, flood damage predictions, and water

balance management. Desert Lake coverage mission is a typical example, which lies in west-central Utah (latitude: $39^{\circ}22'5''N$, longitude: $110^{\circ}46'52''W$). It is formed from return flows from irrigated farms in that area. It is also a waterfowl management area. This proposes a potential problem because the irrigation return flows can cause the lake to have high concentrations of mineral salts, which can affect the waterfowl that utilize the lake. Managers of the Desert Lake resource are interested in the affect of salinity control measures that have been recently constructed by irrigators in the area. This requires estimation of evaporation rates from the Desert Lake area, including differential rates from open water, wetland areas, and dry areas. Estimation of these rates requires data on areas of open water, wetland, and dry lands, which, due to the relatively small size and complicated geometry of the ponds and wetlands of Desert Lake, are not available from satellite images. A UAV can provide a better solution for the problem of acquiring periodic information about areas of open water, etc., since it can be flown more frequently and at little cost.

The whole Desert Lake area is about 2×2 miles. It is comprised of four ponds and some wetland areas. The early version of AggieAir imaging payload, GF-DV, is used in this mission together with real-time, simultaneous RGB and NIR videos. Both the RGB and NIR videos are transmitted back to the ground station in real-time. The photos are stitched using gRAID, shown in Fig. 5.8.

5.3.4 Riparian Surveillance

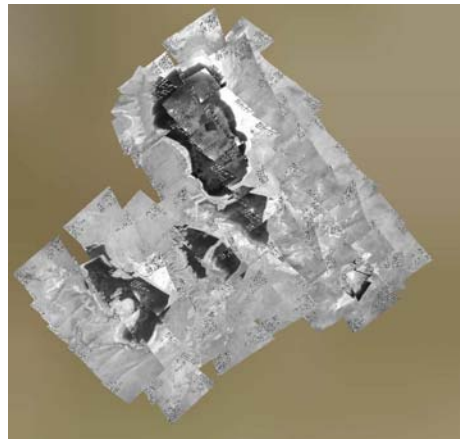
Riparian buffer surveillance is becoming increasingly more important since it is challenging to maintain stream ecosystem integrity and water quality with the current rapidly changing land use [77]. AggieAir UAS could be used in several applications including river tracking, vegetation mapping, and hydraulic modeling, etc.

River Tracking

The path and flow of a river might constantly change due to drought, flood, or other natural calamities. Because of this, the aerial images of the river path could be outdated or in low quality, making it difficult to perform studies of the changed river and the variations



(a) RGB image.



(b) NIR image.

Fig. 5.8: Desert lake coverage map (courtesy of A. M. Jensen for image stitching).

of its nearby ecological system. AggieAir UAS platform with the high-resolution multi-spectral camera system could present a real-time low-cost solution to the river tracking problem [78]. A flight plan with 3D waypoints could be formed by integrating flow line data from NHDPlus (National Hydrography Dataset Plus) and DEM (Digital Elevation Model) from USGS (U.S. Geological Survey). The images captured by the cameras are processed in real-time. Based on the information derived from these images, waypoints are dynamically generated for the autonomous navigation so that the UAV can exactly follow the changed river path and the focus of each image from the camera system is on the center of the river. The actual flight results collected in several flying experiments along a river

verify the effectiveness of AggieAir System, shown in Fig. 5.9. Example RGB and NIR pictures acquired by AggieAir is also shown in Fig. 5.10.

Vegetation Mapping and Hydraulic Modeling

In addition to agricultural applications, AggieAir is also a useful platform for riparian projects. Figure 5.11 shows some imagery taken with AggieAir of a small section of the Oneida Narrows near Preston, Idaho. A team of engineers used this imagery to map the substrate and vegetation for 2D hydraulic and habitat modeling. Normally, the team uses low-resolution, outdated imagery to map rivers. This can be difficult when the vegetation, the path and the flow of the river are always changing. The imagery from AggieAir, however, was up-to-date (within a week) and had high spatial resolution (5 cm), which made mapping the river quick and easy. Not only could different types of vegetation be distinguished from the imagery, but different types of sediment, like sand piles, could also be easily distinguished.

5.3.5 Remote Data Collection

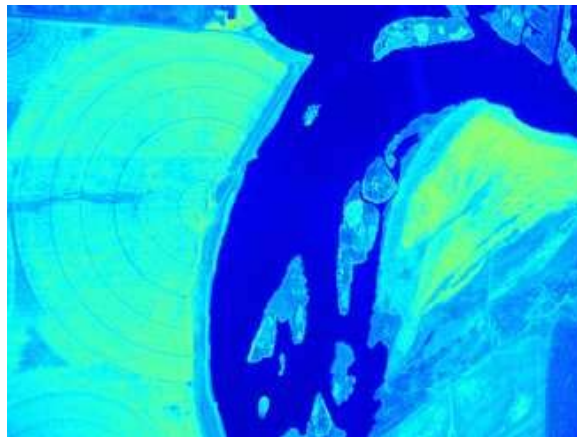
Many agricultural and environmental applications require deployment of sensors for



Fig. 5.9: River tracking map after stitching (courtesy of A. M. Jensen for image stitching).



(a) RGB image.



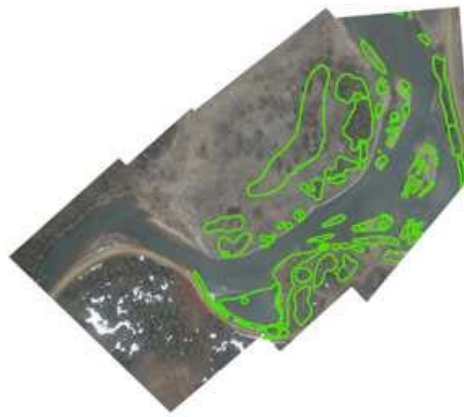
(b) NIR image.

Fig. 5.10: Sample pictures for river tracking.

measurement of the interested field. However, it is not always easy or inexpensive to collect all the data from remote data loggers for further processing. Many applications still require humans to get close to the ground-based sensors to retrieve the data from their data loggers. Wireless sensor networks and satellite networks are used in environmental data collection applications, but wireless communication can be expensive and vulnerable to changing environmental conditions (such as loss of line-of-sight due to vegetation growth). This problem is especially difficult when the sensors are deployed sparsely over a large geographic area where transportation might be limited by terrain conditions. UAVs can fly into such areas without affecting the vegetation on the ground; they can spare humans from having to enter dangerous or difficult areas; and they might be able to operate at lower costs that



(a) Substrate map.



(b) Vegetation map.

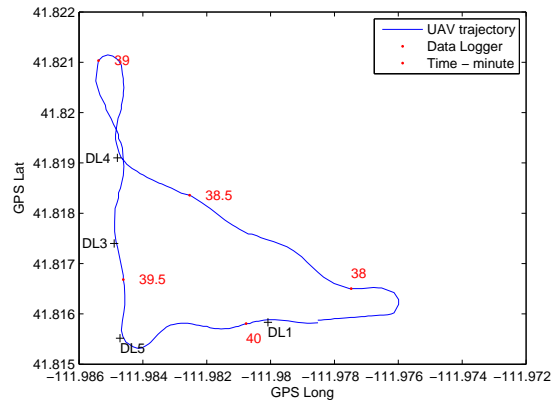
Fig. 5.11: Oneida Narrows imagery (courtesy of A. M. Jensen for image processing).

might be required for approaches involving direct human access to the data. Moreover, UAVs can achieve better wireless communication since the signal can be transmitted more dependably in the air than near ground level.

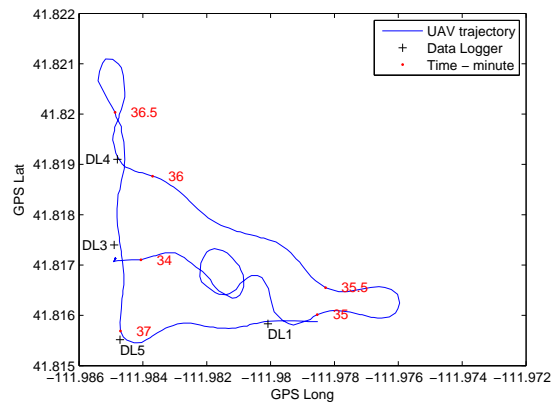
One preliminary experiment was performed to test the feasibility to use UAVs for remote data collection. The CR 206 data loggers from Campbell Scientific Inc. are used as both ground sensors and communication modules. The CR206 data logger is a small measurement and control unit with a 12-bit A/D converter, an on-board 915 MHz spread spectrum radio modem, and 512 kbytes memory [79]. It can transmit data to another logger with the communication range of about 300 meters on the ground. Four CR 206 data loggers

were sparsely spread out on a research farm with more than 300 meters between them, shown in Fig. 5.12. One CR206 data logger was mounted at the bottom of the UAV as a remote data collector, which scans every 15 seconds and sends data out if it detects another CR206. The preplanned path is to fly above all the four data loggers and circle around, as shown in Fig 5.12(a). The UAV will first start from take off point, climb to the desired height and begin following waypoints 1 – 2 – 3 – 4 – 5. The UAV will repeat this cycle 5 – 1 until the battery is exhausted. The flight height is set as 100 meters and the cruise speed for the UAV is set to 14 m./sec.. The UAV flight trajectory is plotted in Fig. 5.12(a) with time steps marked. The UAV has a data logging rate of 3Hz.

The UAV actually flew two rounds from 10:35:16 AM to 10:40:12 AM. The data receiver



(a) Trajectory 1st round.

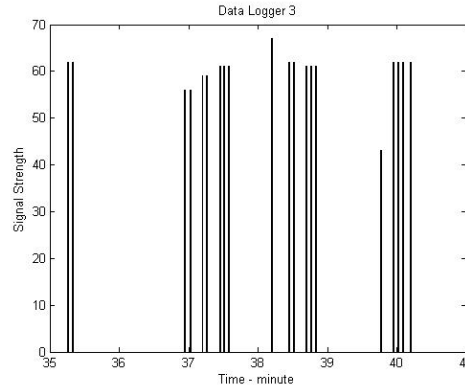


(b) Trajectory 2nd round.

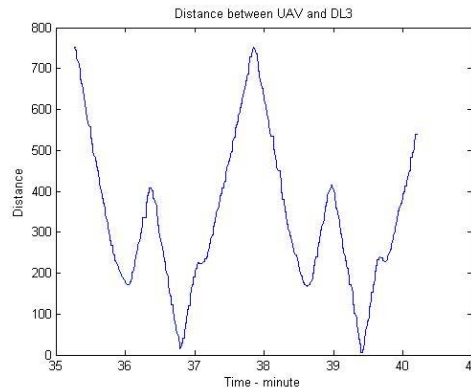
Fig. 5.12: UAV trajectory.

got no signal during the take-off period, which is from 10:34AM to 10:35:16 AM as shown in Fig. 5.12(a). Data collected from data logger 3 is analyzed in detail with the signal strength and the transmission distance shown in Fig. 5.13.

It is clear that the UAV can retrieve data given the UAV stays close to the ground station as shown in Fig. 5.13. But there are obvious some delays caused by the UAV flight speed. It is also observed that the signal strength can vary with the distance. The maximal distance to successfully retrieve data is as far as about 800 meters, about three times the range on the ground. However, it is also observed that the communication is highly affected



(a) Signal Strength from DL3.



(b) Distance between UAV and DL3.

Fig. 5.13: Further analysis of data logger 3.

by the height and the surroundings of the data logger. Data logger 4 is placed in the grass about two feet high, which results in bad communication. Data loggers 1 and 5 have a good communication because of their position above the ground. Further tests with a wider ground sensor distribution, as far as five miles, will be attempted. One more function, that of loitering or circling around the ground sensors, will also be added.

5.3.6 Other Applications

Another typical example of remote data collection is fish tracking. In order to understand fish habitats, radio transmitters are planted in fishes in order to locate and track their movements. Human operators are needed to drive a boat around a lake or down a river following the periodic beacon sent from the transmitters. The beacon is heard through a radio receiver with a directional antenna and its strength is highly dependent on the distance and the direction the antenna is pointed at. AggieAir could be employed here with an onboard self-designed device to catch the signal from the transmitter and record its strength. Thus, the location of the fish can be found and recorded much easier and faster since the wireless signal transmits much better in the air.

There are also many other potential applications for small UAV-based remote sensing. One is for thermal image applications. The sample thermal image taken on the ground is shown in Fig. 5.14. In fact, the white color on the picture means a high temperature while the black color means a low temperature. It can be observed that the vehicle had higher temperature than the human since the air conditioning was running.

5.4 Chapter Summary

This chapter characterizes the problem of using UAVs for remote sensing in water management and irrigation control applications, and provides an outline of a band reconfigurable solution to the problem. The big problem is divided into two subproblems: the path planning subproblem and the image georeferencing subproblem for separate solutions. Several representing experimental results show the effectiveness of the proposed solution.



Fig. 5.14: Sample thermal picture.

Chapter 6

Cooperative Remote Sensing Using Multiple Unmanned Vehicles

The limited power capacity of small UAVs create challenges while using UAVs for remote sensing missions of a large-scale system. This motivates the group use of small UAVs since the aerial image collection task can be finished in parallel on different small UAVs. For instance, some irrigation applications may require remote sensing of a land as big as 30 square miles within one hour. Acquisition of imagery on such a geographic scale is difficult for a single small UAV. Instead, groups of small UAVs can solve this problem because they can provide images in a shorter time even with more spectral bands since UAVs with configurable spectral bands can work in groups. Of course, the low costs make it possible to use small UAVs in large amounts for civilian applications.

Following the similar definition of the remote sensing problem in Chapter 5, the following missions will need multiple UAVs being operated cooperatively:

- Measure $\eta_1, \eta_2, \eta_3 \dots$ simultaneously. For example, images from multiple spectral bands can provide far more information and they are indispensable for applications like soil moisture estimation.
- Measure $\eta_i(q, t)$ within a short time. Some water applications may require images that are taken when the sunshine is the strongest. Small UAVs could work in groups for these kinds of missions to ensure the mission accomplishment within a short time.
- Measure the gradient in real-time. Applications like monitoring of a fast-evolving processes may require information like the gradient or flow rate in real-time. For instance, the gradient of the temperature and wind field in a forest fire scenario can greatly affect the prediction of the fire spread.

The above typical multi-UAV missions can be categorized into two groups: formation-based applications and non-formation-based ones. The consensus-based formation control algorithms are looked into carefully in this chapter with theoretical approaches and experimental validations on MASnet hardware simulation platform. The wind profiling measurement problems is also considered using small UAVs. Similar formation control techniques can be applied on UAVs for wind field measurement.

6.1 Consensus-Based Formation Control

The basic idea of consensus algorithm is to achieve a common state among groups of agents through multi-vehicle communications [80]. For example, the rendezvous mission requires all the agents to converge to a same position with no preknown agreements. The rendezvous mission is a base for other formation control tasks since the offset can be added to the rendezvous mission to achieve the axial alignment or formation control. The basics of the consensus algorithm and its implementation on our MASnet hardware simulation platform are introduced in this section. The motivation here is to apply this multi-vehicle consensus algorithm on real hardware platforms for the formation control.

6.1.1 Consensus Algorithms

Assume that the unmanned vehicles have single-integrator dynamics given by

$$\dot{\xi}_i = u_i, \quad i = 1, \dots, n, \quad (6.1)$$

where $\xi_i \in \mathbb{R}^m$ is the state of the i^{th} vehicle (e.g., position), and $u_i \in \mathbb{R}^m$ is the control input (e.g., velocity). The consensus algorithm is proposed as

$$u_i = - \sum_{j \in \mathcal{J}_i(t)} k_{ij}(t)(\xi_i - \xi_j), \quad i = 1, \dots, n, \quad (6.2)$$

where $\mathcal{J}_i(t)$ represents the set of vehicles sharing states with vehicle i at time t , and $k_{ij}(t)$ is a positive weighting factor at time t [80–84]. $\mathcal{J}_i(t)$ combined with $k_{ij}(t)$ can also be called

a Laplacian matrix $L(t) \in \mathbb{R}^{n \times n}$ in the graph theory. $L(t) = [\ell_{ij}(t)]$ is defined as follows:

$$\ell_{ij}(t) = \begin{cases} \sum_{j \in \mathcal{J}_i(t) \setminus \{i\}} k_{ij}(t), & \text{if } i = j; \\ 0, & \text{if } i \neq j, j \notin \mathcal{J}_i(t); \\ -k_{ij}(t), & \text{if } i \neq j, j \in \mathcal{J}_i(t) \setminus \{i\}. \end{cases} \quad (6.3)$$

For the control law described in (6.2), consensus is said to be reached asymptotically among the n vehicles if $\xi_i(t) \rightarrow \xi_j(t)$, $\forall i \neq j$, as $t \rightarrow \infty$ for all $\xi_i(0)$. The idea is to drive the states of all the n vehicles together through neighbor information sharing strategies. The Laplacian matrix or the communication matrix has to be a spanning tree to ensure the consensus [80].

The basic control strategy (6.3) can be extended for different formation control tasks. Instead of ensuring the convergence of $\xi_i(t) - \xi_j(t)$ to zero, an offset can be added here to achieve user specified formations. For example, an fixed offset δ on the x axis and the zero offset on the y axis can lead to the final axial alignment in a 2D space. The following algorithm is derived based upon (6.3):

$$u_i = \dot{\delta}_i - \sum_{j \in \mathcal{J}_i(t)} k_{ij}(t)[(\xi_i - \xi_j) - (\delta_i - \delta_j)], \quad i = 1, \dots, n, \quad (6.4)$$

where $\delta_i - \delta_j$, $\forall i \neq j$ represents the user specified separation [85]. The different choices of δ_ℓ , $\ell = 1, \dots, n$ can lead to different formation shapes.

6.1.2 Implementation of Consensus Algorithms

The above consensus algorithms (6.2) and (6.4) are for scenarios that the control input is the first order derivative of the system state. There are also cases that the system state can be controlled directly. Similar consensus algorithms can be derived as follows. Suppose the unmanned vehicles can only move in a 2D space. Let $r_i = [x_i, y_i]^T$ and $r_i^d = [x_i^d, y_i^d]^T$ denote, respectively, the actual and desired position of vehicle i . For rendezvous, the control

law is designed as

$$\dot{r}_i^d = - \sum_{j \in \mathcal{J}_i(t)} (r_i^d - r_j^d). \quad (6.5)$$

Another strategy is designed as

$$\dot{r}_i^d = - \sum_{j \in \mathcal{J}_i(t)} (r_i - r_j). \quad (6.6)$$

Both control laws could guarantee the $r_i^d(t) \rightarrow r_j^d(t)$ and $r_i(t) \rightarrow r_j(t)$, $\forall i \neq j$, asymptotically as $t \rightarrow \infty$ [85].

For axial alignment, the following algorithm is applied to update r_i^d as

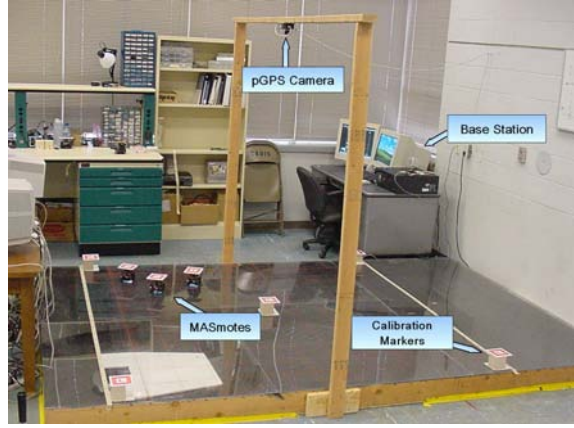
$$\dot{r}_i^d = - \sum_{j \in \mathcal{J}_i(t)} [(r_i - r_j) - (\delta_i - \delta_j)], \quad (6.7)$$

where $\delta_i = [\delta_{ix}, \delta_{iy}]^T$ could be specified for specific missions based on vehicle sizes.

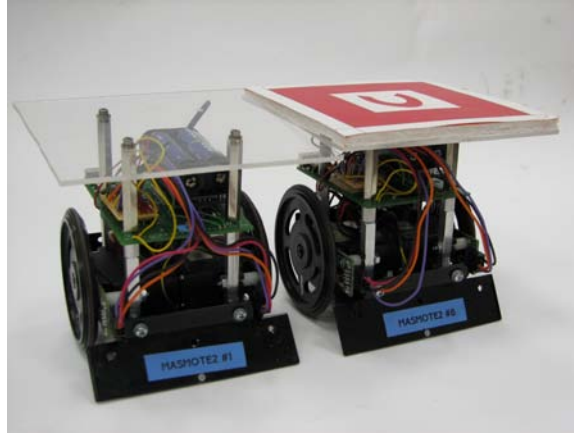
6.1.3 MASnet Hardware Platform

The Mobile Actuator and Sensor Network (MASnet) research platform in the Center for Self-Organizing and Intelligent Systems (CSOIS) at Utah State University combines wireless sensor networks with mobility [86]. In other words, the robots can serve both as actuators and sensors. Although each robot has limited sensing, computation, and communication ability, they can coordinate with each other as a team to achieve challenging cooperative control tasks such as formation keeping and environment monitoring.

The MASnet platform is comprised of MASmotes, an overhead USB camera, and a base station PC, shown in Fig. 6.1. MASmotes are actually two-wheel differentially steered robots that can carry sensors and actuators with MicaZ from Crossbow serving as the processor. Thus, MASmotes support inter-motes communication, sensor data collecting, pulse width modulation (PWM) signal generation. The overhead camera is used to determine each robot's position and orientation, called pseudo-GPS. Images are processed on the base PC, which also serves for serial to programming board communication and decision making.



(a) MASnet testbed.



(b) MASmote robot hardware.

Fig. 6.1: MASnet experimental platform.

The base station communicates with a gateway mote mounted on a programming board by serial link. The gateway mote then communicates with the MASmotes over a 2.4 GHz wireless mesh network. Through communication the base station can send commands and pseudo-GPS information to each MASmote. All the MASmotes can also communicate with each other over the 2.4 GHz wireless mesh network.

The MASmote has a low-level PID controller to achieve an accurate position control, that is, r_i tracks r_i^d . So the specific control input for our MASmote are desired positions of

robots: r_i^d . The consensus algorithm is implemented as below:

$$r_i^d = \frac{\sum_{j=1}^N g_{ij} r_j}{\sum_{j=1}^N g_{ij}}, \quad (6.8)$$

where g_{ij} is the element from the communication matrix.

6.1.4 Experimental Results

Several consensus algorithms have been tested on the MASnet hardware simulation platforms including rendezvous, axial alignment, and V formation all with different communication topologies.

Rendezvous

Rendezvous is the basic for the consensus-based formation control. The key point is to achieve the convergence through constant communications. However, different communication topologies may affect the final convergence time and location. Three typical communication topologies were tested including the neighbor case (Case I), the isolated case (Case II), and the directed communication case (Case III), shown in Fig. 6.2. From the experimental results shown in Fig. 6.3, it can be seen that Case I achieves the rendezvous in the shortest time (11.58 sec.) because of more information sharing while Case II take a little longer time (18.89 sec.) and Case III can only achieve the local convergence.

Besides the fixed communication topologies, the switching ones were also tested on our hardware platform. One typical example is to compare one connected topology with

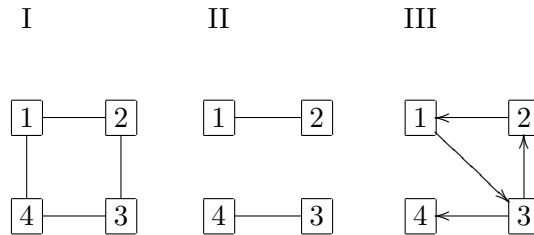


Fig. 6.2: Communication topologies for the rendezvous experiment.

(a) Case I ($t_f = 11.58$ sec.).(b) Case II ($t_f = 6.93$ sec.).(c) Case III ($t_f = 18.89$ sec.).

Fig. 6.3: Experimental results of rendezvous for Cases I-III.

its partial members. Communication topology \mathcal{G}_u is decomposed into five partial members \mathcal{G}_1 - \mathcal{G}_5 , as shown in Fig. 6.4. The robot trajectories are shown in Fig. 6.5. It can be observed that both cases could arrive the final rendezvous, but they will perform differently while converging.

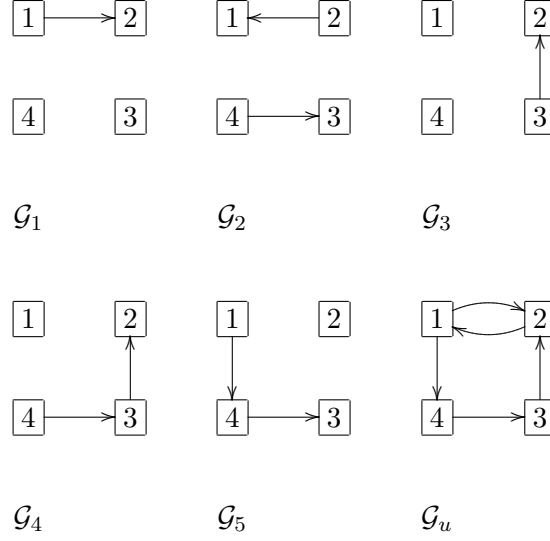


Fig. 6.4: Switching information topologies \mathcal{G}_1 - \mathcal{G}_5 and their union \mathcal{G}_u for rendezvous.



(a) Rendezvous with topologies randomly switching from $\bar{\mathcal{G}}_s = \{\mathcal{G}_1, \dots, \mathcal{G}_5\}$ ($t_f = 45$ sec.). (b) Rendezvous with a time-invariant topology \mathcal{G}_u ($t_f = 24$ sec.).

Fig. 6.5: Experimental results of rendezvous with topologies randomly switched from $\bar{\mathcal{G}}_s$ versus a time-invariant topology \mathcal{G}_u .

Axial Alignment

Axial alignment is essentially alignment along one axis of interest and in the two-dimensional case it can be demonstrated by aligning along one dimension. In order to avoid collisions in this process, the experiment involved alignment along the y axis with an offset alignment along the x axis. By giving an desired offset from the center to the robots on the ends of the group, the line is spread evenly with spaces twice the distance of the offset. This simple mechanism achieves a relatively simple method of collision avoidance and also shows another attribute of the consensus algorithm. The communication topology is shown in Fig. 6.6 and the robot trajectories are shown in Fig. 6.7. The desired offset from the center for the outside robots is 20 cm which gives a separation distance of 40 cm between all robots in the group along the x axis. It can be observed that the robots can achieve the axial alignment mission with the consensus algorithm.



Fig. 6.6: Undirected interaction topology for axial alignment.



Fig. 6.7: Experimental result of axial alignment.

V Formation

The “V” formation control employs an extension of the offset idea. By setting an offset to the following members of the group, the group stays in a “V” formation with proper spacing. The spacing desired here, like the axial alignment experiment, is 40 cm in the y axis and also 40 cm in the x axis. This gives a separation of about 56.5 cm along the edge of the formation between any two robots. The communication flows in a leader-follower structure down through the group, shown in Fig. 6.8. The robot trajectories are shown in Fig. 6.9.

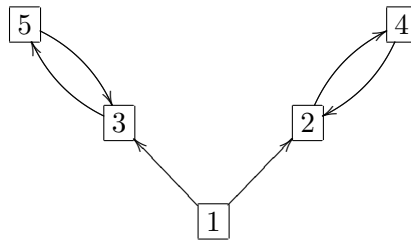


Fig. 6.8: Information exchange topology for formation maneuvering.

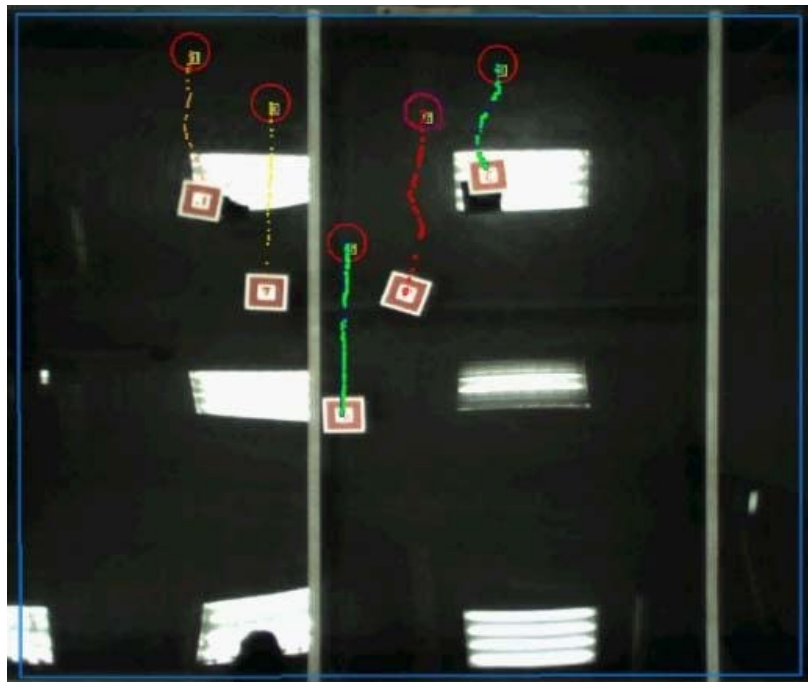


Fig. 6.9: Experimental result of formation maneuvering.

Due to the inherent limitations of the robots and the packet loss during vision problems from the pseudo GPS updates, formation moves on the MAS-net platform are difficult. However, the formation is achieved through the move and stays in a general “V” shape throughout the move. This shows the robustness of the consensus algorithm and its ability to keep the group goal achieved even when motion as a particular formation is required.

6.2 Surface Wind Profile Measurement Using Multiple UAVs

Winds in the atmospheric boundary layer (ABL) play an important role in human life because their flow cause the movements of heat, vapor, pollutants, and other airborne particles. Especially, processes like forest fire spreading [87], gas leaking, pollution dispersion, or heat/vapor transfers are highly affected by the distribution of wind field. Surface winds are defined as flows less than 1km above the ground. They could also be used to generate electricity [88]. To fully use the wind energy and accurately predict the dynamic changes of such diffusion/transfer processes, high resolution and real-time wind field measurements are demanded. Traditional wind profiling techniques like balloons, meteorological towers are not only expensive but also inflexible. In particular, for circumstances like forest fires, it is almost impossible to have an accurate prediction for the local wind field based on data from weather stations due to its immobility and geographical sparse distribution [89]. Because of both temporal and spatial variations, it is hard to measure the wind field precisely in the meso or micro-scale.

UAVs could be utilized as mobile platforms capable of carrying sensors in the 3D space [68]. Nowadays, technological advances in wireless networks and micro electromechanical systems (MEMS) make it possible to mount small, light weight, and inexpensive sensors on UAVs to measure the pressure, temperature, humidity, and wind speed in real-time [2]. The advantages of using UAVs to measure the wind field include [17]:

- Real Time: UAVs provide real-time data to time critical situations like pollutant diffusion, forest fire forecasting, combat urban environmental prediction, or chemical leaking;

- High Resolution: UAVs could get high resolution micro scale data without relying on the weather station. UAVs can be employed in all kinds of terrains;
- Low Cost: The developments of small UAVs make it affordable for its applications in meteorology;
- More Flexibility: UAVs could be easier to use compared with manned aircraft measurements since no human pilots will be endangered for such tedious measurement works;
- More Data: Multiple-UAV solution instead of only one. Easy for gradient-based searching and gradient information acquisition.

Many researchers already looked into the problem of using multiple robots for the environmental monitoring problem. A model-free robot path planning algorithm is introduced for the coverage control problem of a density field [14]. The adaptive and singular value-based sampling algorithms are proposed for the ocean field sampling problem [90,91]. However, most of reported efforts focus on the density field instead of a more complex vector field. Rotary wing UAVs are also used for heat flux estimation with user customized pressure sensing unit [92]. To achieve the optimal measurement of the wind field, groups of UAVs could fly in formations for faster estimation [93].

In this dissertation, small UAVs are defined as UAVs with the weight less than 55 lbs [19]. They are mostly used for intelligence, surveillance, and reconnaissance missions in the troposphere, which is the part of the atmosphere about fifteen kilometers above the ground [94]. The lowest part of the troposphere is planetary boundary layer (PBL). The winds in the PBL, also called the surface winds, are highly affected by the Earth's surface and in turn play important roles in weather predictions. Researchers have used aircrafts to aid the measurements in the meteorology [95]. However, UAVs are still seldomly used for such meteorology missions. Typical small UAV platforms are able to fly in winds less than 20 m./sec. [68,96,97]. After the specific design and tests, small UAVs can even be deployed for very dangerous tornado tracking missions since no human pilots are required onboard.

Small UAVs can make real-time measurements of the wind, temperature, pressure, humidity in points in a 3D space of the troposphere. The wind information is actually estimated based on the measurements of the relative airspeed and the absolute GPS speed of small UAVs. For instance, the horizontal wind estimation error of Kestrel autopilot can be as small as 5% on speed and 2% on heading [98]. There are also special pressure devices made for small rotary-wing UAVs to measure the vertical wind speed [92]. This information could be used to estimate the heat flux in the agricultural fields. There are a lot of potential wind applications for small UAVs including real-time wind profile mapping, forest fire prediction, fog diffusion prediction, etc.

6.2.1 Problem Definition: Wind Profile Measurement

For common weather prediction problems, the synoptic wind field in the horizon order of 1000km is considered. However, UAVs are more suitable for mesoscale or microscale wind field measurement. The mesoscale field is defined with the horizon length between several kilometers to several hundred kilometers while the microscale is as small as 1km or less. The 2D meso or micro scale wind field measurement problem is focused in this chapter. Assuming a near surface wind field of interest by $V = (v_e, v_n)^T$, the vorticity ξ and divergence δ are defined as follows [99, 100]:

$$\xi = k \cdot \nabla \times V, \quad (6.9)$$

$$\delta = \nabla \cdot V, \quad (6.10)$$

where k is the unit vector in z axis.

Without loss of generality, V could be decomposed into two vectors: a nondivergent one and a curl free one.

$$V = k \times \nabla \psi + \nabla \chi, \quad (6.11)$$

where

$$\begin{cases} \nabla \cdot (k \times \nabla \psi) = 0, \\ \nabla \times (\nabla \chi) = 0. \end{cases}$$

We have the following assumptions to guarantee a unique solution for the above equations [99]:

- At the boundary, χ is assumed to be $\chi = 0$;
- At the boundary, p is assumed to be bounded and have higher order derivatives;
- ψ is assumed to be linear with respect to the pressure field in the area of interest;
- Assume that the ξ and δ could be approximated by low-order polynomials.

The Poisson equations could be derived from (6.11).

$$\nabla^2 \psi = \xi, \quad (6.12)$$

$$\nabla^2 \chi = \delta, \quad (6.13)$$

$$v_e = -\frac{\partial p}{\partial y} + \frac{\partial \chi}{\partial x}, \quad (6.14)$$

$$v_n = \frac{\partial p}{\partial x} + \frac{\partial \chi}{\partial y}, \quad (6.15)$$

where ξ and δ have the following forms:

$$\xi(x, y) = \sum_{m=0}^{M_c} \sum_{n=0}^{M_c} c_{m,n} x^m y^n \quad \text{for } m+n \leq M_c, \quad (6.16)$$

$$\delta(x, y) = \sum_{m=0}^{M_c} \sum_{n=0}^{M_c} d_{m,n} x^m y^n \quad \text{for } m+n \leq M_c. \quad (6.17)$$

A typical meso/micro-scale wind field (about 10×10 km) is shown in Fig. 6.10 with 280 meters resolution at 100 meters high. The example wind field is generated by WindStation simulation software [101]. It can be seen in Fig. 6.10 that the wind field is greatly affected by the complex mountain terrain.

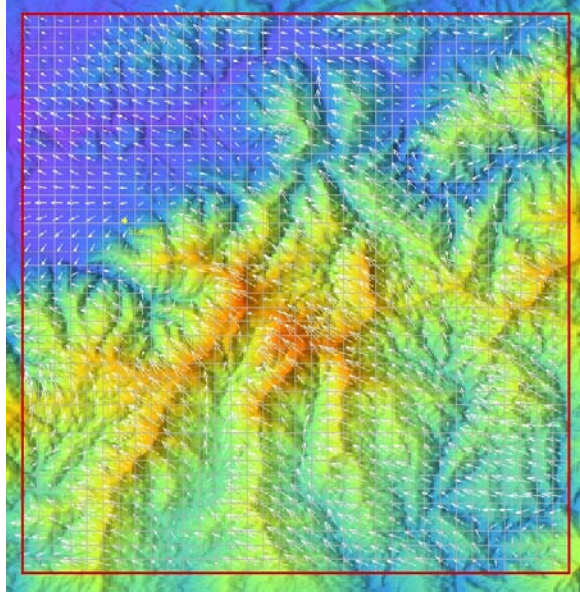


Fig. 6.10: A random wind field.

Numerical Solution for Parameter Identification

Assuming that the wind field in the whole area of interest can be measured, a numerical solution can then be derived [102]. Given an area with $M \times N$ equally spaced grids with spacing h , the measurements of the velocity at all the points form two vectors ($VN_{MN \times 1}$ $VE_{MN \times 1}$).

$$\begin{bmatrix} VN \\ VE \end{bmatrix} = F\hat{W}, \quad (6.18)$$

where \hat{W} is the vector containing all the unknown parameters and pressure field boundary conditions; F is determined from the corresponding governing difference equations. Then,

$$\hat{W} = (F^T F)^{-1} F^T \begin{bmatrix} VN \\ VE \end{bmatrix}. \quad (6.19)$$

The objective function of the wind profile measurement could be defined as:

$$\min. \sum_{i=1}^{MN} [(V_i - \hat{V}_i)(V_i - \hat{V}_i)^T], \quad (6.20)$$

where \hat{V} is the estimate of the wind field from the identified parameters \hat{W} .

6.2.2 Wind Profile Measurement Using UAVs

UAV could serve as a new measurement platform for the surface wind field because UAVs could be easily commanded to any 3D point in the atmospheric boundary layer, which is a hard mission for meteorological stations. Common micro sensors like temperature, humidity, pressure, and wind speed are now very cheap to be mounted on the UAVs. Recently, it is even possible to employ multiple small UAVs to form a team to measure the horizontal or vertical profile simultaneously which can offer big advantages for later gradient detections.

The most intuitive way of using a single UAV for wind profile measurement is to map the wind field first and then analyze the model off-line. Assume that the area of interest is rectangular ($utm_e \in [x_1, x_2]$, $utm_n \in [y_1, y_2]$), the desired resolution is h m. The UAV is assumed to be able to fly at a certain preplanned altitude with the cruising speed v_c and a minimal turning radius $R_{min} < h$. In other words, the UAV could either follow a straight line or follow a circle with radius greater than R_{min} . Sensor readings including the temperature, pressure, wind speed, and GPS position are sent to the ground station at f Hz in real-time. The UAV trajectory could be planned following the algorithm described in Chapter 5. The sweep distance is h and the sensor data collected while turning is neglected for the consistency in spatial resolution of the collected data.

The similar numerical method could be used for the wind field parameter identifications after collecting all the wind data. However, this method is time consuming and especially not efficient for relatively simple wind fields. In fact, the model identification accuracy could be used as a feedback to guide the UAV to an information richer area instead of following the preplanned trajectories without knowing the specifics of the local wind field.

The objective function of the wind profile measurement incrementally using UAVs could be defined as:

$$\min. \quad E[(V_k - \hat{V}_k)(V_k - \hat{V}_k)^T], \quad (6.21)$$

where V_k is the real wind measurement at time k and \hat{V}_k is the estimate of the wind field based on the historic data from $t = 0, \dots, k$.

The difference of the above problem with the numerical off-line solution is that the UAV needs to be guided based on the estimation errors. To solve this problem, we propose the following scheme.

Initial Estimation of Prevailing Wind

The prevailing wind is also called longitudinal wind, which is the wind prediction estimated from larger scale like synoptic scale. It is the prevailing direction at the predicted height without considering the surface frictions and complex terrains. The idea here is to send the UAV to measure the wind speed and estimate the noise level at the same time. In this way, the UAV does not have to visit all the grids.

Assume the wind field could be modeled as

$$\begin{aligned} u &= \bar{u} + \xi_u, \\ v &= \bar{v} + \xi_v, \end{aligned} \quad (6.22)$$

where $\bar{u} + \bar{v}$ is called the constant longitudinal wind and $\xi_u \sim N(0, \sigma_u)$ and $\xi_v \sim N(0, \sigma_v)$ are white noises. The parameters of the prevailing wind model could be identified by Kalman filter described as below:

$$\begin{aligned} vx_k^- &= vx_{k-1} + \xi_{vx}, \\ vy_k^- &= vy_{k-1} + \xi_{vy}, \end{aligned} \quad (6.23)$$

$$\begin{aligned} vx_k &= vx_k^-, \\ vy_k &= vy_k^-. \end{aligned} \tag{6.24}$$

Recursive Parameter Estimation Using UAVs

With the real-time sensor data coming in, the local wind field model can be derived. The estimated model is then compared for each small division. The UAV will be sent to the area with the biggest difference compared with the identified model (the gradient direction).

$$\begin{bmatrix} VN \\ VE \end{bmatrix} = \nabla e. \tag{6.25}$$

Optimal Wind Profile Measurement Procedures

The path planning algorithm using a single UAV for optimal wind profile measurement can be described as follows:

- (1) Launch the UAV and send it into the desired area and altitude for survey;
- (2) Using Kalman filter to make an initial guess of the wind model, or the prevailing wind speed \bar{u} and covariances;
- (3) If $\text{mod}(k, l) == 0$, estimate the wind field model based upon the collected wind data, where l is the preset time interval to trigger the wind model prediction;
- (4) If $\sum_{i=k}^{k+l} |E_i - \hat{E}_i| > \sigma l$, go to Step 5. Otherwise, go to Step 6. σ is the max tolerance of the model errors;
- (5) Follow the flight direction from (6.25), go back to Step 3;
- (6) Follow the preplanned flight path, go back to Step 3.

6.2.3 Wind Profile Measurement Using Multiple UAVs

The intuitive way of using multiple UAVs in wind profile measurement is to divide the interested domain into small regions for every single UAV. However, one advantage here of

using UAV formation flight is the real-time estimation of the pressure derivative $(\frac{\partial p}{\partial x}, \frac{\partial p}{\partial y})$. Assuming that four UAVs collect data while maintaining a simplex shape with h distances, $\frac{\partial p}{\partial x}$, $\frac{\partial p}{\partial y}$, and $\frac{\partial p}{\partial z}$ can then be measured in real-time, which in turn can reduce the computation time for the later parameter estimations. The simplex formation is shown in Fig. 6.11.

The formation shape could also be changed based on different resolution requirements. For example, a closer formation is needed for areas with turbulence while a formation of larger separation is chosen for prevailing wind dominant areas. The UAV distance could also be determined by the resolution requirements.

6.2.4 Preliminary Simulation and Experimental Results

The preliminary simulation and experimental results are provided in this section, focusing on the simple wind field model.

Simulation Results

To simplify the problem, a simple wind field is considered first, which can be modeled

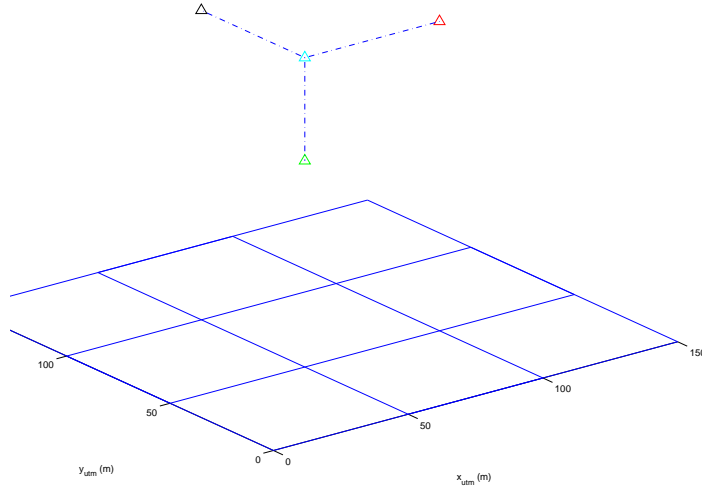


Fig. 6.11: UAVs flying in a simplex formation.

by (6.22). This model is generally true for most open areas with no sudden wind changes in several hours. The target wind field is a rectangular area about $3 \text{ km} \times 3 \text{ km}$. The nominal wind speed is 5 m./sec. and the nominal wind direction is 30 degrees (relative to the north). The UAV wind estimations are corrupted with the measurement noise $\xi_u \sim N(0, 1)$ and $\xi_v \sim N(0, 1)$, shown in Fig. 6.12.

A single UAV is sent out for this mission following trajectories planned based on the method described in Chapter 5. The UAV is assumed to fly at 15 m./sec. and report wind measurements every 3.3 sec. to the ground control station (GCS). The proposed Kalman filter algorithm is running on the GCS for the real-time wind field estimation. The error covariances are estimated through real measurements. The estimation results of the east wind (\bar{u}) and north wind (\bar{v}) are shown in Fig. 6.13 and Fig. 6.14, respectively. It can be observed that the nominal wind can be accurately estimated after several minutes duration of flight.

The nominal wind estimation algorithm can also be used as an initial guess for a more

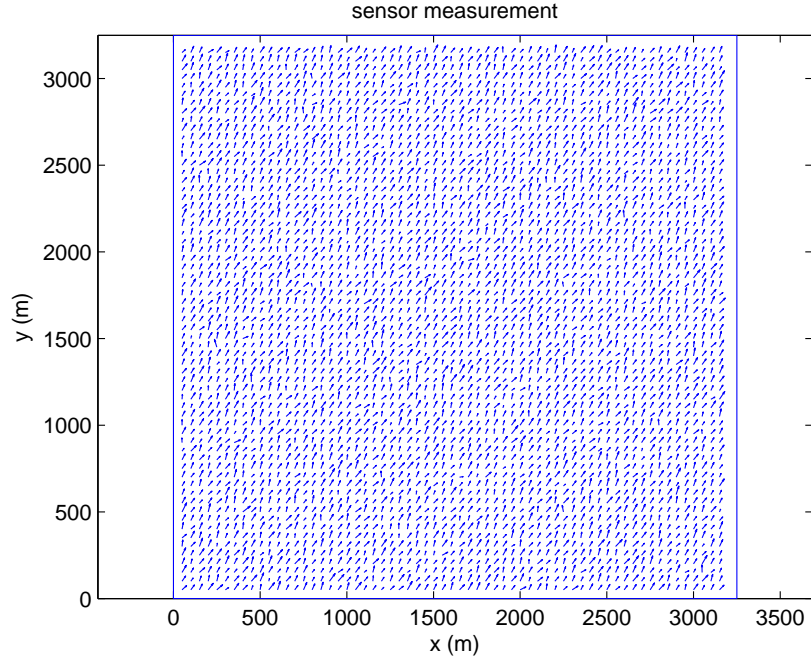


Fig. 6.12: Wind measurement (simulation).

complex wind field. The UAV could be sent to fly at the flat area first to get an estimation of the prevailing wind and then be deployed to complex terrains for further wind model estimation, which is left as future work.

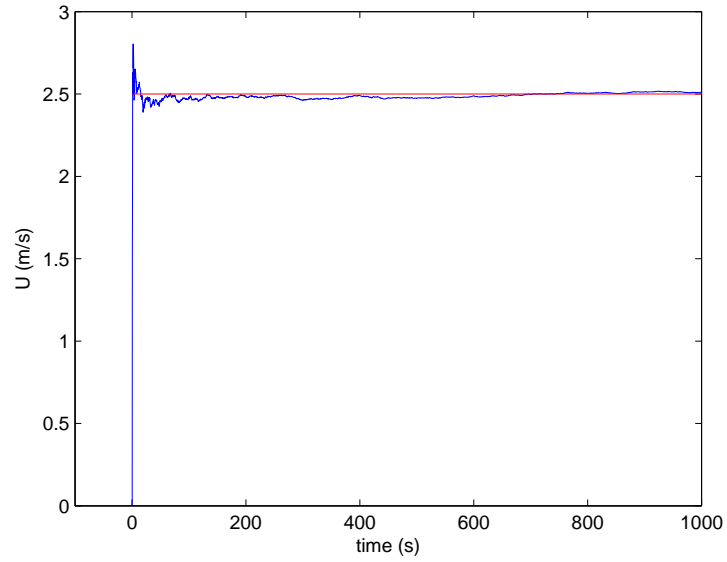


Fig. 6.13: Estimation of wind speed \bar{u} .

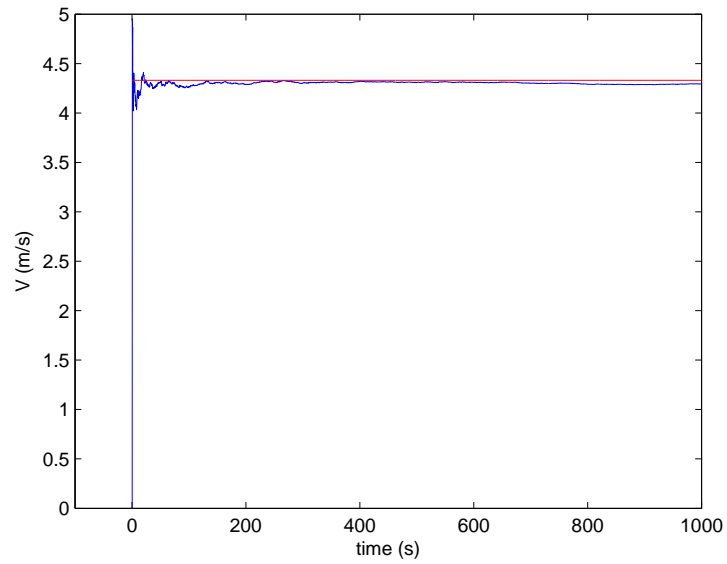


Fig. 6.14: Estimation of wind speed \bar{v} .

Experimental Results

The wind estimation data collected during the flight of a single UAV are used in this section to test the nominal wind estimation algorithm.

Tiger UAV Platform Introduction: AggieAir-Tiger UAV is used as the experimental platform for the wind data collection [69]. It is a flying-wing UAV with a 72" wing span called Tiger, with the image shown in Chapter 2. The weight of Tiger UAV is about 8 pounds including batteries, GPS, modem, autopilot, motors, and sensors. Open source Paparazzi TWOG autopilot board is used as the autopilot hardware [23] with Microstrain GX2 IMU and u-blox LEA-5H GPS unit for inertial measurement. The specifications of AggieAir-Tiger UAV are described in Table 6.1. All the sensor readings are sent to the ground control station (GCS) through a 900 MHz serial modem in real-time. The wind is estimated on the ground control station with the UAV flight trajectory, the GPS speed, and the throttle percentage [23].

Preliminary Results: The flight data was collected at the Cache Junction research farm of Utah State University from 9:54 to 10:27 AM on May 31th, 2009. The Tiger UAV was used to collect data at 90 meters above the ground. The UAV flight trajectory and the estimated wind data are shown in Fig. 6.15. The UAV was first sent into a circle to gain the specified altitude. Then it started to follow the survey of a rectangular field. The cruise speed is set as 15 m./sec. and the wind is estimated every ten seconds.

Table 6.1: AggieAir UAS specifications.

	Specifications
Flight Time	≤ 1 hour
Cruise Sped	15 \sim 20 m./sec.
Flight Altitude	≤ 1000 m. (AGL)
Available Sensors	Temperature/pressure/air speed
Navigation Sensors	GPS/IMU

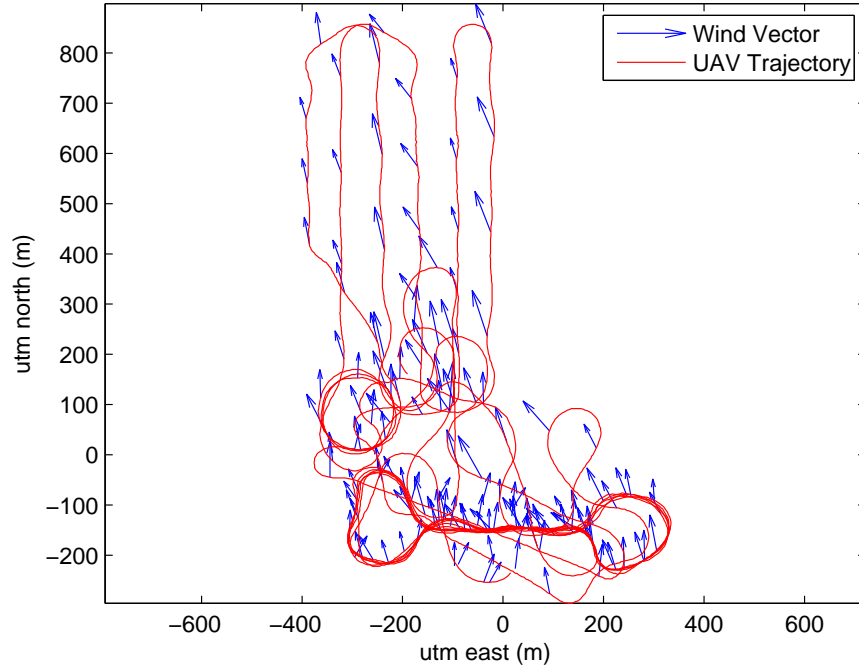


Fig. 6.15: Example wind field measured by AggieAir UAV.

Since the research farm is relatively flat, the prevailing wind can be estimated using the proposed algorithms, shown in Fig. 6.16 and Fig. 6.17. It can be seen that the north wind estimation converges after 10 minutes flight, shown in Fig. 6.17. Unfortunately, there are no other wind measurement techniques available for validations. One possible solution is to use multiple UAVs to see if they could achieve a consensus over the wind data.

Future Work: The simulation and experimental results in this chapter mainly focus on the estimation of the prevailing wind. It is only the first step to accurately model a micro-scale wind field. More efforts are needed for a more general wind field estimation problem including:

- More accurate wind estimation techniques. The current estimation algorithm for Paparazzi UAV platform is not accurate and is not calibrated. Further efforts are needed for accurate wind estimation using small UAVs;

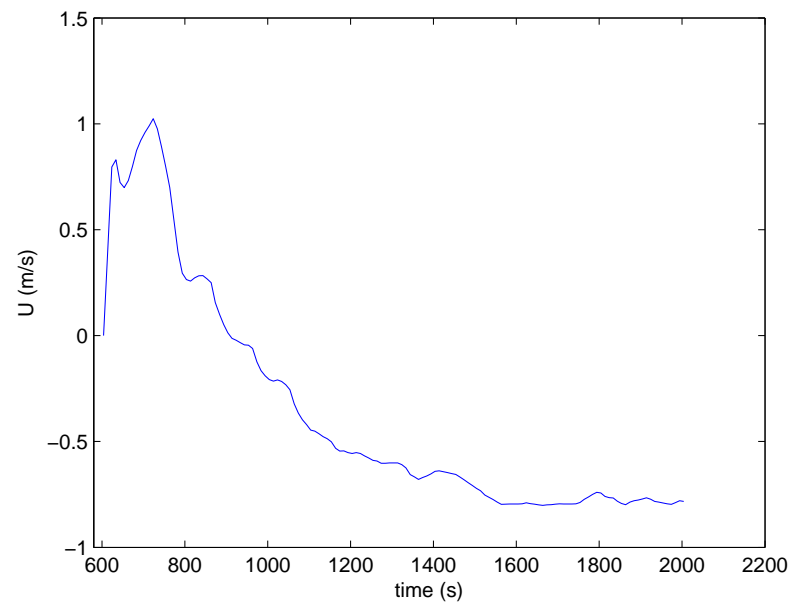


Fig. 6.16: Estimation of wind speed U .

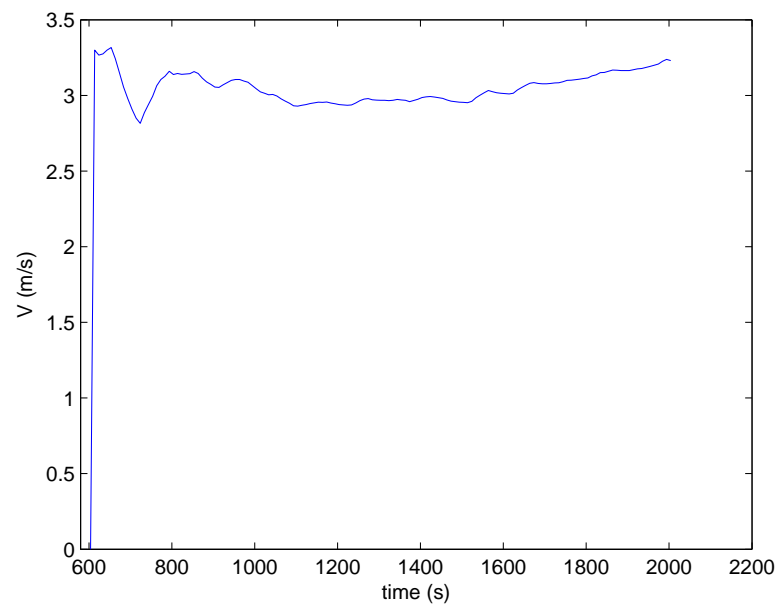


Fig. 6.17: Estimation of wind speed V .

- More wind information to measure. Except for horizontal winds, vertical winds are also very important especially to the heat, vapor transportation problems. Air speed

and pressure sensors can also be installed on vertical take-off and landing (VTOL) UAVs for more wind information following specific flight patterns;

- Further theoretical analysis for the complex wind field model. The wind fields in the complex domain like mountain and urban areas are highly dynamic and hard to measure. However, wind fields in these areas could have huge impacts on the problems like fire evolution. A more general wind model is indispensable for such missions.

6.3 Chapter Summary

The remote sensing problem using multiple UAVs are looked into in this chapter. Firstly, the multi-vehicle consensus algorithm is tested on the indoor MASnet robotics platform with different communication topologies and different missions. Then the wind profiling measurement problem is focused. A new path planning algorithm for wind field measurement is proposed using single or multiple UAVs. Preliminary simulation and flight results showed the potential of the algorithm.

Chapter 7

Diffusion Control Using Mobile Sensor and Actuator Networks

7.1 Motivation and Background

Diffusion processes like chemical/radiation leaks, oil spills can have a large impact on human health and natural environment. Nowadays, technological advances in networking and MEMS (Micro-Electro-Mechanical Systems) make it possible to employ a large number of mobile/static sensors/actuators to observe the diffusion, locate the source, and even counter-react with the harmful pollutants when a mobile sprayer network is used. In the past decade, many researchers looked into this topic. A swarm of mobile robots are used to detect chemical plume source with gradient climbing [103]; a moving diffusion source can be identified based on the parameter estimation algorithm [104]; boundary estimation and following problems are considered [105]. However, only the source information is not enough for controlling a diffusion process. Centroidal Voronoi tessellations are introduced in coverage control of a static gradient field with mobile sensor networks [14, 106, 107] and extended to a diffusing and spaying scenario [108].

Actually, the monitoring and control of a diffusion process can be viewed as an optimal sensor/actuator placement problem in a distributed system [11]. Basically, a series of desired actuator positions are generated based on centroidal Voronoi tessellations and integrated with PID controllers for neutralizing control based on Voronoi partitions. CVT algorithm provides a non-model-based method for coverage control and diffusion control using groups of vehicles. The CVT algorithm is robust and scalable [13, 109] and it can guarantee the groups asymptotically converging to the affected area even in multiple/mobile sources application [14].

Consensus is a common agreement reached by a group as a whole. The consensus can be made on robot formation, source location tracking, task assignment, and traffic control [81, 82, 85]. Although a group of mobile actuators are used for the diffusion control [108], the communication and information aspects are not taken care of. The mobile actuator only negotiates with its neighboring sensors, not neighboring actuators/sprayers, on how much to spray and where to go. As will be known in this chapter, the information sharing and interaction among neighboring actuators/sprayers in a group can have a large impact on the coordinated movements of these actuators and the resulted control performance consequently. Since the actuators are sent out for the same task, consensus is needed on both where to spray and how much to spray. The mobile actuators need to get close to the polluted area but it is not efficient to cluster, or running together densely. On the other hand, the neutralizer spraying should also be balanced since the best energy saving way is to maximize the neutralizing ability of every actuator. A new consensus algorithm is introduced and integrated into the CVT algorithm to guarantee the actuator group to converge faster towards the affected area with an improved control performance.

This chapter is organized as follows. In Sec. 7.2, the diffusion process is modeled by a PDE equation and the diffusion control problem is formulated. In Sec. 7.3, centroidal Voronoi tessellations-based optimal actuator location algorithm is briefly introduced. Section 7.4 is devoted to introducing the information consensus into the CVT-based optimal actuator location algorithm. Finally, simulation results and comparisons with the plain CVT algorithm are presented Sec. 7.5.

7.2 Mathematical Modeling and Problem Formulation

In this section, the PDE mathematical model of a diffusion process is introduced and the neutralizing control problem is then formulated.

Suppose a diffusion process evolves in a convex polytope Ω : $\Omega \in \mathcal{R}^2$. $\rho(x, y) : \Omega \rightarrow \mathcal{R}_+$ is used to represent the pollutant concentration over Ω . The dynamic process can be

modeled with the following partial differential equation (PDE):

$$\frac{\partial \rho}{\partial t} = k \left(\frac{\partial^2 \rho}{\partial x^2} + \frac{\partial^2 \rho}{\partial y^2} \right) + f_d(x, y, t) + f_c(\tilde{\rho}, x, y, t), \quad (7.1)$$

where k is a positive constant representing the diffusing rate; $f_d(x, y, t)$ shows the pollution source; $\tilde{\rho}$ is the measured sensor data; $f_c(\tilde{\rho}, x, y, t)$ is the control input applied to the system which represents the effect of neutralizing chemicals sent out by mobile actuators to counteract the pollutants. An example PDE system is shown in Fig. 7.1.

Assume n mobile actuators are sent to the field $f_c = f_{c_1} + \dots + f_{c_n}$. $P = (p_1, \dots, p_n)$ represent the locations of n actuators, $|\cdot|$ is the Euclidean distance. n actuators partition

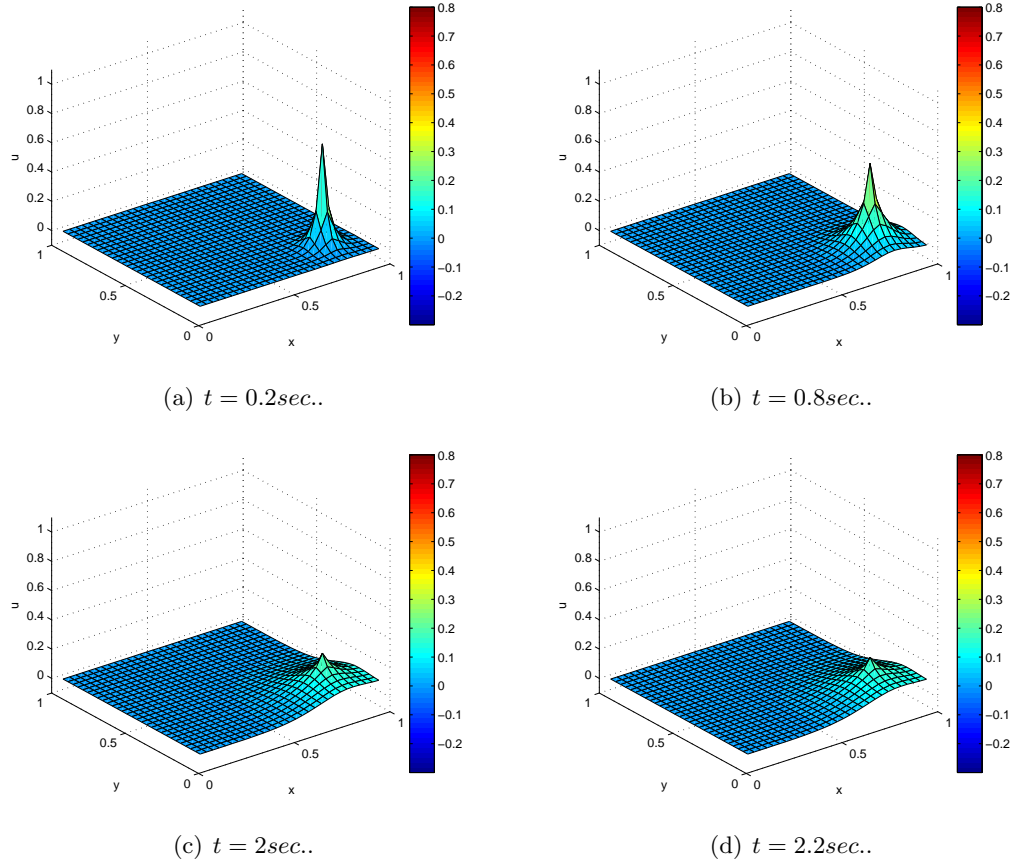


Fig. 7.1: Surf plot of a diffusion process modeled by (7.1): $k = 0.01$, $f_c = 0$, $f_d = f_d(0.8, 0.2, 20e^{-t})$.

Ω into a collection of n Voronoi Diagrams $\mathcal{V} = \{V_1, \dots, V_n\}$, $p_i \in V_i$, $V_i \cap V_j = \emptyset$ for $i \neq j$.

$$V_i = \{q \in \Omega \mid |q - z_i| < |q - z_j| \text{ for } j = 1, \dots, n, j \neq i\} \quad (7.2)$$

The control objectives are:

- Control the diffusion of the pollution to a limited area,
- Neutralize the pollution as quickly as possible without making the area of interest overdosed.

To achieve the above requirements, the following evaluation equation needs to be minimized [14, 108]:

$$\begin{aligned} \min. \mathcal{K}(P, \mathcal{V}) &= \sum_{i=1}^n \int_{V_i} \rho(q) |q - p_i|^2 dq \text{ for } q \in \Omega, \\ s.t. \quad |\dot{p}_i| &< k_v, |\ddot{p}_i| < k_a, \sum_{i=1}^n \int u_{spray_i}(t) dt < k_s, \end{aligned} \quad (7.3)$$

where \dot{p}_i and \ddot{p}_i represent the first and second order dynamics of the actuator and $u_{spray_i}(t)$ is the neutralizing control input of the actuator i at time t .

Define the mass and centroid of region V_i as

$$\begin{aligned} M_{V_i} &= \int_{V_i} \rho(q) dq, \\ \bar{p}_i &= \frac{\int_{V_i} q \rho(q) dq}{\int_{V_i} \rho(q) dq}. \end{aligned}$$

To minimize \mathcal{K} , the distance $|q - p_i|$ should be small when the pollution concentration $\rho(q)$ is high. But it is not an efficient strategy to drive all actuators very close to the pollution source, because the diffused pollutants far away from the source need also be neutralized quickly to minimize (7.3). A necessary condition to minimize \mathcal{K} for coverage control in a static gradient field is that $\{p_i, V_i\}_{i=1}^n$ is a centroidal Voronoi tessellation of Ω [14].

$$\frac{\partial \mathcal{K}}{\partial p_i} = 2M_{V_i}(p_i - \bar{p}_i) \quad (7.4)$$

The CVT algorithm is further extended to a dynamical diffusion process [108]. It is based on a discrete version of (7.3) and the concentration information comes from the measurements of the static, low-cost mesh sensors. The diffusion control problem is converted to two subproblems: location optimization (where to go for actuators) and neutralizing control (how much to spray).

7.3 CVT-Based Dynamical Actuator Motion Scheduling Algorithm

In this section, CVT-based actuator motion planning algorithm is discussed in details.

The classic Lloyd's algorithm [107,110] is an iterative algorithm to generate a centroidal Voronoi diagram from any set of generating points. It is modified to achieve coverage control [14] and diffusion control [108].

7.3.1 Motion Planning for Actuators with The First Order Dynamics

Assume that the sensors can be modeled by a first-order dynamical equation:

$$\dot{p}_i = u_i. \quad (7.5)$$

To minimize \mathcal{K} in (7.3), the control input is set to be:

$$u_i = -k_p(p_i - \bar{p}_i), \quad (7.6)$$

where k_p is a positive gain and \bar{p}_i is the mass centroid of V_i . \bar{p}_i is time-variant with diffusing.

7.3.2 Motion Planning for Actuators with The Second Order Dynamics

If the second-order dynamical sensor model is used, similarly we have:

$$\ddot{p}_i = u_i. \quad (7.7)$$

To minimize \mathcal{K} in (7.3), the control input is set to be:

$$u_i = -k_p(p_i - \bar{p}_i) - k_d\dot{p}_i, \quad (7.8)$$

where both k_p and k_d are positive constants.

The latter part of (7.8) $k_d\dot{p}_i$ is the viscous friction introduced [111], where k_d is the friction coefficient and \dot{p}_i represents the velocity of the robot i . This part is used for eliminating the oscillatory behavior [112] when the robot gets close to its destination. The viscous term guarantees the robot coming to a standstill state even with no external force.

7.3.3 Neutralizing Control

Proportional control is used for the neutralizing chemical releasing. The amount of chemicals each robot releases is proportional to the average pollutant concentration in the Voronoi cell belonging to that robot.

$$u_{spray_i}(t) = -k_{pr} \frac{\int_{\bar{V}_i} \rho(x, y) dV}{\int_{\bar{V}_i} dV}, \quad (7.9)$$

$\bar{V}_i = V_i \cap C_i$ where $C_i = \{q \mid |q - p_i| < r_i\}$, r_i represents the sensing range of i th actuator, and V_i is the Voronoi diagram of actuator i .

7.4 Information Consensus in CVT-Based Diffusion Control

In this section, we introduce information consensus and sharing to the CVT-based diffusion control. The control goal is to drive the actuators to the affected area and counteract the pollutants as quickly as possible.

7.4.1 Basic Consensus Algorithm

First, we review the first-order consensus algorithms [81, 82, 85]. Let $p_i \in R^m$ be the information states of the i^{th} robot. For robots with single integrator dynamics given by

$$\dot{p}_i = u_i, \quad i = 1, \dots, n, \quad (7.10)$$

where $u_i \in R^m$ is the control input, the following first-order consensus algorithm can be applied:

$$u_i = - \sum_{j=1}^n g_{ij} k_{ij} (p_i - p_j), \quad i = 1, \dots, n, \quad (7.11)$$

where g_{ij} represents the set of robots whose information is available to robot i at time t , and k_{ij} is a positive weighting factor.

For the above consensus algorithm, consensus is said to be reached asymptotically among the n vehicles if $p_i(t) \rightarrow p_j(t)$, $\forall i \neq j$, as $t \rightarrow \infty$ for all $p_i(0)$. A classic rendezvous result is that the rendezvous state can be achieved if the information exchange graph has a spanning tree.

7.4.2 Requirements of Diffusion Control

The pollutant diffusion is both a temporal and a spatial evolution process. CVT method provides a spatial solution to partition the area into small Voronoi diagram and a final state of centroidal Voronoi tessellation can be achieved based on different weighted functions. However, the temporal characteristics is also a big challenge for extending CVT to dynamic diffusion control. There are several challenges to incorporate consensus with CVT-based diffusion control.

- **Converging Speed:** To achieve a better control performance, the actuators should converge quickly to the affected area. But all actuators cannot detect the diffusion simultaneously due to the sensing limits. So, the consensus on the affected area needs to be introduced in such a way that the actuators far away from the diffusion source should move faster towards the area with high concentration.
- **Neutralizing Speed:** The final control performance depends highly on how much and where the neutralizing materials are sprayed out. The total amount of the neutralizing material should be minimized given some final constraints on how much to spray totally.
- **Final State:** CVT algorithm (7.6) or (7.8) can guarantee the actuator asymptotically converge to the diffusion source and form a centroidal Voronoi tessellation. But this

is not enough for diffusion control since a diffusion process evolves with time.

7.4.3 Consensus-Based CVT Algorithm

Based on the above discussions, the new algorithm is proposed for the control of a diffusion process. Consensus algorithm is added on two parts: actuator motion control and actuator spraying/neutralizing control.

Algorithm 7.4.1. *The Consensus-based CVT algorithm is described below:*

- (1) *Initial setting: actuator $p_i \in \{p_1, \dots, p_n\}$, response time $t = 0$, concentration threshold k_a .*
- (2) *Compute Voronoi region \bar{V}_i .*
- (3) *Get the sensor data within the range r_s and compute centroid \bar{p}_i and total pollutant in this region P_{total_i} .*
- (4) *Talk with neighboring actuators. If no diffusion ($\forall i, P_{total_i} < k_a$), go to 5); else apply corresponding control laws:*
 - (a) *If actuator p_i is out of the affected region ($P_{total_i} < k_a$), make a consensus with neighbors on where is the affected area.*
 - (b) *If actuator p_i is within the affected region ($P_{total_i} > k_a$), make a consensus with neighbors on how fast to spray.*
 - (c) *Else, use CVT control law (7.6) or (7.8).*
- (5) *Stop since no pollution detected.*

In what follows, we will explain in detail the two consensus algorithms for motion control and spraying control.

Consensus in Actuator Motion Control

In the diffusion process, the actuators sense and react to the diffusion according to the distance from the source. Consensus is introduced here for faster converging speed. First, the affected area is defined as:

$$A_j = \{q \in \Omega | \rho(q) > k_a\} = \{q \in \Omega | |q - d_j| < r_j(t)\}, \quad (7.12)$$

where d_j is the position of the j th diffusion source, k_a is a positive constant representing the concentration threshold, $r_j(t)$ represents the radius of the affected area. Here we assume there is no wind or other reasons affecting the diffusion process. The consensus to the affected area turns out to be a multi-leaders consensus problem. That is, the actuators out of affected area will follow the the actuators already in the affected area. In other words, the diffusion-undetected actuators will follow the diffusion-detected actuators or rendezvous to them until they enter the affected area A_i . The difference with the common ‘‘Rendezvous Problem’’ is that here we need rendezvous to an affected area instead of one point. This can be achieved with disconnected communication topology [85].

$$u_i = - \sum_{j=1}^n g_{ij} k_{ij} (p_i - p_j), \quad i = 1, \dots, n, \quad (7.13)$$

where $k_{ij} > 0$, $g_{ij} = 0$ and g_{ij} will be set to 1 if information flows from actuator j to i . In our case, it is mostly leader-follower case. The followers just need to rendezvous to the leaders which are already in the affected area.

Assuming that actuator j is out of the affected area at time t_d , \mathcal{K} should be minimized

$$\begin{aligned} \frac{\partial \mathcal{K}}{\partial p_j} &= 2M_{V_i}(p_i - \bar{p}_i) \simeq 0, \\ M_{V_i} &\simeq 0. \end{aligned} \quad (7.14)$$

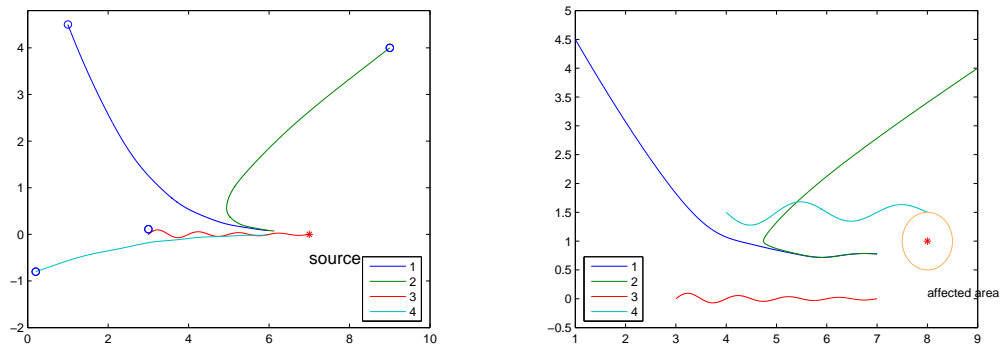
Based on plain CVT actuator motion planning, the actuator j will not react until $|p_i - \bar{p}_i| > \delta$. But the consensus algorithm introduces the information sharing among actuator so that

the actuator out of affected area can react early and achieve a faster converging speed.

We set up an emulated scenario to show our idea. Suppose only one actuator (actuator #3) is close to the diffusion source and detect the diffusion very early Fig. 7.2(a). With CVT algorithm, the actuator #3 can drive to the affected area asymptotically. However, other actuators will not react to the diffusion quickly enough since it takes time for the pollutant to enter the area close to other actuators. With consensus algorithm, the actuator #3 can broadcast to the other actuators, or act as the leader of the group and lead all the others into the affected area. In Fig. 7.2(b), there are two actuators (#1, #4) which are close to the affected area. So, they will respond to both of the early arrivers and converge to the middle of actuator #1 and #4, which is also the affected area that needs to be controlled or sprayed. With this algorithm, consensus can be reached asymptotically for the n actuators since $p_i - d_j \rightarrow r_j(t)$, as $t \rightarrow \infty$ for all p_i .

Consensus in Actuator Neutralizing Control

The plain CVT algorithm introduces a spatial solution to the diffusion control problem [108]. However, the neutralizing control part may not balance. Given a typical pollution/spraying control scenario using the plain CVT algorithm (Fig. 7.3), we can observe from Fig. 7.4 that the actuator #4 sprays more neutralizing chemicals than the total sprayed by the other three, which is not an efficient way when employing more actuators.



(a) 1 Leader (#3) and 3 Followers (#1, #2, #4). (b) 2 Leaders (#3, #4) and 2 Followers (#1, #2).

Fig. 7.2: Simulation: rendezvous to the affected area.

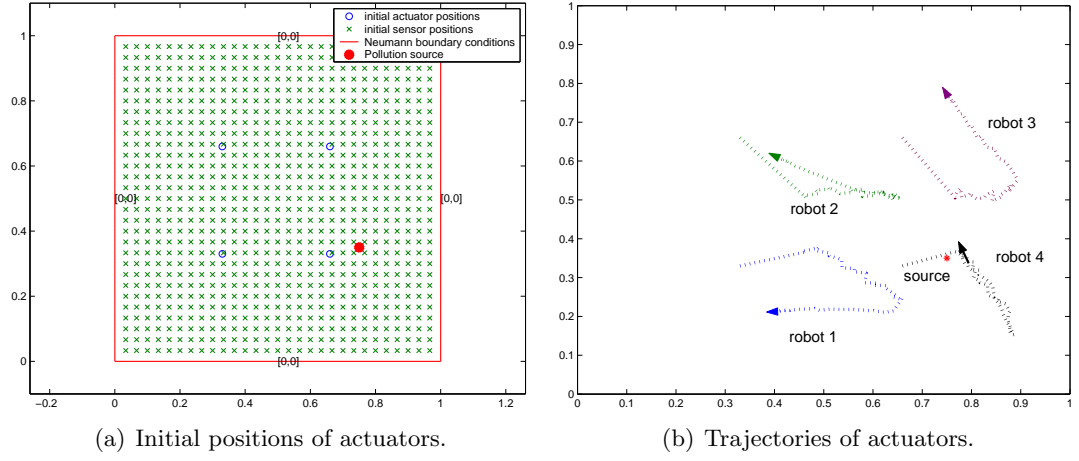


Fig. 7.3: Plain CVT diffusion control.

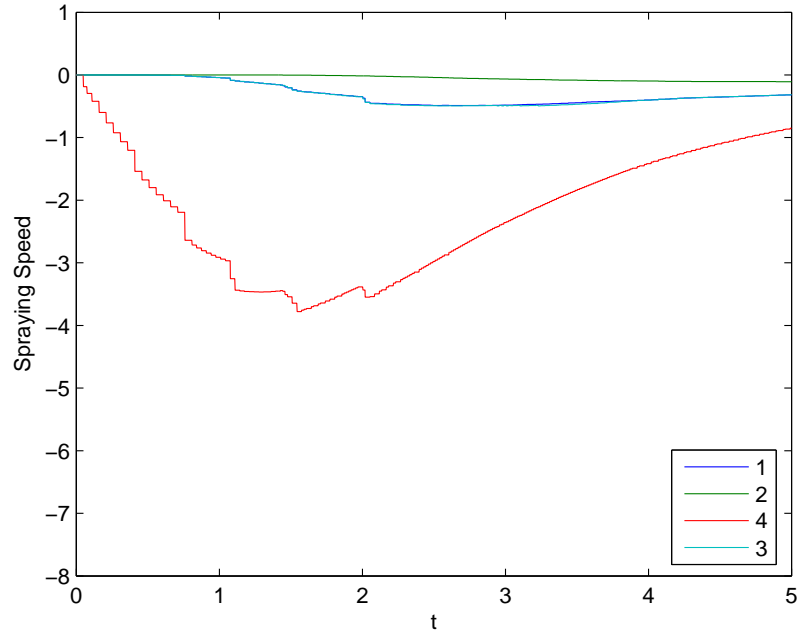


Fig. 7.4: Spraying speed comparison for CVT.

In our present study, consensus is introduced to neutralizing control for maximizing the neutralizing ability of every actuator [113]. Consensus is said to be reached for the n actuators if u_{pr_i} is at the same order of magnitude or as close as possible, $\forall i \neq j$, as $t \rightarrow \infty$. CVT algorithm (7.6) or (7.8) can guarantee the actuator to converge to a final centroidal Voronoi tessellation as $t \rightarrow \infty$, but that is a scenario that can not happen in the

diffusion evolving scenario. To achieve a better control performance, every actuator should be fully used in the neutralizing control. We wish to use the proposed consensus algorithm to avoid the situation that we could not send as many as possible mobile actuators to the most affected area.

To achieve this, the following spraying control input can be applied

$$u_i = -k_p(p_i - \bar{p}_i) - \sum_{j=1}^N g_{ij}k_{ij}(p_i - p_j), \quad (7.15)$$

where g_{ij} and k_{ij} have the same definitions as in (7.11). The first part $p_i - \bar{p}_i$ drives the actuator respond to the diffusing and the later part in (7.15) will drive the actuators closer to the actuator that has the highest P_{total_i} .

7.5 Simulation Results

Two simulation examples are shown to demonstrate the effectiveness of the new algorithm. The first one has no constrain limits on how much to spray totally $k_s = \infty$. The second one illustrate how this constrains will affect the final control performance. The implementation details are provided in Appendix D.

Diff-MAS2D [114] is used as the simulation platform for our implementation. The area concerned can be modeled by $\Omega = \{(x, y) | 0 \leq x \leq 1, 0 \leq y \leq 1\}$. In (7.1) $k = 0.01$ and the boundary condition is given by

$$\frac{\partial u}{\partial n} = 0. \quad (7.16)$$

The stationary pollution source is modeled as a point disturbance f_d to the the PDE system (7.1) with its position at $(0.8, 0.2)$ and

$$f_d(t) = 20e^{-t}|_{(x=0.8, y=0.2)}. \quad (7.17)$$

The mesh sensor network is assumed to provide the actuators with measurements on pollutant concentration. There are 29×29 sensors evenly distributed in a square area $(0, 1)^2$ (a unit area) and four mobile actuators/robots that can release the neutralizing chemicals.

The pollution source begins to diffuse at $t = 0$ to the area Ω and initially the mobile actuator robots are evenly distributed within the domain Ω (one by one square) at the following specific positions: for 2×2 grouping case, $(0.33, 0.33), (0.33, 0.66), (0.66, 0.33), (0.66, 0.66)$. The actuators and sensors get updates every $0.1s$. The dynamic model of actuator is assumed to be the first order. We will add more simulation results for the second order model in the final version.

Given the initial layout Fig. 7.5, we need to choose the corresponding control law and communication matrix. Let's consider the vector form of control input:

$$U = L_1 P - L_2 \bar{P}, \quad (7.18)$$

where $U = [u_1^T \cdots u_n^T]$, $P = [p_1^T \cdots p_n^T]$, $\bar{P} = [\bar{p}_1^T \cdots \bar{p}_n^T]$ are all vectors, L_1 is the control matrix determined by communication topology and corresponding control law.

In the beginning, the actuator #3 is relatively close to the diffusion process, and it will detect and react to the diffusing first. Then, it will broadcast this event to all the other

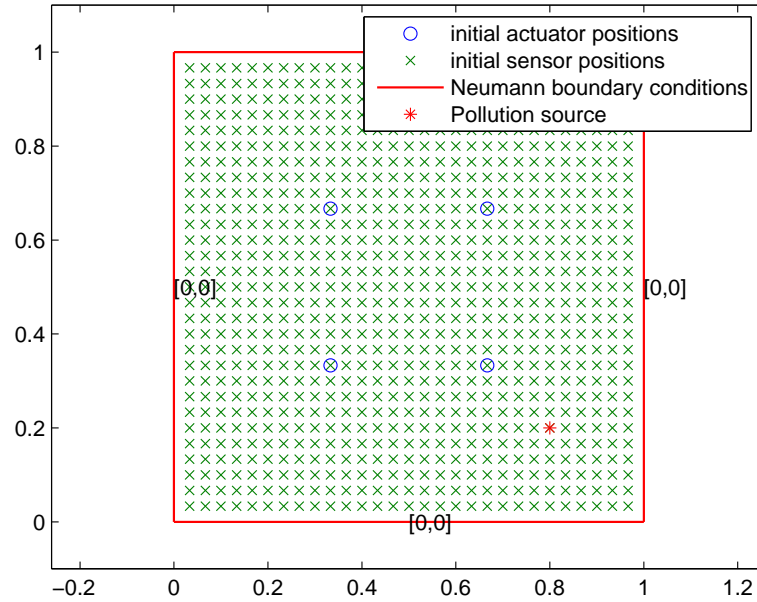


Fig. 7.5: Initial layout of diffusion control.

three actuators. The communication topology shown in Figs. 7.6 and 7.7. The control matrixes L_1 and L_2 are shown below:

$$\mathbf{L}_1 = \begin{pmatrix} -1 & 0 & 1 & 0 \\ 0 & -1 & 1 & 0 \\ 0 & 0 & -1 & 0 \\ 0 & 0 & 1 & -1 \end{pmatrix}, \quad \mathbf{L}_2 = \begin{pmatrix} 0 & 0 & 0 & 0 \\ 0 & 0 & 0 & 0 \\ 0 & 0 & -1 & 0 \\ 0 & 0 & 0 & 0 \end{pmatrix}.$$

After a certain time, actuator #1 and #4 also enter the affected area. The communication topology and control matrix are then changed:

$$\mathbf{L}_1 = \begin{pmatrix} -1 & 1 & 1 & 1 \\ 0 & -1 & 0 & 0 \\ 0 & 0 & -1 & 0 \\ 0 & 0 & 0 & -1 \end{pmatrix}, \quad \mathbf{L}_2 = \begin{pmatrix} 0 & 0 & 0 & 0 \\ 0 & -1 & 0 & 0 \\ 0 & 0 & -1 & 0 \\ 0 & 0 & 0 & -1 \end{pmatrix}.$$

After all the four actuators have entered the affected area, the S_{total_i} are compared and converted to step 4c for consensus on the amounts of neutralizing chemicals. The actuator trajectories are shown in Fig. 7.8.

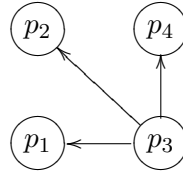


Fig. 7.6: p_3 alone broadcasts.

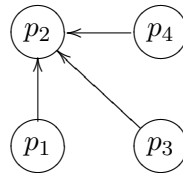


Fig. 7.7: p_1 , p_3 and p_4 broadcast.

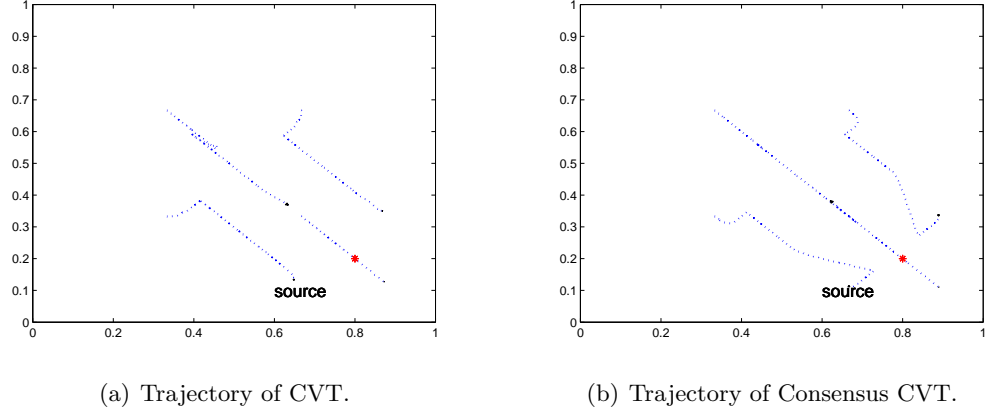


Fig. 7.8: Trajectory comparison between the consensus-based CVT and plain CVT.

$$\mathbf{L}_1 = \begin{pmatrix} -1 & 0 & 1 & 0 \\ 0 & -1 & 1 & 0 \\ 0 & 0 & -1 & 0 \\ 0 & 0 & 1 & -1 \end{pmatrix}, \quad \mathbf{L}_2 = \begin{pmatrix} -1 & 0 & 0 & 0 \\ 0 & -1 & 0 & 0 \\ 0 & 0 & -1 & 0 \\ 0 & 0 & 0 & -1 \end{pmatrix}.$$

Figure 7.9 and Table 7.1 show the control performance comparison between plain CVT and consensus-based CVT, which shows a decrease in both the max and final total pollution value. The time actuators takes to arrive at the affected area can be compared in Fig. 7.10. Consensus-based CVT has a better control performance on the diffusion process over the plain CVT.

When controlling a diffusion process, another important factor is the constrains on the total neutralizing chemical sprayed (7.3). To make a comparison between consensus-based CVT and the plain CVT, the total neutralizing amount is reduced to 70% of the preceding case. For consensus-based CVT, a saturation $[-2, 0]$ is added to guarantee the balance of

Table 7.1: Comparison of control performance.

Algorithm	P_{max}	t_{max}	P_{final}
CVT	12.9186	1.7980	1.9330
ConsensusCVT	12.7850	1.7420	1.5743
CVT (Spray Limits)	10.3318	2.3080	4.6901
Consensus (Spray limits)	12.7850	1.7420	2.9365

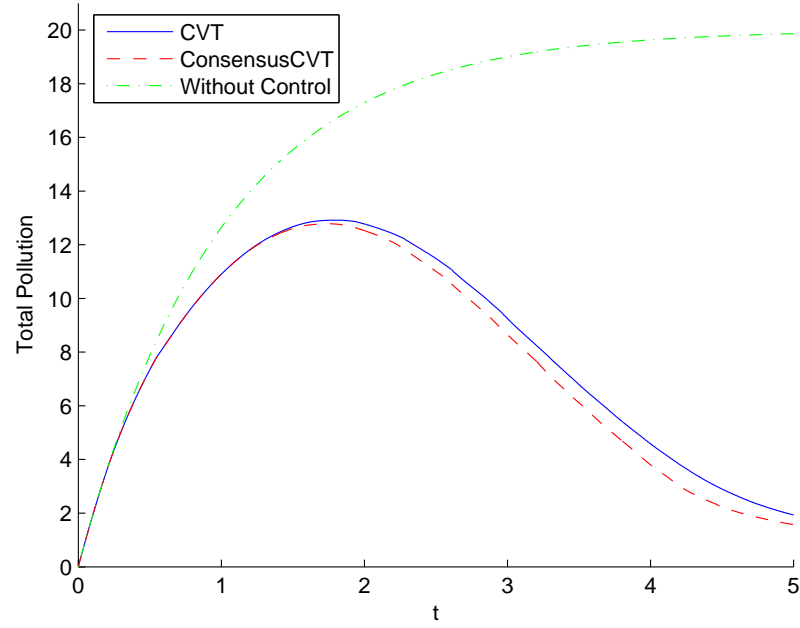


Fig. 7.9: Comparison of total pollutants: plain CVT and consensus CVT.

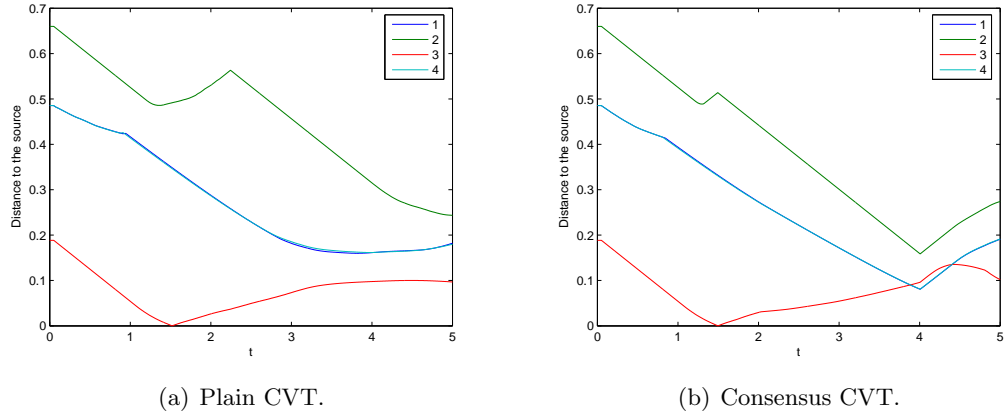


Fig. 7.10: Distance to the source.

spraying speed among actuators. The initial layout and all parameters are the same with the above simulation. The motion trajectories are shown in Fig. 7.11.

From Fig. 7.12 and Table 7.1, we can observe that although the maximal total pollutant is smaller, the final pollutant left using plain CVT is 4.6901, which is much more than that achieved via the consensus-based CVT as low as 2.9365. So, this strategy is not so good

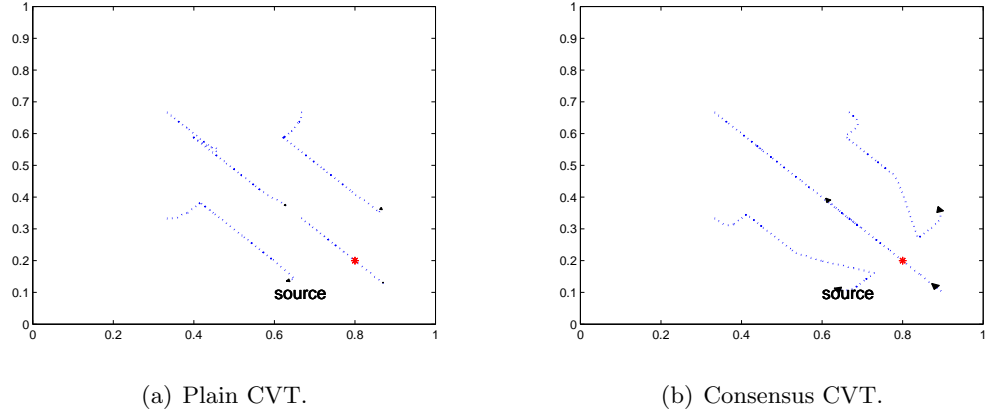


Fig. 7.11: Actuator trajectories of consensus-based CVT and plain CVT.

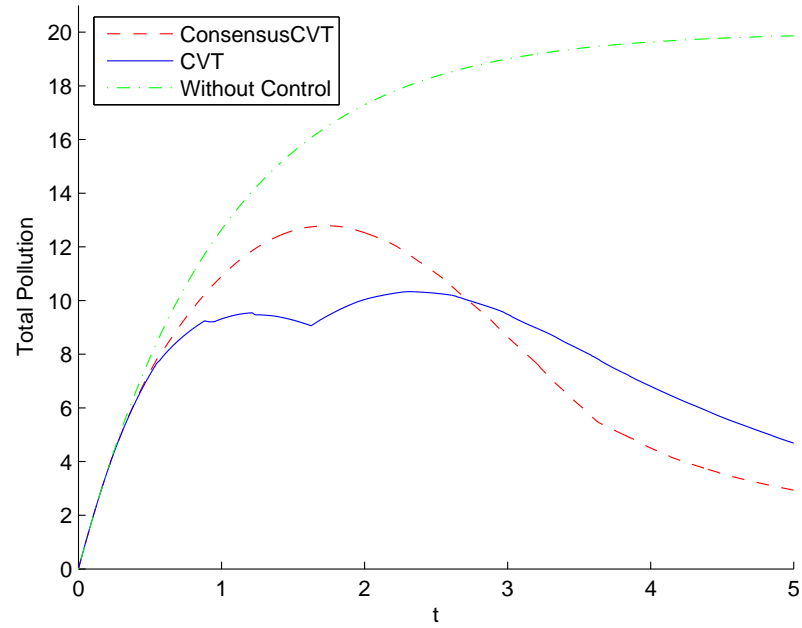


Fig. 7.12: Comparison of total pollutants: plain CVT and consensus CVT.

because it does not make fully use of the neutralizing ability of all the four actuators.

In summary, the diffusion control problem is quite difficult because it evolves both spatially and temporally and PDEs are needed for modeling. There is still no good solution. Based on the presented simulation results, the following further discussions are presented in order.

- **Mobile Actuator Control Problem:** One of the difficulties in diffusion control is that both actuator position and neutralizing speed need to be controlled. Especially, the neutralizing control strategy can have a large impact on the final control performance. Different control laws can be designed for various requirements. As shown in Figs. 7.12 and 7.13, CVT algorithm has smaller maximum pollutant values (see Table 7.2) but quickly sprays out the total neutralizing chemicals. Consensus CVT outperforms CVT in this aspect because it pays more attention to inter-actuator communication and tries to maintain a balance of neutralizer amount among actuators.
- **CVT Advantages and Limitations:** CVT algorithm is a non-model-based method to control a diffusion process and it is easy to implement in a large-scale since it needs only the neighbor information. The diffusion source can be moving and can be multiple. However, CVT can only guarantee the slow converging to the source, as seen in Fig. 7.10. The final diffusion control performance depends a lot on the initial conditions like the starting points of actuators. The converging speed and computation burden are also limitations for CVT [106].
- **Communication Topology:** This chapter assumes that the actuator can get the sensor information within a certain distance of effectiveness and a full communication topology among actuators. But the simulation result is only based on some specific communication topologies. Further tests are needed for topology changing or switching while actuator moving and spraying.
- **2D/3D Spatial Problem:** CVT algorithm is a spatial solution to the diffusion control problem. With the availability of small and powerful robots and sensor network,

Table 7.2: Comparison of total neutralizing material.

Algorithm	S_1	S_2	S_3	S_4
CVT	4.25	0.53	9.01	4.18
ConsensusCVT	4.47	0.69	8.75	4.42
CVT (Spray limits)	3.89	0.31	7.01	4.02
Consensus (Spray limits)	4.67	0.70	7.00	4.61

these kind of spatial problem will sooner or later be solved. Unmanned aerial vehicles (UAVs) will be perfect platforms for this kind of experiments [68].

- Experimental validation: More experiments on real mobile sensor and actuator networks will be interesting to validate the ideas in this chapter.

7.6 Chapter Summary

In this chapter, we proposed to incorporate the information sharing and consensus strategy to the Centroidal Voronoi Tessellation-based actuators motion planning for better control of a diffusing process. The new algorithm is tested with a first order dynamic model and its improvement has been demonstrated, especially under total spraying amount limit. Further simulation results and comparisons can be made in the future using a second order actuator model.

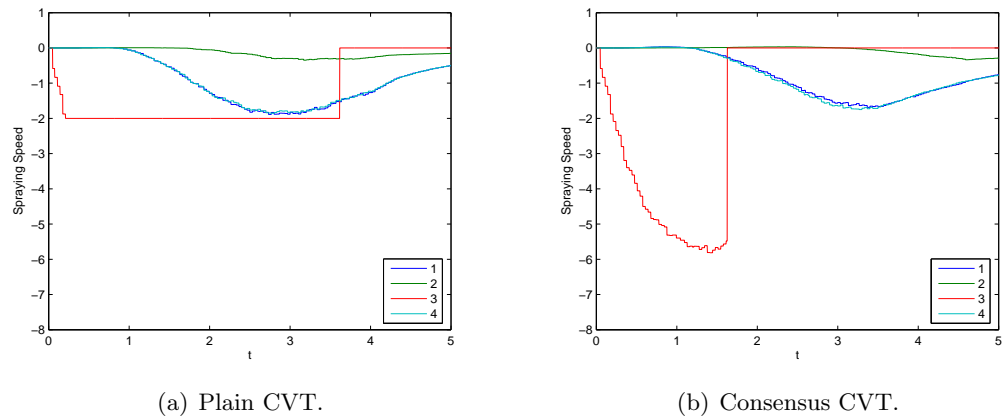


Fig. 7.13: Comparison of spraying speeds.

Chapter 8

Conclusions and Future Research Suggestions

8.1 Conclusions

This dissertation provides new approaches on using unmanned vehicles for remote sensing and distributed control applications. The goal is to bridge the gap between the estimation and control theories of unmanned systems and real environmental or agricultural applications. The AggieAir UAS platform is first introduced in Chapter 2 with a detailed small UAV system review, the subsystem design, the IMU interface design, and the whole system integration tests. The big challenge here is to provide a low-cost yet robust solution since most agricultural and environmental scenarios can not afford expensive UAVs, which are usually more than \$10,000. Our AggieAir2 platform has shown great performance for remote sensing applications with the lowest possible price (about \$3500 for all the hardware), to the author's best knowledge. With the robust platform, more algorithms have been tested to get a better estimation and control performance. In Chapter 3, the state estimation algorithm is focused because its importance for the flight control and the later georeferencing. Several typical state estimation filters are tested on our own flight data, including different kinds of extended Kalman filters. Chapter 4 is about an advanced lateral flight controller design. The fractional calculus-based techniques are used on the roll channel of the flight control system. A designed PI^α controller show better tracking performance than the designed PID controller both in simulations and real flights. Then, the single and multiple UAV-based remote sensing problems are focused in Chapter 5 and Chapter 6, respectively. The path planning subproblem and the georeferencing problem are solved separately. Chapter 7 is devoted to the diffusion control problem using mobile sensor and actuator networks.

8.2 Future Research Suggestions

Many challenges remain when we apply unmanned systems for civilian applications. Our successful AggieAir UAV platform uses the fixed-wing airframe. However, there are scenarios like chemical leaking in a factory or urban areas, which requires a more flexible aerial platform; for example a helicopter-like UAV, or vertically take-off and landing (VTOL) UAV.

8.2.1 VTOL UAS Design for Civilian Applications

VTOL UAVs can fly at extremely low heights with a low ground speed or even stay at a certain position in hovering mode. They could take off and land more easily, independent of runways or complex terrains, which make them especially useful for indoor and surface applications. VTOL UAVs have the following advantages over traditional fixed-wing UAVs.

- Easy for launching and landing even among buildings, on boats, or on moving trucks.
- Much better vertical maneuverability.
- Hovering capability, which is good for image capturing.
- Capable of both very slow and fast flying speed.
- Safer to manipulate and more portable (no wings).

With all the above specialties, VTOL UAVs have many potential civilian applications especially in complex urban areas, which may not be suitable for fixed wing UAVs since a closer aerial view is required. There are many example tasks.

- Inspection of outdoor or indoor structures: Aerial images collected by VTOL UAVs from multiple views can be used for inspection of dams, bridges, tunnels, or power lines instead of sending human beings there.
- Transportation applications: VTOL UAVs can provide big advantages to routine works of the department of transportation. Sample applications include road health

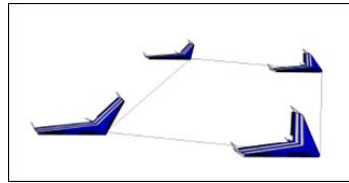
monitoring, traffic surveillance, construction monitoring, etc. High resolution images taken from VTOL UAVs can even help reconstruct the traffic accident scene.

- **Accurate 3D measurements:** The omni-directional mobility of the VTOL UAV increases its flexibility for measurements in a 3D space. For instance, VTOL UAVs can be used to measure the vertical wind speed more accurately than fixed-wing UAVs since they can hover in the air.
- **Thermal audit:** VTOL UAVs with thermal imagers can be used to determine where the heat leaking of a building is for energy saving purposes.
- **High resolution and high quality photos and videos in the air:** VTOL UAVs can be easily carried around, launched, and sent to any altitude around the building or the scene for an aerial view.
- **Education and entertainment:** VTOL UAVs can be demonstrated or used even inside buildings because they do not require much space for take-off and landing.

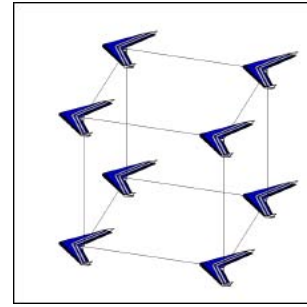
8.2.2 Monitoring and Control of Fast-Evolving Processes

Fast-evolving processes often need faster information collection and control decision which is especially suitable for unmanned systems. Both the fog monitoring and the diffusion control problem are only tested in the DiffMAS2D software simulation platform so far. It will be interesting if we can use UAVs to monitor a real diffusion process. The development of algorithms regarding emergence responses will be very useful for dangerous missions like forest fires monitoring or chemical leaks predictions.

In addition, UAVs can form groups for these missions to provide even quicker responses. UAVs flying in meshes or cubes provide more real-time information compared with a single UAV, shown in Fig. 8.1 [115]. They can even coordinate with each other on variables like the vehicle distance or formation shape based upon requirements from different missions.



(a) Flying mesh.



(b) Flying cube.

Fig. 8.1: UAVs in formation.

8.2.3 Other Future Research Suggestions

There are several other future research suggestions regarding the UAV project including:

- Risk analysis: The robustness analysis of small UAVs is still a new topic. The probability of failure for small UAV manipulations needs to be modeled and analyzed for flight safety requirements.
- UAV as the actuator: Most current UAV applications are for surveillance and monitoring purposes. However, UAV can also work as an actuator. For instance, a VTOL UAV can be used for soil sampling missions with a manipulator installed.
- New UAV design to use fuel cell batteries: The current power system for AggieAir UAS uses Li-Polymer batteries, with the power density of about 185 Wh/kg. However, the power density of the new fuel cell batteries could be as high as 450 Wh/kg [116]. The usage of fuel cell battery can greatly increase the UAV flight time.
- Power consumption minimization: The current AggieAir system is stable but not optimal on the power consumption. Both the flight control strategies and the airframe designing can be optimized to get more flight time.

References

- [1] D. W. Casbeer, S. M. Li, R. W. Beard, T. W. McLain, and R. K. Mehra, "Forest fire monitoring with multiple small UAVs," in *Proceedings of the 2005 American Control Conference*, pp. 3530–3535, June 2005.
- [2] H. Chao, Y. Cao, and Y. Q. Chen, "Autopilots for small unmanned aerial vehicles: a survey," *International Journal of Control, Automation, and Systems*, vol. 8, no. 1, pp. 36–44, 2010.
- [3] J. S. Jang and D. Liccardo, "Small UAV automation using MEMS," *IEEE Aerospace and Electronic Systems Magazine*, vol. 22, no. 5, pp. 30–34, 2007.
- [4] D. B. Kingston and R. W. Beard, "Real-time attitude and position estimation for small UAVs using low-cost sensors," in *Proceedings of the AIAA 3rd Unmanned Unlimited Systems Conference and Workshop*, no. AIAA-2007-6514, Chicago, IL, Sept. 2004.
- [5] L. Perea, J. How, L. Breger, and P. Elosegui, "Nonlinearity in sensor fusion: Divergence issues in EKF, modified truncated SOF, and UKF," in *Proceedings of the 2007 AIAA Guidance, Navigation and Control Conference and Exhibit*, no. AIAA-2007-6488, Aug. 2007.
- [6] J. Nino, F. Mitrachea, P. Cosynb, and R. D. Keyser, "Model identification of a micro air vehicle," *Journal of Bionic Engineering*, vol. 4, no. 4, pp. 227–236, 2007.
- [7] H. Wu, D. Sun, K. Peng, and Z. Zhou, "Modeling identification of a micro air vehicle in loitering flight based on attitude performance evaluation," *IEEE Transactions on Robotics and Automation*, vol. 20, no. 4, pp. 702–712, 2004.
- [8] Y. Lee, S. Kim, and J. Suk, "System identification of an unmanned aerial vehicle from automated flight tests," in *Proceedings of the AIAA's 1st Technical Conference and Workshop on Unmanned Aerospace Vehicles*, May 2002.
- [9] G. Cai, B. M. Chen, K. Peng, M. Dong, and T. H. Lee, "Modeling and control of the yaw channel of a UAV helicopter," *IEEE Transactions on Industrial Electronics*, vol. 55, no. 9, pp. 3426–3434, 2008.
- [10] S. Duranti and G. Conte, "In-flight identification of the augmented flight dynamics of the RMAX unmanned helicopter," in *Proceedings of the Seventeenth IFAC Symposium on Automatic Control in Aerospace*, June 2007.
- [11] D. Ucinski, *Optimal Measurement Methods for Distributed Parameter System Identification*. Boca Raton, FL: CRC Press, 2004.

- [12] Y. Q. Chen, Z. Wang, and J. Liang, "Actuation scheduling in mobile actuator networks for spatial-temporal feedback control of a diffusion process with dynamic obstacle avoidance," in *Proceedings of the 2005 IEEE International Conference on Mechatronics and Automation*, pp. 1630–1635, June 2005.
- [13] H. Chao, Y. Q. Chen, and W. Ren, "A study of grouping effect on mobile actuator sensor networks for distributed feedback control of diffusion process using central voronoi tessellations," *International Journal of Intelligent Control Systems*, vol. 11, no. 2, pp. 185–190, 2006.
- [14] J. Cortés, S. Martínez, T. Karatas, and F. Bullo, "Coverage control for mobile sensing networks," *IEEE Transactions on Robotics and Automation*, vol. 20, no. 20, pp. 243–255, 2004.
- [15] B. James, *Introduction to Remote Sensing*, 4th ed. New York: Guilford Press, 2006.
- [16] L. Johnson, S. Herwitz, B. Lobitz, and S. Dunagan, "Feasibility of monitoring coffee field ripeness with airborne multispectral imagery," *Applied Engineering in Agriculture*, vol. 20, pp. 845–849, 2004.
- [17] H. Chao, M. Baumann, A. M. Jensen, Y. Q. Chen, Y. Cao, W. Ren, and M. McKee, "Band-reconfigurable multi-UAV-based cooperative remote sensing for real-time water management and distributed irrigation control," in *Proceedings of the 2008 International Federal of Automatic Control (IFAC) World Congress*, pp. 11 744–11 749, July 2008.
- [18] L. Johnson, S. Herwitz, S. Dunagan, B. Lobitz, D. Sullivan, and R. Slye, "Collection of ultra high spatial and spectral resolution image data over California vineyards with a small UAV," in *Proceedings of the 2003 International Symposium on Remote Sensing of Environment*, Nov. 2003.
- [19] B. Tarbert, T. Wierzbanski, E. Chernoff, and P. Egan, "Comprehensive set of recommendations for sUAS regulatory development," Small UAS Aviation Rulemaking Committee, Technical Report, 2009.
- [20] Insitu company, "Insitu UAV introduction," [<http://www.insitu.com/>], 2010.
- [21] u-blox company, "u-blox GPS protocol," [<http://www.u-blox.com>], 2010.
- [22] Microstrain Inc., "Gx2 IMU specifications," [<http://www.mirostrain.com>], 2008.
- [23] Paparazzi Forum, "Open source Paparazzi UAV project," [<http://www.recherche.enac.fr/paparazzi/>], 2008.
- [24] G. K. Egan, "The use of infrared sensors for absolute attitude determination of unmanned aerial vehicles," Monash University, Technical Report MECSE-22-2006, 2006.
- [25] P. J. Roberts, R. A. Walker, and P. J. O'Shea, "Fixed wing UAV navigation and control through integrated GNSS and vision," in *Proceedings of the 2005 AIAA Guidance, Navigation, and Control Conference and Exhibit*, no. AIAA 2005-5867, Aug. 2005.

- [26] D. Damien, B. Wageeh, and W. Rodney, "Fixed-wing attitude estimation using computer vision based horizon detection," in *Proceedings of the 2007 Australian International Aerospace Congress*, pp. 1–19, Mar. 2007.
- [27] A. J. Calise, E. N. Johnson, M. D. Johnson, and J. E. Corban, "Applications of adaptive neural-network control to unmanned aerial vehicles," in *Proceedings of the 2003 AIAA/ICAS International Air and Space Symposium and Exposition: The Next 100 Years*, June 2003.
- [28] H. Chao, Y. Luo, L. Di, and Y. Q. Chen, "Fractional order flight control of a small fixed-wing UAV: Controller design and simulation study," in *Proceedings of the 2009 ASME International Design Engineering Technical Conference Computers and Information in Engineering*, no. MESA-87574, Sept. 2009.
- [29] M. Kumon, Y. Udo, H. Michihira, M. Nagata, I. Mizumoto, and Z. Iwai, "Autopilot system for Kiteplane," *IEEE/ASME Transactions on Mechatronics*, vol. 11, no. 5, pp. 615–624, 2006.
- [30] E. N. Johnson and S. Kannan, "Adaptive flight control for an autonomous unmanned helicopter," in *Proceedings of the 2002 AIAA Guidance, Navigation and Control Conference*, no. AIAA-2002-4439, Aug. 2002.
- [31] M. L. F. Santoso and G. K. Egan, "Linear quadratic optimal control synthesis for a UAV," in *Proceedings of the 12th Australian International Aerospace Congress*, Mar. 2007.
- [32] M. Sadraey and R. Colgren, "2 DOF robust nonlinear autopilot design for a small UAV using a combination of dynamic inversion and h -infinity loop shaping," in *Proceedings of the 2007 AIAA Guidance, Navigation and Control Conference*, no. AIAA-2005-6402, Aug. 2005.
- [33] R. Beard, D. Kingston, M. Quigley, D. Snyder, R. Christiansen, W. Johnson, T. McLain, and M. Goodrich, "Autonomous vehicle technologies for small fixed wing UAVs," *Journal of Aerospace Computing, Information, and Communication*, vol. 5, no. 1, pp. 92–108, 2005.
- [34] CloudCap Inc., "Piccolo autopilot specifications," [<http://www.cloudcaptech.com>], 2008.
- [35] A. M. Jensen, "gRAID: A geospatial real-time aerial image display for a low-cost autonomous multispectral remote sensing platform," Master's thesis, Utah State University, 2009.
- [36] Y. Han, "An autonomous unmanned aerial vehicle-based imagery system development and remote sensing images classification for agricultural applications," Master's thesis, Utah State University, 2009.
- [37] NASA, "World wind software," [<http://worldwind.arc.nasa.gov/index.html>], 2007.
- [38] W. F. Phillips, *Mechanics of Flight*. Hoboken, NJ: John Wiley & Sons, 2004.

- [39] Unicorn Ventures Ltd., “The Unicorn assembly and flight manual,” [<http://lib.store.yahoo.net/lib/unicornwings/Manual.pdf>], 2004.
- [40] Palos RC Flying Club, “CG calculator,” [<http://www.palosrc.com/instructors/cg.htm>], 2009.
- [41] B. L. Stevens and F. L. Lewis, *Aircraft Control and Simulation*, 2nd ed. Hoboken, NJ: John Wiley & Sons, 2003.
- [42] A. M. Jensen, M. Baumann, and Y. Q. Chen, “Low-cost multispectral aerial imaging using autonomous runway-free small flying wing vehicles,” in *Proceedings of the 2008 IEEE International Conference on Geoscience and Remote Sensing*, pp. 506–509, July 2008.
- [43] Gumstix, “Gumstix verdex specifications,” [<http://www.gumstix.com>], 2008.
- [44] M. Baumann, “Imager development and image processing for small UAV-based real-time multispectral remote sensing,” Master’s thesis, University of Applied Sciences Ravensburg-Weingarten and Utah State University, 2007.
- [45] Y. Han, A. M. Jensen, and H. Dou, “Programmable multispectral imager development as light weight payload for low cost fixed wing unmanned aerial vehicles,” in *Proceedings of the 2009 ASME Design Engineering Technical Conference Computers and Information in Engineering*, no. MESA-87741, Sept. 2009.
- [46] “gPhoto,” [<http://www.gphoto.org/>], 2008.
- [47] “Picture Transfer Protocol,” [http://en.wikipedia.org/wiki/Picture_Transfer_Protocol], 2008.
- [48] P. Brisset, A. Drouin, M. Gorraz, P. S. Huard, and J. Tyler, “The Paparazzi solution,” in *Micro Aerial Vehicle (MAV) 2006*, Nov. 2006.
- [49] Jordi Munoz and Bill Premerlani, “AuduIMU open source project,” [<http://diydrones.com/profiles/blogs/arduimu-v2-demo-video>], 2009.
- [50] R. Mahony, T. Hamel, and J.-M. Pflimlin, “Nonlinear complementary filters on the special orthogonal group,” *IEEE Transactions on Automatic Control*, vol. 53, no. 5, pp. 1203–1218, 2008.
- [51] R. M. Murray, Z. Li, and S. S. Sastry, *A Mathematical Introduction to Robotic Manipulation*. Boca Raton, FL: CRC Press, 1994.
- [52] William Premerlani, “DCM estimation,” [<http://gentlenav.googlecode.com>], 2009.
- [53] G. Welch and G. Bishop, “An Introduction to the Kalman Filter,” University of North Carolina at Chapel Hill, Report, July 2006, uRL [<http://www.cs.unc.edu/welch/kalman/kalmanIntro.html>].
- [54] I. Podlubny, “Fractional-order systems and $PI^\lambda D^\mu$ controller,” *IEEE Transactions on Automatic Control*, vol. 44, no. 1, pp. 208–214, 1999.

- [55] D. Xue, C. Zhao, and Y. Q. Chen, "Fractional order PID control of a DC-motor with elastic shaft: a case study," in *Proceedings of the 2006 American Control Conference*, pp. 3182–3187, June 2006.
- [56] C. A. Monje, E. Liceaga-Castro, and J. Liceaga-Castro, "Fractional order control of an unmanned aerial vehicle (UAV)," in *Proceedings of the 2008 International Federation of Automatic Control (IFAC) World Congress*, pp. 15 285–15 290, July 2008.
- [57] C. A. Monje, B. M. Vinagre, V. Feliu, and Y. Q. Chen, "Tuning and auto-tuning of fractional order controllers for industry applications," *Control Engineering Practice*, vol. 16, no. 7, pp. 798–812, 2008.
- [58] Y. Q. Chen, T. Bhaskaran, and D. Xue, "Practical tuning rule development for fractional order proportional and integral controllers," *Journal of Computational and Nonlinear Dynamics*, vol. 3, no. 2, pp. 021 403–1–021 403–8, 2008.
- [59] L. Desborough and R. Miller, "Increasing customer value of industrial control performance monitoring-Honeywell's experience," in *Proceedings of the 6th International Conference Chemical Process Control*, pp. 172–192, July 2001.
- [60] D. Xue and Y. Q. Chen, *Linear Feedback Control: Analysis and Design with MATLAB*. Philadelphia, PA: SIAM Press, 2007.
- [61] L. Ljung, *MATLAB System Identification Toolbox 7 Users Guide*. Natick, MA: The MathWorks, 2009.
- [62] I. Podlubny, *Fractional Differential Equations*. San Diego, CA: Academic Press, 1999.
- [63] H. Li, Y. Luo, and Y. Q. Chen, "A fractional order proportional and derivative (FOPD) motion controller: Tuning rule and experiments," *IEEE Transactions on Control System Technology*, vol. 18, no. 2, pp. 516–520, 2010.
- [64] Y. Q. Chen, "Applied fractional calculus in controls," in *Proceedings of the 2009 American Control Conference*, pp. 34–35, June 2009.
- [65] A. Oustaloup, J. Sabatier, and P. Lanusse, "From fractional robustness to CRONE control," *Fractional Calculus and Applied Analysis*, vol. 2, no. 1, pp. 1–30, 1999.
- [66] Y. Q. Chen, "Impulse response invariant discretization of fractional order low-pass filters," [<http://www.mathworks.com/matlabcentral/fileexchange/21365-impulse-response-invariant-discretization-of-fractional-order-low-pass-filters>], 2008.
- [67] M. Niculescu, "Aerosim Blockset Users Guide," [<http://www.u-dynamics.com>], 2002.
- [68] H. Chao, A. M. Jensen, Y. Han, Y. Q. Chen, and M. McKee, *Advances in Geoscience and Remote Sensing*, ch. AggieAir: Towards low-cost cooperative multispectral remote sensing using small unmanned aircraft systems. Vukovar, Croatia: IN-TECH, 2009.
- [69] CSOIS, "OSAM UAV website," [<http://www.engr.usu.edu/wiki/index.php/OSAM>], 2008.

- [70] S. Z. Fedro, G. S. Allen, and A. C. Gary, "Irrigation system controllers," *Series of the Agricultural and Biological Engineering Department, Florida Cooperative Extension Service, Institute of Food and Agricultural Sciences, University of Florida*, 1993.
- [71] W. R. Terrill, "A FAQ on vegetation in remote sensing," [<http://www.tetracam.com/rsvegfaq.txt>], 1993.
- [72] R. P. Randy and P. Sirisha, "Development of software to rapidly analyze aerial images," in *Proceedings of the 2005 American Society of Agricultural and Biological Engineers Annual International Meeting*, July 2005.
- [73] H. Xiang and L. Tian, "Autonomous aerial image georeferencing for an UAV based data collection platform using integrated navigation system," in *Proceedings of the 2007 American Society of Agricultural and Biological Engineers Annual International Meeting*, June 2007.
- [74] PTGui Developers, "PTGui stitching software," [www.ptgui.com], 2007.
- [75] Y. H. Kaheil, M. K. Gill, M. McKee, L. A. Bastidas, and E. Rosero, "Downscaling and assimilation of surface soil moisture using ground truth measurements," *IEEE Transactions on Geoscience and Remote Sensing*, vol. 46, no. 5, pp. 1375–1384, 2008.
- [76] Y. H. Kaheil, E. Rosero, M. K. Gill, M. McKee, and L. A. Bastidas, "Downscaling and forecasting of evapotranspiration using a synthetic model of wavelets and support vector machines," *IEEE Transactions on Geoscience and Remote Sensing*, vol. 46, no. 9, pp. 2692–2707, 2008.
- [77] S. J. Goetz, "Remote sensing of riparian buffers: Past progress and future prospects," *Journal of the American Water Resources Association*, vol. 42, no. 11, pp. 133–143, 2006.
- [78] Y. Han, H. Dou, and Y. Q. Chen, "Mapping river changes using low cost autonomous unmanned aerial vehicles," in *Proceedings of the 2009 American Water Resources Association Spring Specialty Conference on Managing Water Resources Development in a Changing Climate*, May 2009.
- [79] C. Scientific, "CR200 series brochure," [<http://www.campbellsci.com/2/20354/14/1>], 2005.
- [80] W. Ren and R. W. Beard, "Consensus seeking in multiagent systems under dynamically changing interaction topologies," *IEEE Transactions on Automatic Control*, vol. 50, no. 5, pp. 655–661, 2005.
- [81] A. Jadbabaie, J. Lin, and A. S. Morse, "Coordination of groups of mobile autonomous agents using nearest neighbor rules," *IEEE Transactions on Automatic Control*, vol. 48, no. 6, pp. 988–1001, 2003.
- [82] R. Olfati-Saber and R. M. Murray, "Consensus problems in networks of agents with switching topology and time-delays," *IEEE Transactions on Automatic Control*, vol. 49, no. 9, pp. 1520–1533, 2004.

- [83] J. A. Fax and R. M. Murray, "Information flow and cooperative control of vehicle formations," *IEEE Transactions on Automatic Control*, vol. 49, no. 9, pp. 1465–1476, 2004.
- [84] Z. Lin, M. Broucke, and B. Francis, "Local control strategies for groups of mobile autonomous agents," *IEEE Transactions on Automatic Control*, vol. 49, no. 4, pp. 622–629, 2004.
- [85] W. Ren, H. Chao, W. Bourgeois, N. Sorensen, and Y. Q. Chen., "Experimental validation of consensus algorithms for multi-vehicle cooperative control," *IEEE Transactions on Control Systems Technology*, vol. 16, no. 4, pp. 745–752, 2008.
- [86] W. Bourgeois, L. Ma, P. Chen, Z. Song, and Y. Q. Chen, "Simple and efficient extrinsic camera calibration based on a rational model," in *Proceedings of the IEEE Conference on Mechatronics and Automation*, pp. 177–182, June 2006.
- [87] B. Butler, R. Stratton, J. F. M. Finney and, L. Bradshaw, and D. Jimenez, "Detailed wind information and at its application to improved firefighter safety," in *Proceedings of the Eighth International Wildland Fire Safety Summit*, 2005.
- [88] L. Y. Pao and K. E. Johnson, "A tutorial on the dynamics and control of wind turbines and wind farms," in *Proceedings of the 2009 American Control Conference*, pp. 2076 – 2089, June 2009.
- [89] J. M. Forthofer, B. W. Butler, K. S. Shannon, M. A. Finney, L. S. Bradshaw, and R. Stratton, "Predicting surface winds in complex terrain for use in fire growth models," in *Proceedings of the 5th Symposium on Fire and Forest Meteorology and the 2nd International Wildland Fire Ecology and Fire Management Congress*, Nov. 2003.
- [90] A. Caiti, G. Casalino, E. Lorenzi, A. Turetta, and R. Viviani, "Distributed adaptive environmental sampling with AUVs: Cooperation and team coordination through minimum-spanning-tree graph searching algorithms," in *Proceedings of the Second IFAC Workshop on Navigation, Guidance and Control of Underwater Vehicles*, Apr. 2008.
- [91] D. O. Popa, A. C. Sanderson, V. Hombal, R. J. Komerska, S. S. Mupparapu, D. R. Blidberg, and S. G. Chappel, "Optimal sampling using singular value decomposition of the parameter variance space," in *Proceedings of the 2005 IEEE/RSJ International Conference on Intelligent Robots and Systems*, pp. 3131–3136, Aug. 2005.
- [92] J. Bange, P. Zittel, T. Spieß, J. Uhlenbrock, and F. Beyrich, "A new method for the determination of area-averaged turbulent surface fluxes from low-level flights using inverse models," *Boundary-Layer Meteorology*, vol. 119, no. 3, pp. 527–561, 2006.
- [93] Y. Q. Chen and Z. Wang, "Formation control: a review and a new consideration," in *Proceedings of the 2005 IEEE/RSJ International Conference on Intelligent Robots and Systems*, pp. 3181–3186, Aug. 2005.
- [94] J. M. Wallace and P. V. Hobbs, *Atmospheric Science: An Introductory Survey*. Orlando, FL: Academic Press, 1977.

- [95] D. H. Lenschowa, V. S. Jovcicb, and B. Stevens, "Divergence and vorticity from aircraft air motion measurements," *Journal of Atmospheric and Oceanic Technology*, vol. 24, no. 12, pp. 2062–2072, 2007.
- [96] A. Rodriguez, E. Andersen, J. Bradley, and C. Taylor, "Wind estimation using an optical flow sensor on a miniature air vehicle," in *Proceedings of the 2007 AIAA Guidance, Navigation and Control Conference*, no. AIAA-2007-6614, Aug. 2007.
- [97] H. J. Palanthandalam-Madapusi, A. Girard, and D. S. Bernstein, "Wind-field reconstruction using flight data," in *Proceedings of the 2008 American Control Conference*, pp. 1863–1868, June 2008.
- [98] Procerus Technologies, "Kestrel autopilot specifications," [http://www.procerusuav.com/Downloads/Datasheets/Kestrel_2.2x.pdf], 2008.
- [99] D. G. Long, "Modelling and measurement of near-surface oceanic winds," *International Journal of Modelling and Simulation*, vol. 13, no. 4, pp. 156–161, 1993.
- [100] P. Lynch, "Deducing the wind from vorticity and divergence," *Monthly Weather Review*, vol. 116, no. 1, pp. 86–93, 1987.
- [101] Antnio M. Gameiro Lopes, "WindStation software," [<http://www.easycfd.net/windstation>], 2010.
- [102] D. G. Long and J. M. Mendel, "Model-based estimation of wind fields over the ocean from wind scatterometer measurements. i. development of the wind field model," *IEEE Transactions on Geoscience and Remote Sensing*, vol. 28, no. 3, pp. 349–360, 1990.
- [103] D. Zarchitsky, D. F. Spears, and W. M. Spears, "Swarms for chemical plume tracing," in *Proceedings of the 2005 IEEE Swarm Intelligence Symposium*, pp. 249–256, June 2005.
- [104] M. A. Demetriou, "Power management of sensor networks for detection of a moving source in 2-D spatial domains," in *Proceedings of the 2006 American Control Conference*, pp. 1144–1149, June 2006.
- [105] Y. Q. Chen, K. L. Moore, and Z. Song, "Diffusion boundary determination and zone control via mobile actuator-sensor networks (MAS-net): Challenges and opportunities," in *Proceedings of the 2004 Intelligent Computing: Theory and Applications II, part of SPIE's Defense and Security*, 2004.
- [106] Q. Du, V. Faber, and M. Gunzburger, "Centroidal Voronoi Tessellations: Applications and Algorithms," *SIAM REVIEW*, vol. 41, no. 4, pp. 637–676, 1999.
- [107] L. Ju, Q. Du, and M. Gunzburger, "Probabilistic methods for centroidal voronoi tessellations and their parallel implementations," *Parallel Computation*, vol. 28, no. 10, pp. 1477–1500, 2002.
- [108] Y. Q. Chen, Z. Wang, and J. Liang, "Optimal dynamic actuator location in distributed feedback control of a diffusion process," in *Proceedings of the 44th IEEE Conference on Decision and Control*, pp. 5662–5667, Dec. 2005.

- [109] Y. Q. Chen, Z. Wang, and J. Liang, "Automatic dynamic flocking in mobile actuator sensor networks by central Voronoi tessellations," in *Proceedings of the 2005 IEEE International Conference on Mechatronics and Automation*, vol. 3, pp. 1630–1635, Aug. 2005.
- [110] A. Okabe, B. Boots, and K. Sugihara., *Spatial Tessellations*, 2nd ed. Chichester, UK: John Wiley, 2000.
- [111] A. Howard, M. J. Mataric, and G. S. Sukhatme, "Mobile sensor network deployment using potential fields: A distributed, scalable solution to the area coverage problem," in *Proceedings of the 2002 International Symposium on Distributed Autonomous Robotics Systems*, June 2002.
- [112] N. Heo and P. K. Varshney, "Energy-efficient deployment of intelligent mobile sensor networks," *IEEE Transactions on Systems, Man and Cybernetics, Part A*, vol. 35, no. 1, pp. 78–92, 2005.
- [113] H. Chao, Y. Q. Chen, and W. Ren, "Consensus of information in distributed control of a diffusion process using Centroidal Voronoi Tessellations," in *Proceedings of the 46th IEEE Conference on Decision and Control*, pp. 1441–1446, Dec. 2007.
- [114] J. Liang and Y. Q. Chen, "Diff-MAS2D (version 0.9) user's manual: A simulation platform for controlling distributed parameter systems (diffusion) with networked movable actuators and sensors (MAS) in 2D domain," CSOIS, Utah State University, Technical Report USU-CSOIS-TR-04-03, 2004.
- [115] A. M. Jensen, D. Morgan, S. Clemens, Y. Q. Chen, and T. Hardy, "Using multiple open-source low-cost unmanned aerial vehicles (UAV) for 3D photogrammetry and distributed wind measurement," in *Proceedings of the 2009 ASME Design Engineering Technical Conference Computers and Information in Engineering*, no. MESA-87586, Sept. 2009.
- [116] Horizon Fuel Cell Technologies, "Fuel cell battery for UAVs," [<http://www.hes.sg/>], 2009.
- [117] Xbow Technology, "MNAV IMU specifications," [http://www.xbow.com/Support/Support_pdf_files/MNAV100CA_Users_Manual.pdf], 2009.
- [118] Curtis L. Olson, "Microgear open source project," [<http://cvs.flightgear.org/curt/UAS/MicroGear1>].
- [119] Xsens Company, "Xsens-Mtig IMU specifications," [<http://www.xsens.com>], 2008.

Appendices

Appendix A

IMU/GPS Serial Communication Protocols

Most stand-alone IMUs or GPS units communicate with other devices through serial ports, either RS232, UART, or RS485. The example communication protocols are collected in the appendix including u-blox GPS, several commercial IMUs for the convenience of other GPS/INS developers.

A.1 u-blox GPS Serial Protocol

The UBX GPS messages required for the Paparazzi flight control include [21]:

- UBX_NAV_POSLLH_ID, for latitude, longitude, and altitude;
- UBX_NAV_VELNED_ID, for v_n , v_e , v_d , Heading, GSpeed, and ITOW;
- UBX_NAV_SOL_ID, for Pacc, Sacc, Pdop, and NumSV;
- UBX_NAV_SVINFO_ID, for the satellite information.

The UBX communication protocol with GPS module is defined as follows:

Bytes	1	2	3	4	5	6	6 ~ 5+LEN	6+LEN	7+LEN
	B5	62	CLASS	ID	LEN1	LEN2	PAYLOAD	CK1	CK2

A.2 Microstrain GX2 Serial Protocol

Microstrain GX2 IMU supports multiple modes, and the continuous mode (CC) is used for GhostGX2 including all the sensor data and the rotation matrix [22]. The CC mode is triggered by sending packets (C4, C1, 29, CC) when GhostGX2 starts. The serial packet from Microstrain GX2 IMU after the initialization is defined as follows:

Bytes	1	2~ 75	76	77	78	79	80	81
	SYNC	PAYLOAD	T1	T2	T3	T4	CK1	CK2

A.3 Crossbow MNAV Serial Protocol

Crossbow MNAV IMU has a complete set of sensors for unmanned system applications, shown in Fig. A.1 [117]. The following packets need to be sent to the MNAV to start the scaled mode with full sensor packet [117,118].

- (1) Set up baud rate as 57600 bps (0x55, 55, 57, 46, 01, 00, 02, 00, 03, 00, A3),
- (2) Set sampling frequency as 50 Hz (0x55, 55, 53, 46, 01, 00, 01, 00, 02, 00, 9D),
- (3) Set up scaled mode (0x55, 55, 53, 46, 01, 00, 03, 00, 53, 00, F0).

The serial communication protocol with Crossbow MNAV IMU is defined as follows:

Bytes	1	2	3	4 ~ 3+LEN	4+LEN	5+LEN
	55	55	ID	PAYLOAD	CK1	CK2

The complete data packets have the ID of “S” and “N,” representing the IMU packet without and with GPS, respectively.



Fig. A.1: Crossbow MNAV IMU.

A.4 Xsens Mti-g Serial Protocol

Xsens Mti-g IMU has both the GPS and inertial sensors, shown in Fig. A.2 [119]. The serial communication protocol is defined as follows [119]:

Bytes	1	2	3	4	4~ 3+LEN	4+LEN
	PRE	BID	MID	LEN	PAYLOAD	CKS

For example, GoToConfig message is defined as: 0xFA, FF, 30, 00, 0D.



Fig. A.2: Xsens Mti-g IMU.

Appendix B

Paparazzi Autopilot Software Architecture: A Modification Guide

This guide is to explain the structure of the Paparazzi autopilot software for further modification purposes based on the author's working experiences. The purpose of this guide is to facilitate the readers who are interested in adapting the Paparazzi autopilot for their own developments. The major function of Paparazzi autopilot software is to guide the UAV for the autonomous flight [23]. The autopilot code is written with the C language since it runs on embedded systems like LPC2148. For the airframe and mission specific configurations, the XML files are used including flight plan setting, telemetry selection, and controller tuning, etc. The compiler will convert all these XML files into C files for the code uploading.

B.1 Autopilot Software Structure

In order to achieve the autonomous navigation task, the autopilot needs several sub-functions like collecting data from sensors, actuating control surfaces based on the flight plan, and communicating with the ground for health monitoring and emergency responses. The whole Paparazzi autopilot software structure is shown in Fig. B.1. For the AggieAir2 UAV platform, the sensors include the GPS, IMU, and the voltmeter while the actuators include the throttle motor and the elevons. The communication devices include one 900 MHz serial modem and one RC receiver. The remote control using the RC transmitter is also called the safety link, or fly-by-wire (FBW). The data link between the UAV and the ground is connected through a pair of modems. The data link includes the telemetry for health monitoring (one-way communication) and the DL setting for real-time tunings (two-way communication). The autopilot software is to achieve the sensing, actuation, and

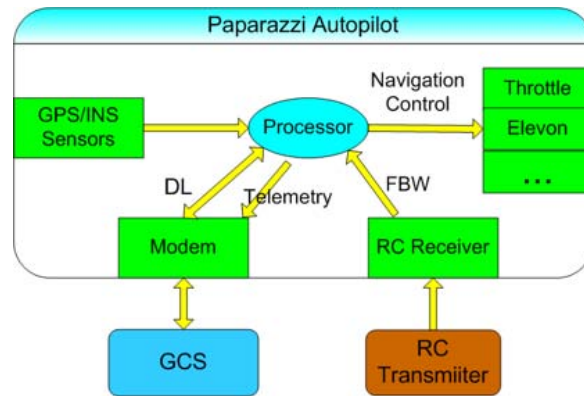


Fig. B.1: Paparazzi autopilot software structure.

communication tasks using all the devices described above. The codes running on the central processor is written in C and the specific parameters for control and navigation purposes are implemented in XML files [23].

B.2 Configuration XML Files

Paparazzi UAV project uses several XML files for the user-specific configuration settings including the flight plan, airframe parameters, and communication setting parameters [23]. Different users could have different navigation plans, various airframes or communication devices. The major configuration files include:

- The airframe configuration file, which contains all the airframe parameters like controller gains, elevon mix setting, max servo limits, and most importantly, the airborne files for uploading;
- The flight plan, which is to set the default flight plan and exceptional behaviors using blocks;
- The data link setting, which is to specify the DLsetting message types (DLsetting is used for online tuning);

- The telemetry configuration file, which is to set the telemetry messages to be sent to the GCS in real-time;
- The radio configuration file, which contains the RC transmitter setting.

All the configuration files are stored in the */paparazzi3/conf* directory or sub-directories under it by default.

B.3 Airborne C Files

The key parts of the Paparazzi autopilot code are implemented in C. The airborne files are located in the */paparazzi3/sw/airborne* directory. Because Paparazzi UAV is an open source project, many macros and conditional inclusions (*#ifdef*, *#endif*) are used for different users. A brief description of the airborne files are introduced in the following:

- *main.c*: the main function of the whole autopilot code;
- *main_ap.c*: the sub-functions implemented with either time interrupts or event interrupts;
- *main_fbw.c*: the fly by wire implementation for the RC control;
- *ap_downlink.h*: the communication sub-function definitions;
- *gps.c* and *gps_ubx.c*: the GPS protocol;
- *osam_ugear.c* and *osam_ugear.h*: the OSAM-Paparazzi interface for getting GPS/INS data from the Gumstix;
- *infrared.c*: to read the Infrared sensor outputs through ADC;
- *fw_h_ctl.c* and *fw_v_ctl.c*: for the low level control.

Paparazzi software uses a “task event” structure [23]. For example, the “main.c” is implemented as follows.

```

Paparazzi airborne code: main function.
while(1){
    if (sys_time_periodic()) {
        Fbw(periodic_task);
        Ap(periodic_task);
        Fbw(event_task);
        Ap(event_task);
    }
    ...
}

```

The Paparazzi UAV project provides several demo examples in the airborne directory for a better understanding of the airborne code writing using LPC processors. The demo file examples include [23]:

- *main_demo1.c*: to show how the code works with no specific functions;
- *main_demo2.c*: to show how to make the LED toggle;
- *main_demo3.c*: to make the LED toggle and send data to UART0;
- *main_demo4.c*: to downlink formatted messages to the modem UART;
- *main_demo5.c*: to show how to modify the setting files through a user defined GUI;
- *main_demo6.c*: for the USB-serial communication.

All the XML files are first converted to C header files. Then the airborne files are linked and compiled into an elf file. The elf file is finally uploaded to the autopilot.

B.4 OSAM-Paparazzi Interface Implementation

The functions of the OSAM-Paparazzi Interface are explained in detail in Chapter 2. This manual focuses on the implementation part. Several C files are modified or added to the airborne directory.

- *main_ap.c*: modified to add the new event of receiving packets from Gumstix;
- *ap_downlink.h*: modified to add new telemetry messages for debugging purposes;

- *infrared.c*: modified to stop the angle updates from infrared sensors;
- *osam_imu_ugear.c* and *osam_imu_ugear.h*: created for the OSAM-Paparazzi communication protocol;

The event of receiving messages from the Gumstix is added to replace the default event to receive the GPS messages.

```

Event modifications in main_ap.c


---


#ifdef OSAMUGEAR
    if (UgearBuffer()) {
        ReadUgearBuffer();
    }
    if (ugear_msg_received){
        parse_ugear_msg();
        ugear_msg_received = false;
        if (gps_pos_available){
            UseGpsPosUgear(estimator_update_state_gps);
            gps_pos_available = FALSE;
            ...
        }
    }
}
#endif /* OSAMUGEAR*/

```

The airframe configuration XML file needs also to be modified since the OSAM-Paparazzi interface is used to replace the default GPS for the UART1. The following lines need to be added.

```

ap.CFLAGS += -DOSAMUGEAR -DUGEAR_LED=2 -DUSE_UART1
-DOSAMUGEAR_LINK=Uart1 -DUART1_BAUD=B115200

ap.srccs += osam_ugear.c latlong.c

```

B.5 Roll-Channel Fractional Order Controller Implementation

The roll-channel flight controller design part is introduced in Chapter 4. The implementation details are covered in this manual. Related files in the airborne directory are modified or added.

- *main_ap.c*: modified to replace the default flight controller with ours, called AggieController;
- *ap_downlink.h*: modified to add the debug telemetry since the low level flight control requires the real-time data for further analysis;
- *osam_aggie_controller.c* and *osam_aggie_controller.h*: added to implement the low-level Aggie controllers.

The pseudo codes added in the *main_ap.c* are shown in the following.

Modifications in *main_ap.c*

```

#ifndef AGGIECONTROLLER
    h_ctl_attitude_loop();
    v_ctl_throttle_slew();
#else
    if (pprz_mode != PPRZ_MODE_AUTO1) {
        aggie_h_ctl_setpoint();
        aggie_h_ctl_roll_loop();
        aggie_h_ctl_pitch_loop();
        aggie_ctl_throttle_loop();
        ...
    }
#endif /* AGGIECONTROLLER*/

```

The main parts for the implementation of the proposed FOPI controller is achieved in the *osam_aggie_controller.c* file, shown in the following.

```

/* $Id: osam_aggie_controller.c 2710 2008-09-12 22:11:35Z osam $
 * Copyright (C) 2009-2019 Haiyang Chao
 * This file is part of paparazzi.
 *
 * paparazzi is free software; you can redistribute it and/or modify
 * it under the terms of the GNU General Public License as published by
 * the Free Software Foundation; either version 2, or (at your option)
 * any later version.

```

```

*
* paparazzi is distributed in the hope that it will be useful,
* but WITHOUT ANY WARRANTY; without even the implied warranty of
* MERCHANTABILITY or FITNESS FOR A PARTICULAR PURPOSE. See the
* GNU General Public License for more details.
*
* You should have received a copy of the GNU General Public License
* along with paparazzi; see the file COPYING. If not, write to
* the Free Software Foundation, 59 Temple Place - Suite 330,
* Boston, MA 02111-1307, USA.
*/
/** \file osam_aggie_controller.c
 *  \brief header file for Aggie flight controller
 *  This file is first generated by Haiyang Chao on 20090929.
 */
/*aggie_outer_roll_loop function is to do a pid control of roll loop
from a outter loop*/
void aggie_outer_roll_loop_pid(void){
    float h_ctl_roll_outer_pgain = ir_correction_left;
    float h_ctl_roll_outer_igain = ir_correction_right;
    static float i = 0.0; /*Ki controller output*/

    BoundAbs(aggie_roll_outer_setpoint, h_ctl_roll_max_setpoint);
    float p = h_ctl_roll_outer_pgain*(estimator_phi - aggie_roll_outer_setpoint);
    float v = p + i;
    aggie_roll_setpoint = SAT2(v,PI/4*ir_correction_down);

    i = i+h_ctl_roll_outer_pgain*h_ctl_roll_outer_igain/FREQ*

```

```

(estimator_phi-aggie_roll_outer_setpoint)+
2*h_ctl_roll_outer_igain/FREQ*(aggie_roll_setpoint-v);

/*The following is just for debugging use
aggie_float1 = 111.1;
aggie_float2 = i;
aggie_float3 = v;
aggie_float4 = aggie_roll_setpoint;*/
}

/*aggie_outer_roll_loop_foc function is to do a pid control of roll
loop from a outter loop*/
void aggie_outer_roll_loop_foc(void){
    float h_ctl_roll_outer_pgain = ir_correction_left;
    float h_ctl_roll_outer_igain = ir_correction_right;
    static float err_windup = 0.0;
    static float i = 0.0; /*variable for integrator output*/

    BoundAbs(aggie_roll_outer_setpoint, h_ctl_roll_max_setpoint);
    float p = h_ctl_roll_outer_pgain*(estimator_phi - aggie_roll_outer_setpoint);
    u_foc2 = u_foc1; /*update u(t-2)*/
    u_foc1 = u_foc0; /*update u(t-1)*/
    u_foc0 = p*h_ctl_roll_outer_igain+2*h_ctl_roll_outer_igain*err_windup;
    y_foc2 = y_foc1; /*update y(t-2)*/
    y_foc1 = y_foc0; /*update y(t-1)*/

    float foc = u_foc0*NUM2+u_foc1*NUM1+u_foc2*NUM0-y_foc1*DEN1-y_foc2*DEN0;
    y_foc0 = foc;

```

```

    i = i + y_foc1/FREQ;

    float v = p + i;

    aggie_roll_setpoint = SAT2(v,PI/4*ir_correction_down);

    err_windup = aggie_roll_setpoint - v;


/* for debug use only*/

    aggie_float1 = foc; //for debug 20091009
    aggie_float2 = i; //for debug 20091009
    aggie_float3 = u_foc0; //for debug 20091009
    aggie_float4 = v; //for debug 20091009
} /* function aggie_outer_roll_loop_foc stopped here*/


void aggie_h_ctl_roll_loop( void ) {

    float err = estimator_phi - aggie_roll_setpoint;

    float cmd = h_ctl_roll_pgain * err;

    h_ctl_aileron_setpoint = TRIM_PPRZ(cmd);

}


void aggie_h_ctl_pitch_loop( void ) {

    static float last_err;

    float err = estimator_theta - h_ctl_pitch_setpoint;

    float d_err = err - last_err;

    last_err = err;

    float cmd = h_ctl_pitch_pgain * (err + h_ctl_pitch_dgain * d_err);

    h_ctl_elevator_setpoint = TRIM_PPRZ(cmd);

}


void aggie_ctl_throttle_loop( void ) {

```

```
float cmd = 6720.0; /*70% 20091002*/  
v_ctl_throttle_slewed = TRIM_UPPRZ(cmd);  
}
```

Appendix C

List of Documents for CSOIS Flight Test Protocol

A series of flight test documents are included in this appendix to show how to perform routine flight tests in a systematic way. One of the contributions of this dissertation is to establish the flight test protocol to minimize the happening of accidents. The flight test documents are summarized based on the extensive flight test experiences from CSOIS OSAM-UAV team.

C.1 Sample CSOIS-OSAM Flight Test Request Form

1. Flight Test Time: 10/05/2009 8:00 - 12:00 AM
2. Field Test Crew: Haiyang Chao, Ying Luo, Hu Sheng
3. Flight Test Missions (in priorities): Fly ChangE with Aggie-controller 0.2
 - Square: roll_desire = -10-+10, pitch_desire = 0, throttle_desire = 0.7. Square.time = 5*2 s.
 - Square: roll_desire = -20-+20, pitch_desire = 0, throttle_desire = 0.7. Square.time = 5*2 s.
 - PRBS: pitch_desire = 0, throttle_desire = 0.7. Roll.design_Length=15.
 - Outer_loop test with P controller.
 - Outer_loop test with PI controller.
4. Field Operators Required:
 - Flight Test Preparation and Checklist: Haiyang Chao, Ying Luo, Hu Sheng
 - Car Rental: UWRL truck driven by A.M. Jensen

- Safety Pilot: Haiyang Chao
- GCS Operator: Hu Sheng (Ying Luo to learn)
- Camera Record: Ying Luo

5. Airplanes needed: ChangE 60”

6. Lab Preparation Needed:

- Special test for this mission: Check Aggie-controller 0_2 on the ground
- In-lab airframes inspection
- What-to-bring checklist

C.2 Sample CSOIS-OSAM 48" UAV (IR) In-lab Inspection Form

UAV Inspector			
UAV	Name	Pheonix 48"	Dimon 48"
ID	Take-off Weight (kg)		
	RC Channel		
System	Surface Smooth		
Check	Winglet Stable		
Balance	Hang-up		
Check	Manual		
Actuators	Default Trim(1/30 in.)		
Check	Elevon Moving Range		
	Propeller No Damage		
	Throttle Moves Correctly		
	Elevon Moves Correctly		
	Nothing Loose		
Sensors	IR Sensor Check		
Check	GPS Quick Lock		
	Correct Orientation(PFD)		
	Auto1 check		
Communication	RC Range (step)		
Check	Modem Commit		

C.3 Tiger Preflight Checklist for AUVSI SUAS Competition 2009

- (1) Motor mount screws tight.
- (2) Prop bolt tight.
- (3) Nothing loose.
- (4) Elevons move correctly.
- (5) Throttle turns on.
- (6) Correct IMU data (orientation).
- (7) GPS lock valid.
- (8) Wifi link OK.
- (9) Camera lens cover clear.
- (10) Camera setup OK (fire up altitude and camera setting).
- (11) Camera status (1 means initialized).
- (12) Gumstix SD card clear.
- (13) Walk 25 big steps into the wind after the bungee is fully extended.
- (14) Turn on the motor switch right before the launch. Raise the UAV as high as you can and let it go.

Appendix D

DiffMAS2D Code Modification Guide

DiffMas2D [114] is a diffusion control simulation platform written in MATLAB/Simulink. The basic idea of DiffMas2D is to use a sensor and actuator network for the sensing and actuation of a diffusion process modeled by the following equation:

$$\frac{\partial \rho}{\partial t} = k \left(\frac{\partial^2 \rho}{\partial x^2} + \frac{\partial^2 \rho}{\partial y^2} \right) + f_d(x, y, t) + f_c(\tilde{\rho}, x, y, t), \quad (\text{D.1})$$

where k is a positive constant representing the diffusing rate, $f_d(x, y, t)$ shows the pollution source, $\tilde{\rho}$ is the sensor measurements, $f_c(\tilde{\rho}, x, y, t)$ is the control input applied to neutralize pollutants.

The major functions of the DiffMas2D software include:

- solving the PDE model (D.1);
- providing sensor readings for any position within the domain;
- applying the feedback control law on how much to spray ($f_c(\tilde{\rho}, x, y, t)$);
- planning the path for the actuators.

D.1 Files Description

DiffMas2D is comprised of one Simulink model and a series of preprocessing and post-processing M files. The main files are briefly introduced in the following:

- *simstart.m*: the file to start the simulation;
- *initialization.m*: the file to set up the initial parameters like the diffusion speed, sensor and actuator numbers, and initial positions;

- *init_check.m*: the file to test if there is any conflictions between the settings and the Simulink model;
- *pre_process.m*: the file for the boundary settings;
- *diffu_ctrl_sim.mdl*: the main model file to the real-time simulation;
- *post_process.m*: the file to depict all the saved data in pictures.

diffu_ctrl_sim.mdl is the central file of the DiffMas2D simulation platform, shown in Fig. D.1 and the key subfunctions are defined with M files like the actuator path planning and the spraying control. Several important M functions are introduced in the following:

- *controller.m*: the function for neutralizing control;
- *actrl.m*: the function for the actuator position control;
- *ades.m*: the function to calculate the desired position of each actuator for monitoring purposes;
- *distout.m*: the function to define the diffusion source.

D.2 Diffusion Animation Generation

DiffMAS2D supports the generation of the diffusion animation after running the simulation for a preset time period. All the simulated data is saved in the workspace and *post_process.m* can convert the data into jpg pictures. The user can then use some softwares to convert multiple jpg pictures into an animation gif file.

D.3 Implementation of CVT-Consensus Algorithm

The CVT-Consensus algorithm is mostly implemented in *actrl.m* and *ades.m*. The *actrl.m* file is shown in the following.

```
function out = actrl(in)
% actrl: actuator position control. Output the acceleration of each actuator.
```

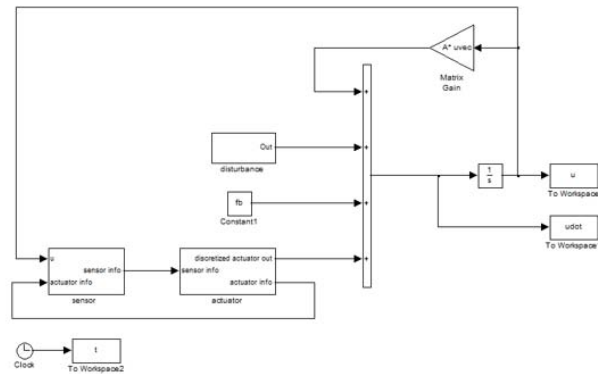


Fig. D.1: DiffMAS2D Simulink model.

```
% The actuator is modeled as two double integrators:
%
%       $\ddot{x} = f_x(t)$ ,
%       $\ddot{y} = f_y(t)$ .
%   $f_x(t)$  and  $f_y(t)$  are defined in this file.

% keyboard
in = in(:);

NS = in(1); % number of sensors
NA = in(2); % number of actuators
apos = reshape(in(3:2*NA+2), NA, 2);

% actuator velocity matrix. [avel(i,1),avel(i,2)] is the current velocity
% of the ith actuator
avel = reshape(in(2*NA+3:4*NA+2), NA, 2);
```

```

% current sensor infomation.

% [sinfo(i,1),sinfo(i,2)] is the current position of the ith sensor
% [sinfo(i,3),sinfo(i,4)] is the current velocity of the ith sensor
% sinfo(i,5) is the sensed data of the ith sensor
sinfo = reshape(in(4*NA+3:4*NA+5*NS+2), NS, 5);

% current time
t = in(end);

%%%%%%%%%%%%%%%%%%%%%%%%%%%%%%%%%%%%%%%%%%%%%%%%%%%%%%%%%%%%%%%%%%%%%%%%
% Code below this line should be written by the user to achieve the desired %
% actuator movement. The final output is a vector in the format of %
% [fx_1,fx_2,...,fx_NA,fy_1,fy_2,...,fy_NA]' %
%%%%%%%%%%%%%%%%%%%%%%%%%%%%%%%%%%%%%%%%%%%%%%%%%%%%%%%%%%%%%%%%%%%%%%%%

global p_out sum_s controlTime;
controlTime=controlTime+1;
if controlTime==100 %300
    controlTime=0;

    %arrays to record the points that is most close to i's actuator
    p=zeros(NA, 300);

    %array to indicate the number of points for each actuator
    p_index=zeros(NA,1);

    %find the Vi for each actuator
    p_out=zeros(NA,2);
    sum_s=zeros(NA,1);

    %design acceleration for each actuator
    k1=3; k2=1;

```

```

% Voronoi Diagram computing (Nearest actuator strategy)
for i=1:NS
    min=( ( apos(1,1)-sinfo(i,1) )^2+( apos(1,2)-sinfo(i,2) )^2 );
    mini=1;
    for j=2:NA
        temp=( ( apos(j,1)-sinfo(i,1) )^2+( apos(j,2)-sinfo(i,2) )^2 );
        if temp < min
            min=temp;
            mini=j;
        end
    end
    if(min < 0.04) % added this condition 20060923 for increasing PrayK
        p_index(mini)=p_index(mini)+1;
        p( mini,p_index(mini) )=i;
    end
end
des=zeros(NA,2);

for i=1:NA
    sumx=0;
    sumy=0;
    sumd=0;
    for j=1:p_index(i)
        % added 20060903 to delete positions that sensor reading too small
        sumx=sumx+sinfo(p(i,j),5)*sinfo( p(i,j),1);
        sumy=sumy+sinfo(p(i,j),5)*sinfo( p(i,j),2);
        sumd=sumd+sinfo(p(i,j),5);
    end
end

```

```

        if(sumd == 0)
            des(i,1)=apos(i,1);
            des(i,2)=apos(i,2);
            sum_s(i)=0;
        else
            des(i,1)=sumx/sumd;
            des(i,2)=sumy/sumd;
            sum_s(i)=sumd/p_index(i);
        end
    end
end
if(t<2)
    Lmatrix3 = [-2 0 -1 0;0 -2 -1 0;0 0 -3 0;0 0 -1 -2];
    p_out = Lmatrix3*(apos-des);
elseif ((t > 2) && (sum(sum_s/sum_s(3)) < 2))
    Lmatrix1 = [-1 0 1 0;0 -1 1 0;0 0 -1 0;0 0 1 -1];
    Lmatrix2 = [0 0 0 0;0 0 0 0;0 0 -1 0;0 0 0 0 ];
    p_out = Lmatrix1*apos-Lmatrix2*des;
else
    Lmatrix0 = (-1)*k1*eye(NA,NA);
    p_out = Lmatrix0*(apos-des);
end
end

if(t > 0.2)
    fgorki = 1;
end
out = reshape(p_out, 2*NA,1);

```


Vita

Education

- Ph.D. (May, 2010), Electrical and Computer Engineering Department, Utah State University, Logan, Utah, U.S.A.
- M.S. (June, 2005) Electrical Engineering Department, Zhejiang University, Hangzhou, Zhejiang, China.
- B.S. (June, 2001) Electrical Engineering Department, Zhejiang University, Hangzhou, Zhejiang, China.

Book Chapter

- Chapter 22: AggieAir: Towards Low-cost Cooperative Multispectral Remote Sensing Using Small Unmanned Aircraft Systems, Haiyang Chao, Austin Jensen, Yiding Han, YangQuan Chen, and Mac McKee, *Advances in Geoscience and Remote Sensing*, Gary Jedlovec, Ed. Vukovar, Croatia: IN-TECH, pp. 463-490, ISBN 978-953-307-005-6, 2009.

Journal Articles

- Fractional Order [Proportional Integral] Flight Control for the Roll-Channel of a Small Fixed-Wing UAV, Ying Luo, Haiyang Chao, Long Di, and YangQuan Chen, submitted under review.
- Roll-Channel Fractional Order Controller Design for a Small Fixed-Wing Unmanned Aerial Vehicle, Haiyang Chao, Ying Luo, Long Di, and YangQuan Chen, *Control Engineering Practice (CEP)*, accepted to appear, doi:10.1016/j.conengprac.2010.02.003, 2010.
- Cooperative Sensing and Distributed Control of a Diffusion Process using Centroidal Voronoi Tessellations, Haiyang Chao, and YangQuan Chen, *Numerical Mathematics: Theory, Methods and Applications (NMTMA)*, accepted to appear, 2010.

- Autopilots for Small Unmanned Aerial Vehicles: A Survey, Haiyang Chao, Yongcan Cao, and YangQuan Chen, *International Journal of Control, Automation, and Systems (IJCAS)*, vol.8, no.1:36-44, 2010.
- Experimental Validation of Consensus Algorithms for Multi-vehicle Cooperative Control, Wei Ren, Haiyang Chao, William Bourgeois, Nathan Sorensen, and YangQuan Chen, *IEEE Transactions on Control Systems Technology (TCST)*, vol.16, 4:745-752, 2008.
- A Study of Grouping Effect On Mobile Actuator Sensor Networks for Distributed Feedback Control of Diffusion Process Using Central Voronoi Tessellations, Haiyang Chao, YangQuan Chen, and Wei Ren, *International Journal of Intelligent Control Systems (IJICS)*, vol. 11, no. 3, pp. 185-190, 2006.

Conference Papers

- A Two-stage Calibration Method for Low-cost UAV Attitude Estimation Using Infrared Sensor, Long Di, Haiyang Chao, and YangQuan Chen, *IEEE/ASME International Conference on Mechatronic and Embedded Systems and Applications (MESA)*, submitted under review 2010.
- Low-Cost-UAV Based Thermal Infrared Remote Sensing: Platform, Calibration and Applications, Hu Sheng, Haiyang Chao, Cal Coopmans, Jinlu Han, Mac McKee, and YangQuan Chen, *IEEE/ASME International Conference on Mechatronic and Embedded Systems and Applications (MESA)*, submitted under review 2010.
- Fractional Order [Proportional Integral] Roll Channel Flight Control for Small Fixed-Wing UAV, Ying Luo, Haiyang Chao, Long Di and YangQuan Chen, *the 8th World Congress on Intelligent Control and Automation (WCICA)*, accepted to appear 2010.
- Real-Time Cooperative Wind Profile Mapping Using Multiple Low-Cost Unmanned Aerial Vehicles, Haiyang Chao, Johnathan Nielsen, Long Di, Ying Luo and YangQuan Chen, *AUVSI's Unmanned Systems North America*, accepted to appear 2010.
- Surface Wind Profile Measurement Using Multiple UAVs, Haiyang Chao and YangQuan Chen, *American Control Conference*, accepted to appear 2010.
- Fractional Order Flight Control of a Small Fixed-Wing UAV, Haiyang Chao, Ying Luo, Long Di, and YangQuan Chen, *ASME International Design Eng. Technical Conference Computers and Information in Eng. Conference (IDETC/CIE)*, No. MESA-87574, Sep. 2009.

- Design and Implementation of Sensing and Estimation Software in Aggienav, a Small UAV Navigation Platform, Calvin Coopmans, Haiyang Chao, and YangQuan Chen, *ASME International Design Engineering Technical Conferences Computers and Information in Engineering Conference (IDETC/CIE)*, No. MESA-87675, Sep. 2009.
- Team OSAM-UAVs Design for the 2008 AUVSI Student UAS Competition, Christopher J. Hall, Daniel Morgan, Austin Jensen, Haiyang Chao, Calvin Coopmans, Mitchel Humpherys, and YangQuan Chen, *ASME International Design Eng. Technical Conference Computers and Information in Engineering Conference (IDETC/CIE)*, No. MESA-87675, Sep. 2009.
- Multiple Micro Aerial Vehicles for Applications in Real-Time Remote Sensing, Christopher Hall, Daniel Morgan, Austin M. Jensen, Haiyang Chao, YangQuan Chen and Mac McKee, *AWRA Annual Water Resources Conference*, Nov. 2008.
- Band-reconfigurable Multi-UAV-based Cooperative Remote Sensing for Real-time Water Management and Distributed Irrigation Control, Haiyang Chao, Marc Baumann, Austin Jensen, YangQuan Chen, Yongcan Cao, Wei Ren and Mac McKee, *International Federation of Automatic Control World Congress*, July, 2008.
- Consensus of Information in Distributed Control of a Diffusion Process using Centroidal Voronoi Tessellations, Haiyang Chao, YangQuan Chen, and Wei Ren, *IEEE International Conference on Decision and Control (CDC)*, Dec. 2007.
- Experimental Implementation and Validation of Consensus Algorithms on a Mobile Actuator and Sensor Network Platform, Wei Ren, Haiyang Chao, William Bourgeois, Nathan Sorensen, and YangQuan Chen, *IEEE Conference on Man, System, and Cybernetics*, Oct., 2007.
- Autopilots for Small Fixed-Wing Unmanned Air Vehicles: A Survey, Haiyang Chao, Yongcan Cao, and YangQuan Chen, *IEEE International Conference on Mechatronics and Automation (ICMA)*, Aug. 2007.
- Mobile Actuator Networks for Distributed Feedback Control of Diffusion Process Using Multiscale Central Voronoi Tessellations, Haiyang Chao, YangQuan Chen, and Wei Ren, *SIAM Conference on Computational Science and Engineering*, Feb. 2007.
- A Study of Grouping Effect On Mobile Actuator Sensor Networks for Distributed Feedback Control of Diffusion Process Using Central Voronoi Tessellations, Haiyang Chao, YangQuan

Chen, and Wei Ren, *IEEE International Conference on Mechatronics and Automation (ICMA)*, June 2006.

Honors and Awards

- Outstanding Graduate Research Assistant, Electrical and Computer Engineering Department, Utah State University, Mar. 2010.
- Association for Unmanned Vehicle Systems International (AUVSI), graduate supervisor, navigation engineer, and safety pilot of Team USU OSAM, the 1st Place Team with \$14000 prize in 2009 AUVSI student UAS competition (totally 18 teams), Jun. 2009.
- Association for Unmanned Vehicle Systems International (AUVSI), airframe designer and navigation engineer of Team USU OSAM, the 2nd Place Team with \$8000 prize in 2008 AUVSI student UAS competition (totally 16 teams), Jun. 2008.
- Utah State University, Graduate Student Senate Enhancement Award, (20 recipients out of more than 100 applicants), 2008.
- NSF-IPAM(Institute for Pure and Applied Mathematics)-UCLA, travel grant for one week-long workshop on “Mathematical Challenges on Sensor Networks”, Jan. 2007.
- IEEE International Conference on Mechatronics and Automation, Best Student Paper Finalist, Jun. 2006.
- Utah State University, Vice President’s Fellowship, 2005-2006.

Teaching and Mentoring

Graduate Advisor

January, 2008 - present

Graduate advisor for 2009 AUVSI Student UAS Competition Team OSAM-UAV. Planning and coordinating 14 UAV flight tests (about half a day each).

NSF REU Student Supervisor

Summer, 2006 and 2007

Serving as the student supervisor for National Science Foundation Research Experiences for Undergraduate Program (MAS-net). Lectures for undergraduates on researches undergoing in CSOIS. Supervising students in their research projects and organizing outdoor activities.

Guest Lecturer

August, 2005 - present

Presenting seasonal lectures for undergraduate level course ECE 5320 Mechatronics in Spring 2008 and BIE 3000 Instrumentations for Biological Systems in Spring 2006 and 2007.

Guest Lab TA

March, 2010

Mentoring in the lab “Nonparametric System Identification with PRBS Excitations” for undergraduate level course ECE 5320 Mechatronics in Spring 2010.

Professional Presentations

- Mar. 9, 2010: Presentation titled “AggieAir: Towards Low-cost Cooperative Multispectral Remote Sensing Using Small Unmanned Aircraft Systems” for ECE 6800 Graduate Colloquium of Utah State University, Logan, UT, USA.
- Aug. 31, 2009: Presentation titled “Fractional Order Flight Control of a Small Fixed-Wing UAV” in International Conference on Mechatronic and Embedded Systems and Applications (MESA), San Diego, CA, USA.
- Jan. 22, 2009: Presentation titled “Progress of fractional order flight control of fixed-wing UAVs, simulation results and flight test results” for CSOIS Applied Fractional Control (AFC) Reading Group, Utah State University, Logan, UT, USA.
- Dec. 12, 2007: Presentation titled “Consensus of Information in Distributed Control of a Diffusion Process using Centroidal Voronoi Tessellations” in IEEE International Conference on Decision and Control (CDC), New Orleans, LA, USA.
- Feb. 20, 2007: Presentation titled “Mobile Actuator Networks for Distributed Feedback Control of Diffusion Process Using Multiscale Central Voronoi Tessellations” in SIAM Conference on Computational Science and Engineering, Costa Mesa, CA, USA.
- June 27, 2006: Presentation titled “A Study of Grouping Effect On Mobile Actuator Sensor Networks for Distributed Feedback Control of Diffusion Process Using Central Voronoi Tessellations” in International Conference on Mechatronics and Automation (ICMA), Luoyang, Henan, China.